Landslide early warning systems from weather radar observations

A case study in the Khao Yai National Park, Thailand

Master Thesis

Jonathan Linnebach

Delft University of Technology

TU Delft

Landslide early warning systems from weather radar observations

A case study in the Khao Yai National Park, Thailand

by

Jonathan Linnebach

to obtain the degree of Master of Science in Environmental Engineering
at the Delft University of Technology

To be defended publicly on Friday September 13, 2024.

Student number:	5843162	
Project duration:	February, 2024 – September, 2024	
Thesis committee:	Prof. dr. T. Bogaard,	TU Delft
	Dr. ir. G. Schoups,	TU Delft
	Dr. P. P. Mapiam,	Kasetsart University

TU Delft

Acknowledgements

This thesis project would not have been possible without the great people around me. Their efforts and support allowed me to successfully complete this project while also making it a fun and enjoyable period full of new experiences and things to learn.

First and foremost, I would like to thank my mentor, Prof. Dr. Thom Bogaard, for his guidance and support throughout this research. His expertise and engagement in many discussions not only shaped this project but also gave me the opportunity to deepen my personal knowledge in the field. The weekly landslide colloquium with other students from this field gave me an interesting insight into many more aspects of the field far beyond my own thesis project.

I would also like to extend my gratitude to Professor Punpim and Poom, who welcomed me at Kasetsart University and made sure that I had an unforgettable time in Bangkok. It was a great experience working together on this project and I'm proud of what we have achieved together. Without their support, this research would not have been possible.

Additionally, I'm very thankful to Dr. Gerrit Schoups, whose advice and expertise have contributed to my academic development and the achieved quality of this work.

Furthermore, I want to thank Professor Apiniti and his students for providing me with the laboratory and field equipment during my time at Kasetsart University. I especially want to thank Golf for his extensive support during the experiments in the laboratory.

To my family and friends from the Dispuut Water and Environment, B17, and also all the others who came to visit Delft during this period, thank you very much for your support. You especially made this a very enjoyable time.

Finally, I acknowledge the financial support provided by Delft Global Initiative and FAST Fund, which made this research, and especially the field visit to Thailand, possible. Their funding and resources were crucial to the successful completion of this project.

Jonathan Linnebach
Delft, September 2024

Abstract

Landslides are one of the most widespread natural hazards, causing thousands of casualties every year and significant economic damage worldwide. In mountainous regions of Thailand, damages and fatalities due to landslides have increased over the last decades due to intensified human interventions. This research aims to contribute to the development of a near real-time, joint early warning system for flash floods and landslides in Khao Yai National Park, Thailand.

Spatial and temporal landslide occurrences in Khao Yai National Park were assessed. To extend the available landslide inventory, the detection of historical landslides was automated on the Google Earth Engine platform using remotely sensed relative changes in NDVI. Predisposing factors of landslide occurrence were determined using the frequency ratio method. A susceptibility map was then derived by linking the detected landslides to the predisposing factors: slope angle, aspect, land use, lithology, and distance to road. Validation with the landslide inventory shows excellent classification performance.

The temporal probability was assessed using a physically-based multi-hazard model. The hydrological model includes the driving hydrological processes for each grid cell. The streamflow model output was calibrated using observed nested river discharge events. The model performance was tested under spatially distributed precipitation forcing of varying quality. The results show good performance in predicting streamflow and landslide occurrence based on modeled antecedent conditions when using high-quality weather radar information as forcing.

This research demonstrates the effectiveness of integrating fully distributed physically-based modeling with high-resolution spatial rainfall observations from weather radar. The findings are expected to enhance the development of a multi-hazard early warning system and improve disaster risk management in northeastern Thailand.

Contents

List of Figures

List of Tables

1 Introduction

Landslides are one of the most widespread natural hazards causing thousands of casualties every year and economic damage worldwide (Froude and Petley, 2018). While landslides can be caused by earthquakes, volcanic eruptions, or human activity, most landslides are triggered by rainfall events. This results in pore pressure buildup in the soil and destabilization of slopes due to local hydrological processes. The current development of climate change leading to more extreme rainfall events in the future has therefore the effect of further increasing the areas prone to landslides (Bogaard and Greco, 2016).

1.1. Background

A landslide is defined as the downward sliding of a mass of debris, earth, or rocks on a slope under the influence of gravity. The destabilization of slopes is a complex combination of geomechanical, geomorphological, hydrological, and hydraulic processes. Determining the cause of a landslide is therefore a multidisciplinary problem. Trigger events play a key role in the destabilization of a slope. These can be, earthquakes, volcanic eruptions but most importantly heavy precipitation events. However, these events are only the final 'push' that causes a slope to fail. The antecedent hydrological conditions of the slope at the beginning of the trigger event are therefore at least as important. Depending on the 'pre-wetting' of the slope a heavy rainfall event may become a trigger event or not. The study of landslide hydrology therefore contains understanding hydrological processes like filling, storing, and draining of water in a slope to determine the antecedent conditions as well as understanding the processes during a trigger event. While all of the single processes are well understood by different research fields, the study combined processes and possible feedback has only gained attention in recent years (Bogaard and Greco, 2016).

To reduce the risk of loss and damage due to natural hazards such as landslides, the 2015 Third UN World Conference on Disaster Risk Reduction (WCDRR) has adopted the Sendai Framework of Disaster Risk Reduction. This framework outlines seven global targets to be achieved by 2030 to reduce disaster risks and provides member states with concrete actions to achieve these goals. The targets include targets to reduce global mortality, affected people, and economic loss due to natural disasters as well as increasing measures and strategies to reduce disaster risk. One of the targets raises a specific goal: *Substantially increase the availability of and access to multi-hazard early warning systems and disaster risk information and assessments to people by 2030* (UNISDR, 2015).

As a result of this, the development of Landslide Early Warning Systems (LEWS) has seen increased attention in recent years using a wide variety of approaches. While the development of a global LEWS based on global landslide susceptibility maps and satellite rainfall observations is an ambitious goal that gives authorities important information to prepare for disasters on a national level, the obtained resolution is not sufficient to take measures on a local scale (Stanley et al., 2021). Territorial LEWS, usually managed by local authorities based on local rainfall information can produce more specific

warnings which enables authorities to take measures like closing roads or evacuating people. These LEWS however require local data and resources to develop and maintain the system and are therefore not accessible in many parts of the world (Piciullo et al., 2018).

In scientific literature, results of landslide studies are usually displayed in one of three types of maps: Maps of spatial incidence such as landslide inventories or susceptibility maps, maps of spatial-temporal incidence, and forecasting of landslides such as landslides hazard maps due to a specific trigger event and maps of landslide risk assessment (Chacón et al., 2006). Operational LEWS are mostly classified as spatial-temporal models and can be roughly divided into empirical (statistical) models and physically-based models. Empirical models, based on a threshold of duration and intensity of rainfall, are the most common choice when developing a LEWS. However, these models require an inventory of historical landslide events. Physically-based models on the other hand can be set up without a large amount of landslide observations when necessary. These models require more detailed information about hydrological, geological, and geotechnical parameters as well as more computational power. Physically-based models are therefore mostly limited to local applications (Bogaard and Greco, 2018 and Greco et al., 2023).

In any case, historical landslide inventories are key in developing a LEWS because they are required for model calibration and therefore often impose the largest limitation on the analysis. Different approaches have been applied successfully in the past to improve the landslide inventory for a region. These include studying historical records such as news articles and old maps, conducting field observations, developing citizen science campaigns (Perera et al., 2022) as well as remote sensing applications to detect landslides from space. In recent years multiple workflows have been developed using either pixel or object-based picture analysis to detect landslides. Most of these tools are based on open-source data and therefore usable either through Google Earth Engine scripts or Python packages. (Fayne et al., 2019, Amatya et al., 2021, Ngandam Mfondoum et al., 2021 and Perera et al., 2022).

1.2. Problem statement

In mountainous regions in Thailand damages and fatalities due to landslides have increased as well in the last decades due to more human interventions like building roads or expanding villages in landslide-prone areas. Previous studies have investigated possible actions and concluded that the development of LEWS is the most promising and cost-effective measure to mitigate landslide impacts (Fowze et al., 2012). A simple community-based LEWS using manual rain gauges and rainfall thresholds has already been developed 20 years ago which has helped decrease fatalities enormously by raising awareness for natural hazards (Schmidt-Thomé et al., 2018). However, this system depends on manual measurements and national rainfall thresholds and can therefore only give limited information about possible local hazards.

This thesis project is placed into the framework of this problem. The case study area of the project is the Khao Yai National Park in Thailand. This national park lies in a mountainous area 100 km north-east of Bangkok and is Thailand's most visited national park. In recent years the area has experienced extreme rainfalls repeatedly resulting in flash floods and landslides affecting the roads in the park as well as the villages around the park. The local authorities are therefore aiming for a more advanced early warning system to be prepared for such events in the future. The TU Delft has had a long-lasting collaboration with Kasetsart University's Department of Water Resources Engineering for over 10 years. One of the goals of this collaboration is to develop a multi-hazard early warning system for various regions of Thailand.

A typical LEWS aims to predict spatial and temporal landslide occurrence (Aristizábal et al., 2016). The spatial and temporal components can thereby be predicted simultaneously or in separate stages (Chacón et al., 2006). For the defined study area, the Khao Yai National Park in Thailand, a susceptibility analysis was conducted in 2022 using the Analytical Hierarchy Process in which experts give weights to predisposing factors based on their expertise (Pimmasarn et al., 2022). However, due to the subjectivity of the expert's opinion and a limited number of recorded landslide observations in the

area, these results can not be replicated by other users in different areas (Kirschbaum et al., 2016). By using a statistical model in combination with an advanced landslide inventory the prediction of spatial landslide occurrence can therefore be further improved. In the development of a multi-hazard early warning system, physically-based models offer the potential to predict temporal landslide occurrence and flash flood peaks simultaneously (Aristizábal et al., 2016 and Bout et al., 2022). However, in the tropical and mountainous environment of the study area the data availability, especially of the precipitation forcing, introduces major challenges.

In a previous thesis project, a physically-based model has already been used in the same study area to investigate the effect of using spatially distributed rainfall input instead of uniform input. This study concluded that precipitation forcing with high spatial and temporal resolution has to be used to model the local hydrology accurately. Using rain gauge-based interpolation methods such as inverse distance or Thiessen polygons was not sufficient to represent the local complexity in rainfall patterns with high intensity in the study area (Potthoff, 2022). Another option to obtain precipitation observations with high spatial resolution are remote sensing products such as weather radar observations or satellite-based products. As weather radar information becomes increasingly available around the globe, using this information is a logical step to further improve multi-hazard models. In a previous study, the usage of these spatial observations has already been used successfully in an intensity/duration-based landslide model (Cremonini and Tiranti, 2018). Furthermore, the usage of bias-corrected radar observation for flash flood modeling has widely been tested and can significantly improve the performance of fully spatial distributed models if other required distributed datasets (i.e. topography, vegetation, soils, land use, etc) are available in sufficient quality (Sokol et al., 2021). Thereby, the performance can be highly variable and is dependent on the intensity and duration of a storm event (Rozalis et al., 2010). Taking into account antecedent soil moisture conditions is therefore crucial to explaining different behaviors of a catchment under different storm types (Javelle et al., 2010 and Grillakis et al., 2016).

This thesis project contributes to the development of a multi-hazard early warning system by testing the utilization of spatially distributed rainfall products to model the antecedent conditions and trigger events of landslides in the case area. Through the collaboration project rain radar observations from two stations are available for the Khao Yai National Park. This allows the development of a fully spatially distributed model for landslide hazard prediction in combination with a full hydrological model for the national park area using weather radar as forcing information. The importance of including the antecedent conditions in the multi-hazard model can thereby be assessed.

1.3. Research goal

Physically-based multi-hazard models have received more attention due to increased computational capacities and higher availability of spatially distributed data in the recent decade. However, the usage for operational LEWS is still a challenging task, due to the required detail of spatial information. The availability of weather radar nowcasting information imposes new possibilities when developing a physically-based LEWS. Unfortunately, in mountainous regions the radar products often show low-quality sections in radar reflectivities and beam blockage which imposes major challenges in capturing local high-intensity events. It therefore needs to be tested if the available observations are sufficient to predict a landslide trigger event when used as input for an operational physically-based LEWS. Similar questions arise for the determination of the antecedent conditions. Previous studies suggest that spatially distributed rainfall inputs are necessary. However, the required spatial and temporal resolution in precipitation input remains unknown as well as the influence of occasionally low-quality radar observations.

The research goal of this thesis project is shaped taking into account the goal of the overarching research collaboration and the identified research gap. The research collaboration thereby lays the foundation while the identified research gap defines the details of the goal. The goal of this thesis project is:

> *Determining potentials and limitations of using weather radar information to model antecedent conditions and nowcast trigger events of landslides with a physically-based multi-hazard model in the Khao Yai National Park in Thailand.*

The physically-based multi-hazard model is based on the LISEM software package, developed by University Twente, which was chosen for the study as this model is now used by all participants of the overarching research collaboration. To achieve the research goal, the following research activities are defined as sub-goals:

Sub-goal 1: Creation of a landslide inventory for the Khao Yai National Park.

Sub-goal 2: Analysis of landslide susceptibility for the Khao Yai National Park to asses landslide predisposing factors and determine spatial landslide occurrence.

Sub-goal 3: Development of a spatially distributed physical-based multi-hazard model for the Khao Yai National Park.

Sub-goal 4: Assessment of antecedent hydrological conditions and hydro-meteorological landslide trigger events using the developed model.

1.4. Research approach

The research project was conducted in four stages to achieve the research goal (Figure 1.1). In the first stage, an extended landslide inventory was created by analyzing historical optical remote sensing data to detect land cover changes associated with landslide events. This process was automated on the Google Earth Engine platform, which allows for the efficient analysis of large datasets using external computational power. Secondly, a landslide susceptibility map was derived from this landslide inventory to determine landslide-prone areas and predisposing factors for the study area. This susceptibility map, indicating spatial landslide occurrence is the first component of a LEWS.

The third stage of the research was a field visit to the study site. The main goal of the field visit was to gain an impression of the study area to be able to better justify assumptions in the modeling phase of the project. Furthermore, landslide locations were mapped to validate the landslide inventory and susceptibility map, and soil samples were taken to close gaps in the available data required for the multi-hazard model. The final stage of the project was the development of a physical-based fully spatially distributed multi-hazard model to predict temporal landslide occurrence. This model was then calibrated to the observed streamflow and landslide antecedent conditions and slope stability were assessed for an event at the end of 2022 using weather radar observations as model forcing. The predicted temporal landslide occurrence forms the second component of a LEWS.

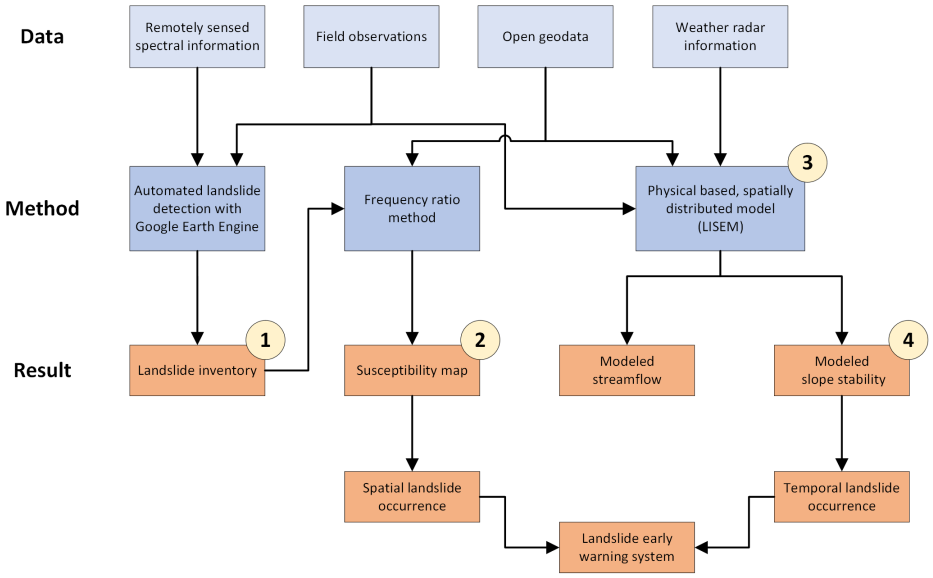

Figure 1.1: Research flow diagram. Numbers 1 to 4 indicate the different research sub-goals respectively.

2

Study area

The Khao Yai National Park is a protected nature area in northeastern Thailand, located about 100 km northeast of Bangkok (Figure 2.1). The national park covers an area of about 2200 km² and can be characterized as a densely forested mountainous area, reaching elevations up to 1300 m above sea level. Due to its proximity to the metropolis, Bangkokians frequently use the park as a weekend holiday destination, which is recognizable in its well-developed tourism infrastructure. The main activities in the area are trekking, wildlife observation, and camping. Due to the large tourism industry in and around the national park, it is not only of ecological but also of socio-economic value (Khao Yai National Park, 2021).

Heavy rainfall events pose a risk of flash floods and landslides to the national park and its surroundings with its developed tourism industry, especially during the rainy season from May to October. As a result of a landslide event in 2020 with about 20 landslides and rockfalls along the main road of the national park, catchment M43A in the northern part of the national park was selected as a case area for the development of a near real-time early warning system for landslides and flash floods (Mapiam et al., 2023).

For this thesis project, two different spatial dimensions were selected for the study area. First, the entire national park was considered as study area to increase the amount of observed landslides to a

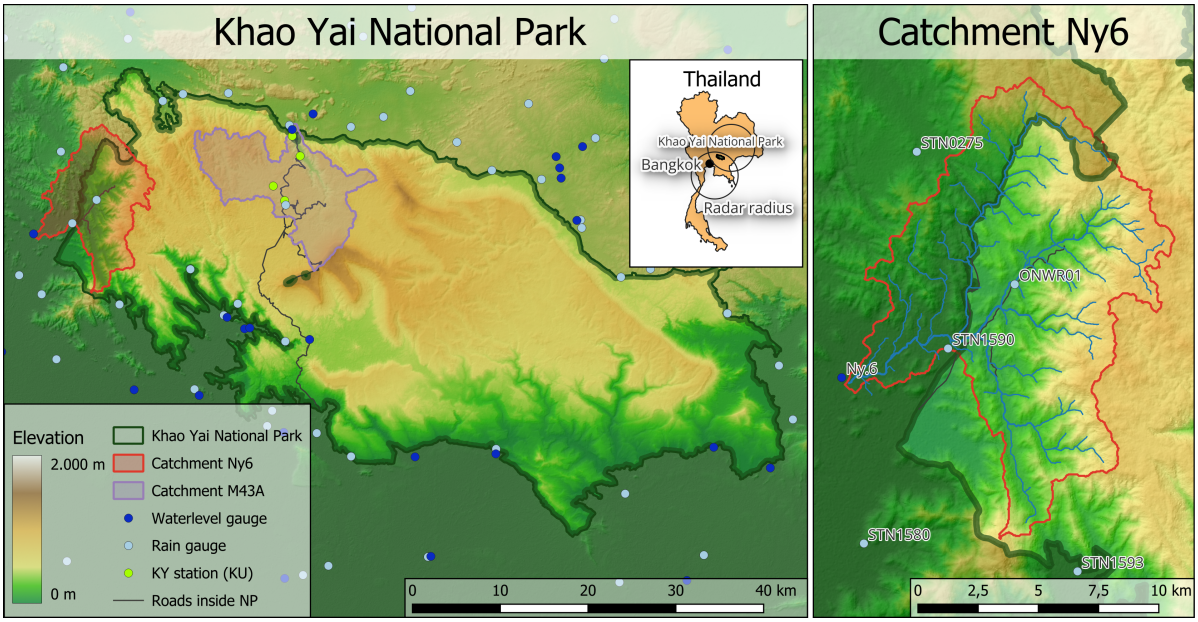

Figure 2.1: Study area: Khao Yai National Park (left) and catchment Ny6 (right).

statistically significant number for the landslide susceptibility analysis. Second, to assess antecedent conditions and temporal landslide occurrence, the study area was restricted to the gauged catchment Ny6 in the west of the national park which has an area of 127.2 km² (Figure 2.1). Within this catchment, landslide events have been frequently observed by National Park Rangers in recent years. Additionally, good road access facilitated field observations in this area.

2.1. Meterological and hydrological observations

The Thai Meteorological Department maintains a dense network of automated rain gauges around the national park (Figure 2.1) which records precipitation with a temporal resolution of 15 min. On average, this network records a mean annual rainfall of 1325 mm for northeastern Thailand (Thai Meterological Department, 2015). However, only two stations are located within the boundaries of the national park. These stations record a mean annual rainfall of 2326 mm (1993–2001), with more than 80 % of the precipitation falling in the rainy season from May to October (Kitamura et al., 2002). Due to this mismatch of recorded precipitation between the study area and the greater region, Kasetsart University has installed a low-cost sensor network (Figure 2.1) with automated rain gauges and soil moisture sensors in the study area to further investigate spatial rainfall patterns (Methaprayun et al., 2023). These observations are valuable additional information for the calibration of the weather radar composite for the study area.

In addition to the rain gauge network, the Royal Irrigation Department maintains a network of automated water level gauges at strategic locations (Figure 2.1). These stations record the water level with a temporal resolution of 15 minutes. The channel crosssections at the locations of the stations are recorded yearly. Through regular discharge measurements, individual rating curves are constructed every year (Royal Irrigation Department, 2024).

The chosen study catchment is determined by the outlet at water level gauge Ny6. Two automatic rain gauges are located within the catchment. Furthermore, six more rain gauges are located within 10 km distance of the catchment boundaries. Unfortunately, the automatic rain gauge experiences technical errors regularly. Therefore, observed rainfall time series were filtered through a double-mass curve analysis (Toet et al., 2023). However, at any time between 2017 and 2023, at least one of the two automated gauges within catchment Ny6 was functional.

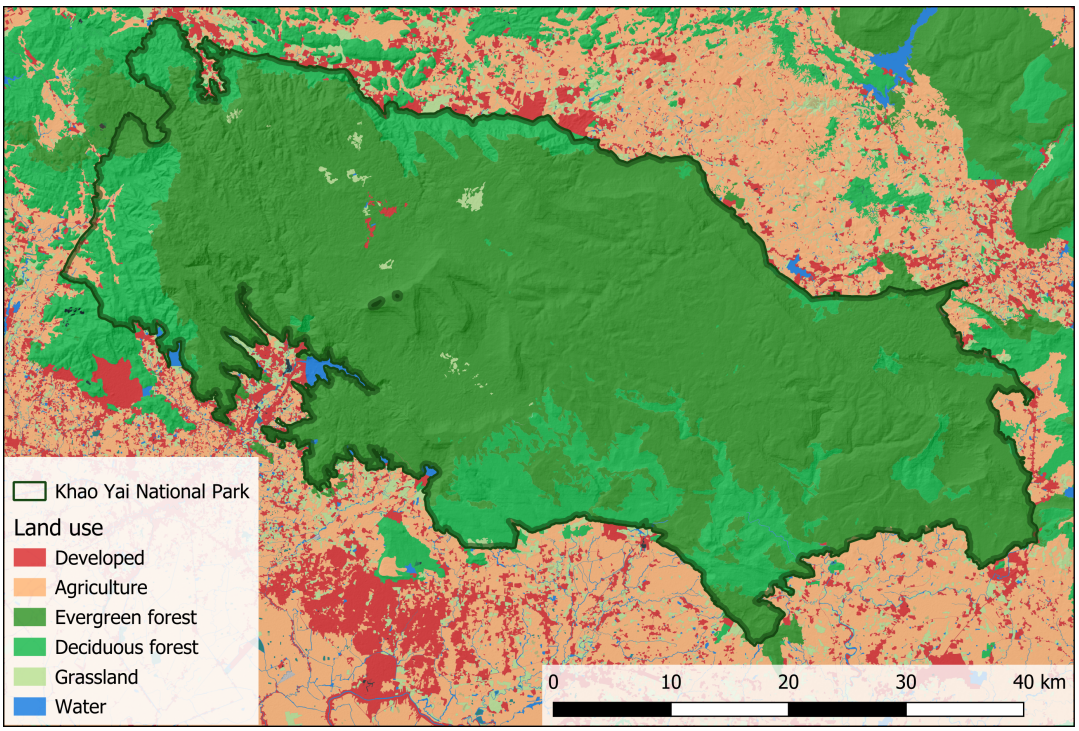

Figure 2.2: Land cover map of the Khao Yai National Park and its surroundings (Land Development Department, 2020).

2.2. Land cover

Land cover information is an important input for the analysis of spatial landslide occurrence. Furthermore, other parameters such as vegetation cover or surface roughness can be derived from land cover information, which are required parameters for the spatially distributed hydrological model. The Land Development Department of the Ministry of Agriculture and Cooperatives is responsible for soil mapping and land use planning in Thailand. The department therefore has a detailed land use map, containing 18 different categories of land use alone within the boundaries of the national park. These detailed land use categories were resampled into five categories to obtain a land cover map (Figure 2.2).

The study area is mostly undeveloped and almost fully forested, with an exception at the western edge of the park and the touristic developments around the visitor center of the national park. The main variation in land cover is due to vegetation. Higher elevation areas are covered in dense evergreen forest. In the lower areas the vegetation is dominated by deciduous forest. This is in strong contrast to the area surrounding the national park which is densely developed with residential areas and agriculture. Land use changes in the study area are minimal due to restrictions of the national park.

2.3. Lithology and soil type

Information about the subsurface is crucial for determining hydrological processes and assessing the failure probability of slopes. Spatial data on lithology and soil type is available for the whole country of Thailand in the national lithology and soil maps. These datasets allow for the derivation of further physical soil parameters based on literature values.

In the northwestern part of the park, the bedrock is primarily composed of volcanic rock from the Permian period (Figure 2.3). This region is characterized by small valleys with steep slopes. The southeastern part of the study area features a plateau of sedimentary rock, predominantly sandstone, from the Jurassic period. Along the northern boundary of the study area, this plateau ends in a 50 km long cliff along the Khao Yai fault (Ridd and Morley, 2011). Additionally, granite formations are present in the eastern part of the park.

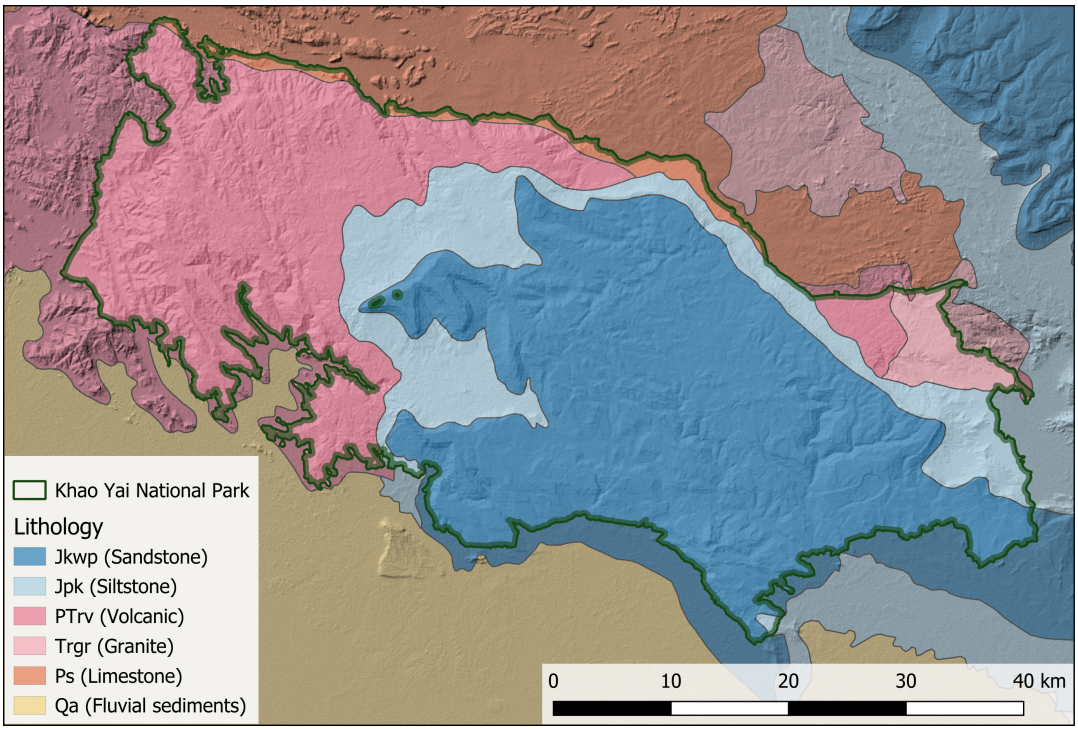

Figure 2.3: Lithology map of the Khao Yai National Park (Department of Mineral Resources, 2015).

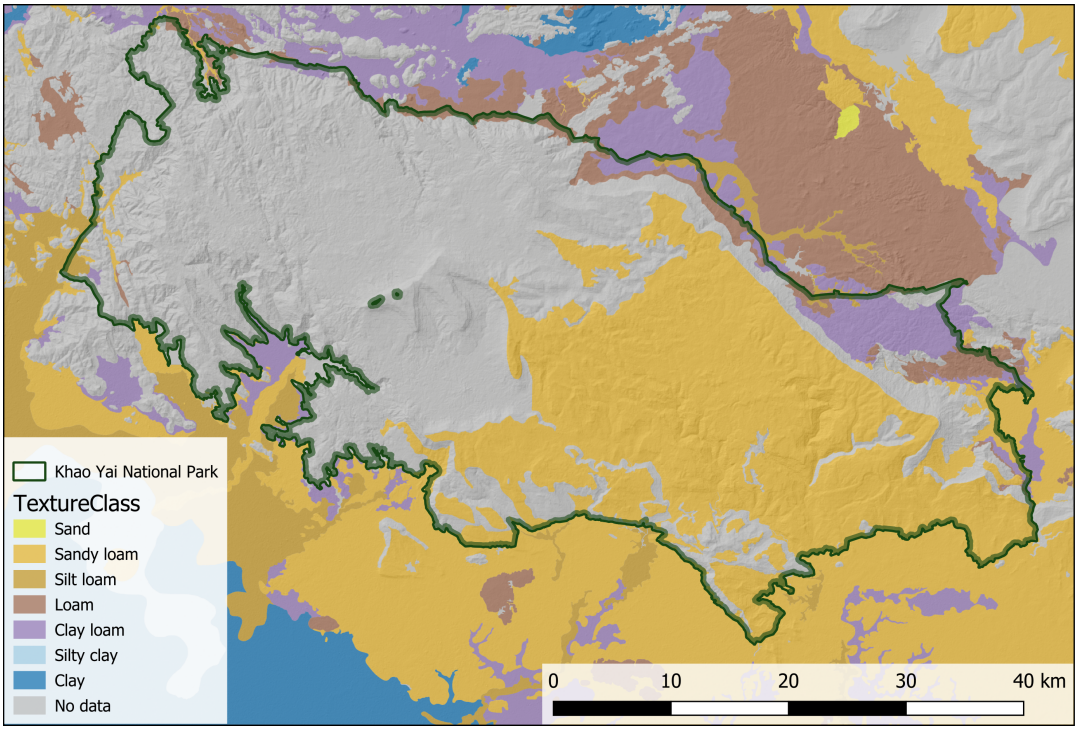

Figure 2.4: Soil texture class map of the Khao Yai National Park (Land Development Department, 2018).

Observations from historical soil surveys in Thailand, conducted by the Land Development Department, have been compiled into the Thai Soil Map. This map details the spatial distribution of soil types across the region. Unfortunately, large portions of the study area are marked as *unknown* (Figure 2.4). These unknown areas often correspond to complex slope regions where soil characteristics are crucial for assessing slope stability, as these are typically the locations where landslides are most likely to occur. The lack of data in these areas presents a challenge for analyzing spatial-temporal landslide occurrences. However, in the valleys where soil surveys have been performed, loamy soil is predominantly observed.

3

Landslide susceptibility

Landslide events are a common occurrence in the Khao Yai National Park. The local rangers know from experience which areas of the park are most affected and can report on different events based on their memory. However, these events are mostly not recorded in datasets. Therefore, a landslide inventory map needed to be constructed first, to create a basis for analyzing spatial landslide occurrence in the national park. Next to the landslide inventory map, a landslide susceptibility map is the most common form to determine landslide-prone areas. This map ranks the slope stability of an area in categories from stable to unstable based on predisposing factors without any temporal implication and shows where landslides may occur (Chacón et al., 2006).

3.1. Methodology

Historical records of landslides in the study area are rare and limited to single events. Furthermore, they can not be verified in the field due to the fast-growing vegetation in the study area. Therefore, a remote-sensing approach was chosen utilizing the large database of optical satellite images available on the Google Earth Engine platform to derive landslide events from sudden changes in vegetation cover. The landslide inventory is a crucial training dataset for the landslide susceptibility analysis.

A landslide susceptibility map is created by linking landslide-predisposing factors to landslide observations eg. a landslide inventory. In previous studies, a variety of methods have been developed to create such a susceptibility map reaching from GIS-based probabilistic approaches to machine learning applications. More complex methods do not necessarily lead to better results but mostly only favor certain aspects over others. Moreover, it has been shown that especially in data-scarce areas simple and robust methods outperform complex methods which require a higher data quality (Sun et al., 2018). Therefore, the frequency ratio method was chosen for this study, which is a robust method that has been used successfully in many previous studies (eg. Li et al., 2017, Vakhshoori and Zare, 2016 or Phạm et al., 2015).

3.1.1. Landslide inventory

To detect historical landslide events a pixel-based, optical approach was chosen adapted from the method of Scheip and Wegmann (2021). Due to its large open database of satellite images and its strong computational power, Google Earth Engine was used for the analysis. Scheip and Wegmann (2021) have developed a Google Earth Engine tool called HazMapper. This tool allows users to map natural hazard events such as landslides or wildfires for a specific day. They calculate the maximum NDVI from an optical image composite for a period before and after the event to detect sudden changes in vegetation that might be caused by a natural hazard. Then the rdNDVI is calculated using equation 3.1:

$$\text{rdNDVI} = \left(\frac{\text{NDVI}_{\text{post}} - \text{NDVI}_{\text{pre}}}{\sqrt{\text{NDVI}_{\text{pre}} + \text{NDVI}_{\text{post}}}} \right) \times 100 \tag{3.1}$$

$NDVI_{pre}$ and $NDVI_{post}$ are the NDVI images of the pre-and post-event greenest-pixel composites, respectively. By applying a threshold to calculated rdNDVI values, pixels are classified as positive with respect to event occurrence. Parameters such as the considered periods before and after the event or the rdNDVI threshold vary per event and therefore need calibration to produce reliable results. This method works especially well in areas with little human activity and therefore little to no land use changes.

For this study, the time period 2017 to 2023 was chosen, due to the fact that imagery from the Sentinel-2 mission is only available for this period. Sentinel-2 imagery is available in the Google Earth Engine database with a spatial resolution of 10 m and a temporal resolution of 5 days, given by the revisit frequency of the satellites. Next to Google Earth Engine, the GIS tool *QGIS* was used (Figure 3.1). In the first part, pixels with changes that are characteristic of landslides were detected with the Google Earth Engine script. In the second step, these pixels were grouped and filtered to eliminate noise and identify individual landslides. Indicated landslide locations were checked using Google Earth and high-resolution imagery from the GeoEye mission to verify the method.

To detect pixels with changes that are characteristic of landslides, the following steps were executed in the Google Earth Engine script. First, the harmonized version of the Sentinel-2 imagery was selected as imagery for this analysis. Due to a band shift in 2022, NDVI values before and after that shift are not comparable when using the original imagery. Using the pre-processed harmonized version of the

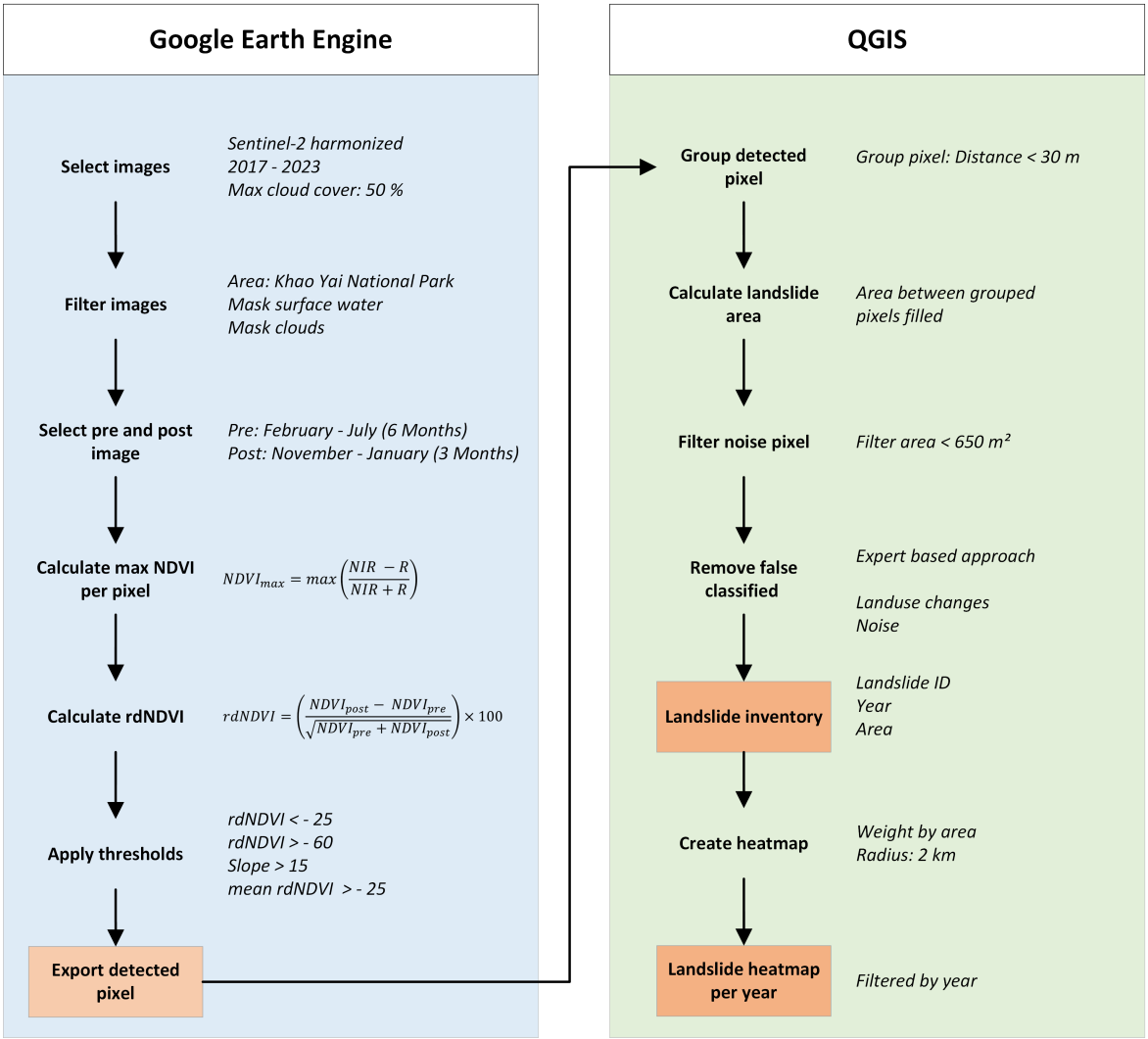

Figure 3.1: Workflow with Google Earth Engine and GIS to obtain the landslide inventory.

image collection, in which the bands are shifted back according to the old settings, solves this problem. Furthermore, using only images with a maximum cloud cover of 50 % proved to be an effective trade-off between minimizing noise caused by clouds and ensuring a sufficient number of images were available for analysis. The obtained image collection was then spatially confined by the extent of the study area and open water surfaces were masked using the JRC Global Surface Water dataset . To account for possible cloud coverage, the *maskS2clouds* algorithm was used to mask pixels with cloud coverage (Braaten, 2024). However, this algorithm is based on the *Q60 (Quality 60 m)* band of the Sentinel satellite, which has a 60 m spatial resolution. This means that single pixels with a higher resolution do not get masked as clouds if they are at the edge of a cloud-covered area and clouds do not cover the majority of their corresponding 60 m pixel. These pixels then create noise in the results and have to be filtered out in a further step (Scheip and Wegmann, 2021).

From the selected and filtered images, the rdNDVI value was calculated per pixel for every year. The method developed by Scheip and Wegmann (2021) requires the user to choose the date of the event. In this case, however, the date of the event is unknown. Therefore two approaches were tested to determine the period before and after for the calculation of the rdNDVI. The first tested approach was to calculate the rdNDVI for every day a Sentinel image is available by using six previous months and six coming months from the day of the overpass of the satellite for the calculation of the rdNDVI. The benefit of this approach is that the timing of a landslide is known within a time period of 10 to 15 days. However, due to heavy cloud cover during the rainy season from July to October, most images are not usable. Nevertheless, when looking at a specific location, instead of the whole study area, more images without cloud cover are available. The approach is therefore only preferred if more accurate information about the timing of a specific landslide is required. To detect landslides in the whole study area, a simplified approach was chosen in which the whole duration of the rainy season is defined as one event. The highest NDVI value from the 6 month period from February to July is therefore used as pre-event value while the highest value from the 3 month period from November to January is used as post-event value for the calculation of the rdNDVI. This second approach resulted in less noise in the results and allows for quick analysis of multiple years.

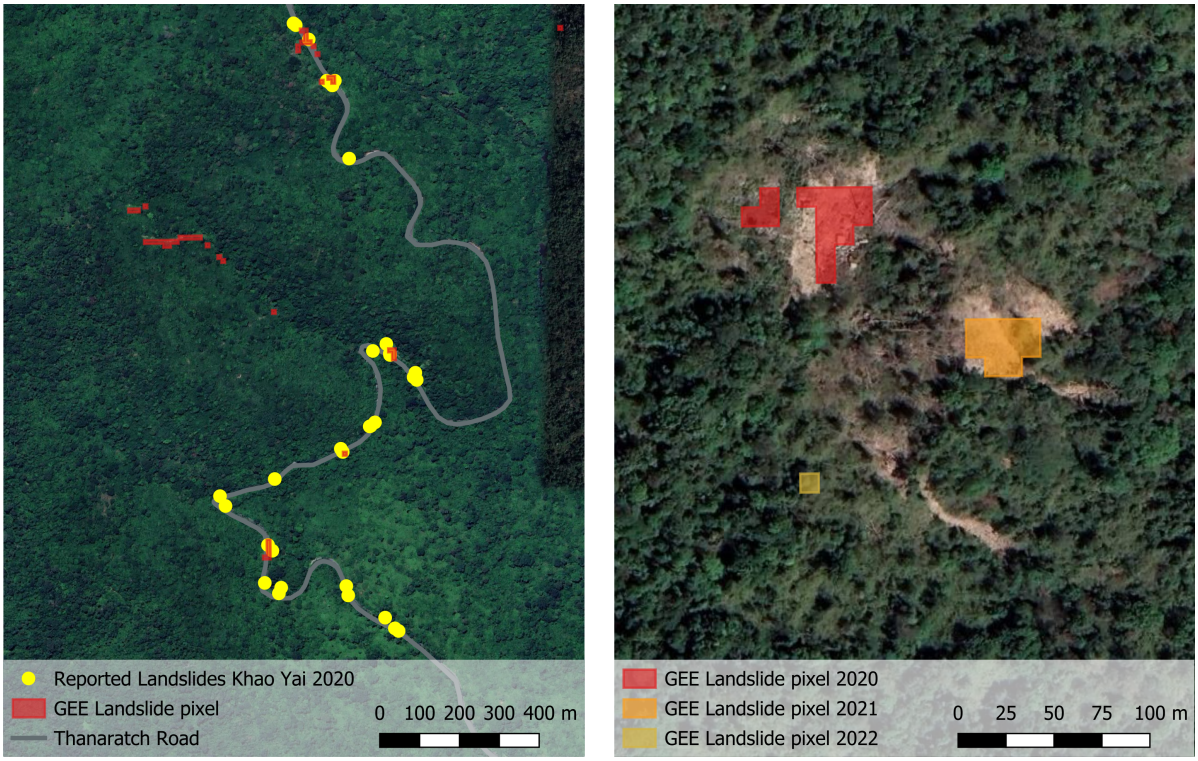

Figure 3.2: Expert-based calibration process of the Google Earth Engine landslide mapping algorithm by comparing the classified pixels with the 2020 landslide report (left) or visible landslides in GeoEye Imagery (right).

By applying multiple thresholds to the calculated rdNDVI map, possible landslide pixels were classified. These thresholds were the minimum and maximum rdNDVI as well as the slope. The value of the thresholds was determined in an iterative supervised calibration process by comparing the results to the landslide event of 2020 as well as large landslides which are clearly visible on Google Earth (Figure 3.2). The challenge is thereby to find a balance between having as little noise as possible while still detecting small landslides. The maximum rdNDVI and slope are the thresholds that delimit actual changes from the seasonal signal while the minimum rdNDVI filters noise due to cloud cover.

Detecting landslides in parts of the study area dominated by deciduous trees was more challenging compared to areas covered with evergreen forests (Figure 2.2). Deciduous trees in the study area drop their leaves at the beginning of the dry period, from November to April, which completely overlaps with the selected post-image period. As a result, steep areas covered exclusively by deciduous trees often fall within the thresholds and are consistently classified as landslides. To address this, these areas were excluded from the analysis by calculating the mean rdNDVI over the years 2017 to 2023. Pixels with a mean rdNDVI < -25 that fell within the classification thresholds were excluded from the results.

The detected pixels were then exported to manually filter the remaining noise and group pixels into single landslides. For that, pixels within a radius of three pixels were grouped, and the area between the pixels of a group was filled. By calculating the area and deleting groups < 650 m² (5 pixels, depending on spatial distribution) noise pixels were eliminated. The remaining groups were then checked manually with high-resolution satellite imagery. In this process, single landslides were deleted from the inventory based on an expert decision approach if they were falsely classified due to land use change or heavy noise. For each landslide, an ID, the year, and the area were added to complete the landslide inventory.

3.1.2. Frequency ratio method

To determine landslide susceptibility, the observed landslide events were linked to predisposing factors using the frequency ratio method. In this method, the complexity of each predisposing factor is simplified by dividing the values or categories into reasonable classes based on expert judgment. The frequency ratio value is then calculated for each factor using the prepared landslide inventory and the following formula:

$$\mathrm{FR} = \left[\frac{N_{\mathrm{pix}}(SX_i)/\sum_{i=1}^{m} SX_i}{N_{\mathrm{pix}}(X_j)/\sum_{j=1}^{n} N_{\mathrm{pix}}(X_j)} \right] \tag{3.2}$$

with:

$N_{\mathbf{pix}}(SX_i)$**:** The number of pixels containing landslide in a class
$N_{\mathbf{pix}}(X_i)$**:** The number of pixels in a class
$\sum_{i=1}^{m} SX_i$**:** Total number of landslide pixels
$\sum_{j=1}^{n} N_{\mathbf{pix}}(X_i)$**:** Total number of pixels

FR < 1 thereby indicates that a class is not significant for landslide susceptibility while FR > 1 indicates a significant class. From these calculated FR values significant predisposing factors are selected for further analysis. Furthermore, factors must be excluded if a correlation with another selected factor is detected. The landslide susceptibility index is then derived per pixel by summing the FR values of the significant factors:

$$\mathrm{LSM} = \sum_{j=1}^{n} \mathrm{FR}, \tag{3.3}$$

To create the final landslide susceptibility map the landslide susceptibility index is then further reduced into categories of susceptibility, typically from *Very low* to *Very high* by applying a calibrated threshold (Lee and Pradhan, 2007).

3.1.3. Factor selection

Due to given limits of the data availability of the study area, seven factors were selected for the analysis. Namely: Slope, Aspect, Elevation, Lithology, Landuse, Distance to road, NDVI, and Distance to stream (Appendix B). The factors Slope, Aspect, and Distance to stream were thereby derived from a digital elevation model (DEM).

Two datasets are available for the DEM. The first used dataset is the DEM obtained by the Shuttle Radar Topography Mission (SRTM) with a spatial resolution of 30 m by 30 m which was obtained in February 2000 (OpenTopography, 2013). The second dataset is a DEM obtained by ALOS-PALSER mission in the years 2006 to 2011 with a spatial resolution of 12.5 m by 12.5 m (ASF DAAC, 2014). While the ALOS-PALSER DEM has a higher spatial resolution than the SRTM, less measurement error and void filling corrections have been applied which results in more noise in the dataset. Therefore, factors that are derived from a DEM were derived from both available datasets (12,5 m and 30 m resolution). Furthermore, the median and maximum values of the NDVI of the NVDI were both included in the first analyses.

Multiple additional factors are often used in other studies such as soil type, curvature, distance to lineament, wetness index, and sometimes even annual precipitation (Regmi et al., 2014, Sun et al., 2018). Unfortunately, the factors soil type and depth could not be used due to the limited availability of spatial data (Figure 2.4). Other factors are not significant predisposing factors in the Khao Yai National Park according to previous analyses in the study area (Pimmasarn et al., 2022 and Chaikaew et al., 2023). Furthermore, once the three to five most significant predisposing factors are found, a higher number of factors does not improve the result of a susceptibility analysis (Kavzoglu et al., 2015 and Wang et al., 2015).

A pre-analysis was performed with these selected factors to find the factors that can be linked to landslide occurrence in the study area (Figure 3.3b). The mean and standard deviation in FR values between the different classes of each factor were calculated. Factors with a standard deviation in FR < 0.5 were excluded from the analysis because no significant difference between the classes could be found. Furthermore, the correlation between different classes was analyzed to ensure that all selected factors are independent (Figure 3.3a). If a correlation could be found, the factor with the smaller maximum FR

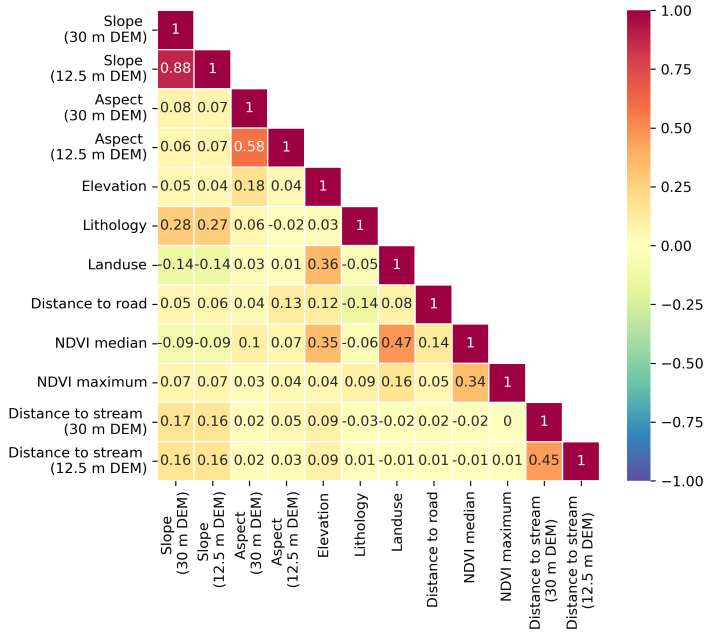

(a)

Factor	Max FR	Mean FR	Std FR
Slope (30 m DEM)	43.01	13.27	17.95
Slope (12.5 m DEM)	38.32	11.51	15.97
Aspect (30 m DEM)	2.52	1.05	0.68
Aspect (12.5 m DEM)	1.96	0.98	0.59
Elevation	1.48	0.93	0.32
Lithology	1.64	0.71	0.62
Landuse	3.12	1.56	1.43
Distance to road	4.96	1.75	2.15
NDVI median	15.62	6.40	6.75
NDVI maximum	11.81	6.46	5.51
Distance to stream (30 m DEM)	1.36	1.00	0.31
Distance to stream (12.5 m DEM)	1.60	0.97	0.42

(b)

Figure 3.3: Correlation between predisposing factors (a) and assessment of significance of pre-selected factors (b).

value was removed. To reduce the weight of the factor Slope, it was decided to use the factors derived from the 12.5 m DEM because more detail in the DEM results in lower FR values for slope and aspect. Finally, the factors (1) Slope, (2) Aspect, (3) Land use, (4) Lithology, and (5) Distance to road were selected for the calculation of the landslide susceptibility index (Equation 3.3).

3.1.4. Calibration and Validation

The creation of the landslide susceptibility map from the calculated landslide susceptibility index requires a calibrated threshold of landslide susceptibility. For the calibration of this threshold, the landslide pixels of the landslide were randomly split into 80 % calibration and 20 % testing datasets. Due to the limited size of the dataset, this was repeated 10 times to obtain a solid calibration. This was performed with all possible combinations of the five selected factors to analyze which factor combination gives the best fit to the observed landslides.

Next to the positive testing points of the landslide inventory, 3000 negative points were randomly sampled from the area where no landslides were detected during the creation of the landslide inventory. For every landslide susceptibility index threshold, the confusion matrix was then calculated which contains the true positives (TP), false positives (FP), true negatives (TN), and false negatives (FN) of the classification with a certain classification threshold. From the confusion matrix the precision, sensitivity, and specificity can be derived:

$$\text{Precision} = \frac{TP}{TP + FP} \tag{3.4}$$

$$\text{Sensitivity (True positive rate)} = \frac{TP}{TP + FN} \tag{3.5}$$

$$\text{Specificity (True negative rate)} = \frac{TN}{TN + FP} \tag{3.6}$$

By plotting the Sensitivity against 1 - Specitivity the receiver operating characteristic (ROC) curve can be constructed. With the area under the ROC curve the predictive ability of a model can be assessed and compared to different models (Mandrekar, 2010). Furthermore, from these metrics, the $F_\beta - score$ and the true skill statistic (TSS) can be calculated, which are both measures to evaluate the performance of a binary classification model with a specific threshold.

$$F_\beta = (1 + \beta^2) \cdot \frac{\text{Precision} \cdot \text{Sensitivity}}{(\beta^2 \cdot \text{Precision}) + \text{Sensitivity}} \tag{3.7}$$

$$\text{TSS} = \text{Sensitivity} + \text{Specificity} - 1 \tag{3.8}$$

The parameter β in Equation 3.7 is a weight factor to give the sensitivity a weight over the precision. In this case, a β-value of 1.5 was chosen to reduce the weight of size of the negative observations which was 10 times larger than the dataset of positive observations used for validation. The threshold for landslide susceptibility was then derived by finding the threshold for which the F_β-score and TSS are at their maximum (See example in Figure 3.4b).

The classification of landslide susceptibility indexes into susceptibility classes from *Very low* to *Very high* is an expert decision and therefore always biased. However, to reduce this bias the calculated threshold and the frequency of the landslide susceptibility index were used for the classification. Thereby the calculated threshold forms yields the boundary between the category *Low susceptibility* and *Moderate susceptibility*. The other two boundaries were determined visually from the histogram of pixel value frequency (Figure 3.4a).

This calibration-validation process was then repeated for all possible combinations of the five selected predisposing factors. Susceptibility maps were thereby also created for combinations of only two, three, and four factors. Through this, it could be identified if all selected factors are significant, or if landslide susceptibility can be described by a smaller group of predisposing factors.

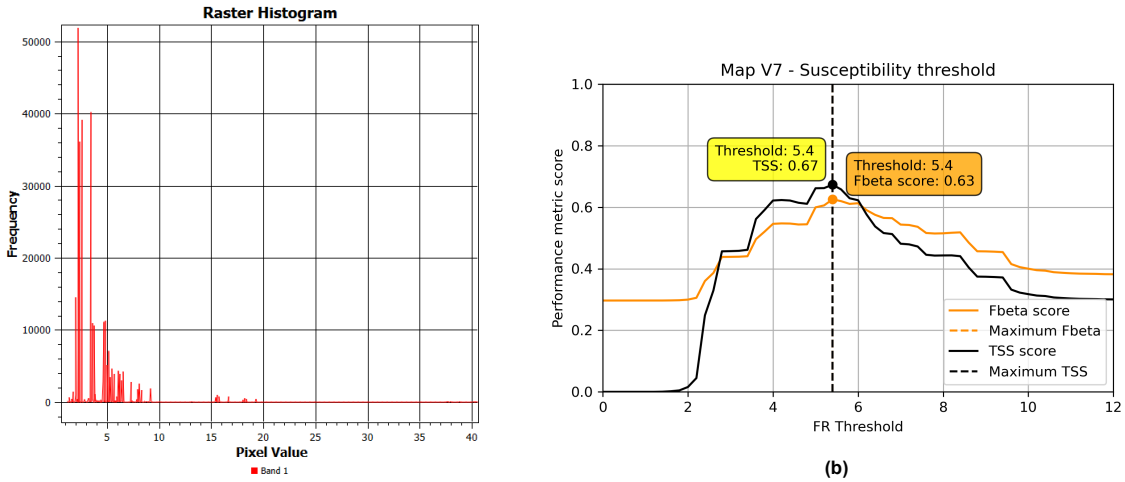

Figure 3.4: Frequency of FR values (left) and True Skill Statistic (TSS) and F_β score over different detection thresholds (right).

3.2. Results

The spatial occurrence of landslides in the study area is presented in two different maps. The landslide inventory map shows the locations of observed landslides from 2017 to 2023. The derived landslide susceptibility map illustrates areas susceptible to landslides based on the identified predisposing factors.

3.2.1. Landslide inventory

A total of 142 landslides could be detected for the years 2017 to 2023 using remotely sensed changes in vegetation cover (Figure 3.5). Each landslide was given an ID and the area of the landslide was calculated (Table A). The method of calculating the rdNDVI thereby does not allow to differentiate between the initiation and the runout zone of the landslide. All landslides with an area of > 1000 m² could be manually verified using Google Earth.

When comparing events of single years, differences in the number of observed landslides, the size of landslides, and their spatial distribution can be recognized. During the years 2020 and 2022, the highest number of landslide events was observed (Table 3.1). In 2020, most of the recorded events occurred in the northwest of the park, while in 2022, the events were concentrated in the southwest (Figure A.1). Larger landslides were observed in 2022, with the largest one reaching a length of 200 m and a width of 50 m. In 2017 and 2021, only about 10 landslides were detected. However, the size of the largest landslides recorded during these years was significantly larger than the largest landslide recorded in 2020. Since potential damage increases with landslide size, these years remain important, even though the number of observed landslides was relatively small.

Year	Landslides	Mean area	Max area
2017	11	1904 m²	6308 m²
2018	2	802 m²	925 m²
2019	27	1309 m²	3422 m²
2020	43	1340 m²	3902 m²
2021	9	1710 m²	5101 m²
2022	47	1524 m²	8592 m²
2023	3	1865 m²	3065 m²

Table 3.1: Number and area of detected landslides per year.

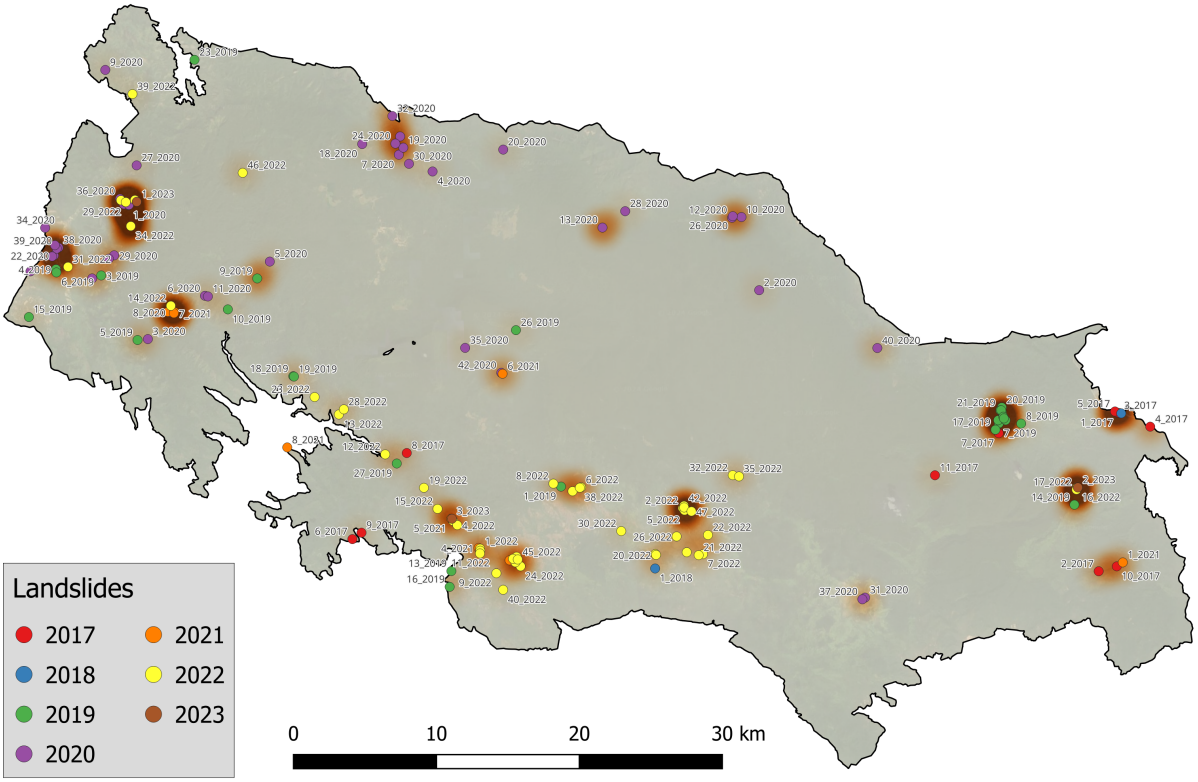

Figure 3.5: Landslide inventory map showing locations of observed landslides and hotspots of occurrence.

3.2.2. Landslide susceptibility map

The results of the analysis of landslide predisposing factors give insight into why spatial differences in landslide occurrence could be observed. In the pre-analysis, the five significant landslide predisposing factors Slope, Aspect, Land use, Lithology, and the Distance to road were identified (Table 3.2). All of these factors contain at least one class which indicates a significant FR of landslide occurrence compared to the other classes of the factors. For other analyzed factors such as Elevation or Distance to stream this could not be found (Table B.1).

The results for the calculated FR values of the factor slope indicate that landslide susceptibility increases with steeper slopes. Slopes with an angle of less than 15° are not susceptible to landslides. If the aspect of a slope in the study area is north-facing, the susceptibility to landslides increases. Additionally, landslides are more likely to occur in areas with volcanic lithology. Two landslide classes with high FR values for landslide occurrence were identified. In areas with deciduous forests, the likelihood of observing a landslide is more than three times higher than the average. A similar FR value was calculated for open field areas. The second most significant factor for landslide susceptibility, after steep slopes, is the distance to roads. Within a 50-meter proximity to a road, the susceptibility to landslides is five times higher than in other areas.

To derive the landslide susceptibility map for the Khao Yai National Park, all possible combinations of the identified predisposing factors were tested (Appendix C). Thereafter, using the factors Slope, Aspect, Land use, and Distance to road was identified as the best combination when comparing the resulting susceptibility map with the landslide inventory. The factor lithology is therefore not included in the final susceptibility map (Figure 3.6) because it does not add any valuable information. Similarly good results could be archived when further reducing the number of factors, not including the Distance to road or even only considering Slope and Land use (Table C.1). However, this decreases the performance of the classification along the roads, where correct classification is most important.

Table 3.2: FR value per class for significant factors.

Factor	Class	Landslide area [km²]	Landslide ratio [%]	Class area [km²]	Class ratio [%]	FR
Slope (12.5 m DEM)	< 15°	0.0216	11.09	1551.46	70.31	0.158
	15° - 25°	0.0566	29.06	436.83	19.8	1.468
	25° - 35°	0.0544	27.93	176.24	7.99	3.496
	35° - 45°	0.0465	23.87	37.37	1.69	14.094
	> 45°	0.0157	8.06	4.64	0.21	38.323
Aspect (12.5 m DEM)	Flat	0.0064	3.29	166.66	7.56	0.435
	N	0.0715	36.76	414.06	18.78	1.957
	E	0.0461	23.7	502.53	22.8	1.04
	S	0.036	18.51	635.48	28.83	0.642
	W	0.0345	17.74	485.79	22.04	0.805
Landuse	Desigous forest	0.1144	58.82	416.34	18.87	3.117
	Developed	0.0001	0.05	5.16	0.23	0.22
	Evergreen forest	0.0754	38.77	1763.05	79.92	0.485
	OpenField	0.0046	2.37	21.6	0.98	2.415
Lithology	Sandstone	0.0593	30.49	1031.15	46.77	0.652
	Siltstone	0.0287	14.76	340.43	15.44	0.956
	Volcanic	0.105	53.98	726.48	32.95	1.638
	Limestone	0.0008	0.41	51.43	2.33	0.176
	Granite	0.0007	0.36	55.03	2.5	0.144
Distance to road	< 50 m	0.0106	5.45	24.23	1.1	4.958
	50 m - 100 m	0.0007	0.36	23.48	1.07	0.338
	100 m - 200 m	0.0031	1.59	46.42	2.11	0.757
	> 200 m	0.1801	92.6	2110.39	95.73	0.967

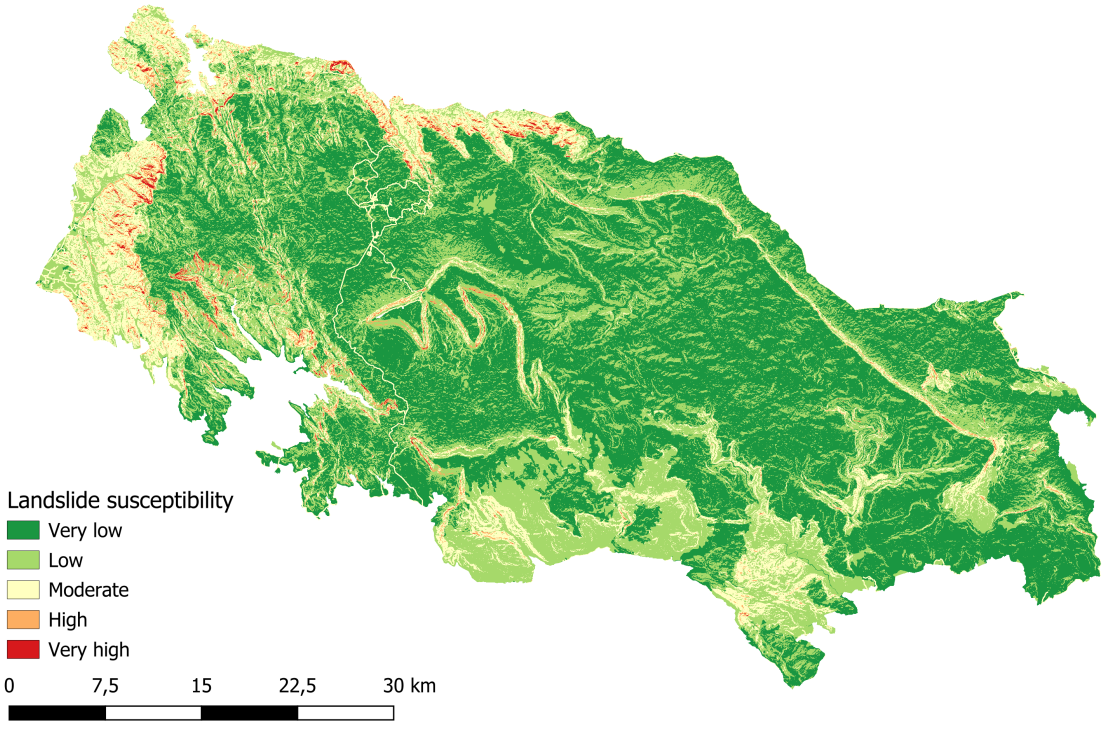

Figure 3.6: Susceptibility map of the Khao Yai National Park derived from the four predisposing factors Slope, Aspect, Land use, and Distance to Road.

To evaluate the classification result the ROC curve was constructed from the testing samples for each calibration/testing run (Figure 3.7). To assess the quality of the classification the area under the curve (AUC) is calculated. An AUC of 0.5 indicates a random classifier while an AUC of 1.0 is achieved with a perfect classification. For the selected combination of parameters a mean AUC of 0.9, which is considered an excellent to outstanding classification (Mandrekar, 2010). All 10 calibration runs could achieve similar results which indicates a robust classification. Overall, a true positive rate of 80.23 % and a false negative rate of 19.77 % was achieved, which translates into a mean TSS of 0.67 for the testing samples which indicates a good classification (Achu et al., 2023). Furthermore, 16.3 % of the study area can be considered susceptible to landslides, with 13.7 % having *moderate*, 2.2 % *high*, and 0.4 % *very high* susceptibility (Table C.2).

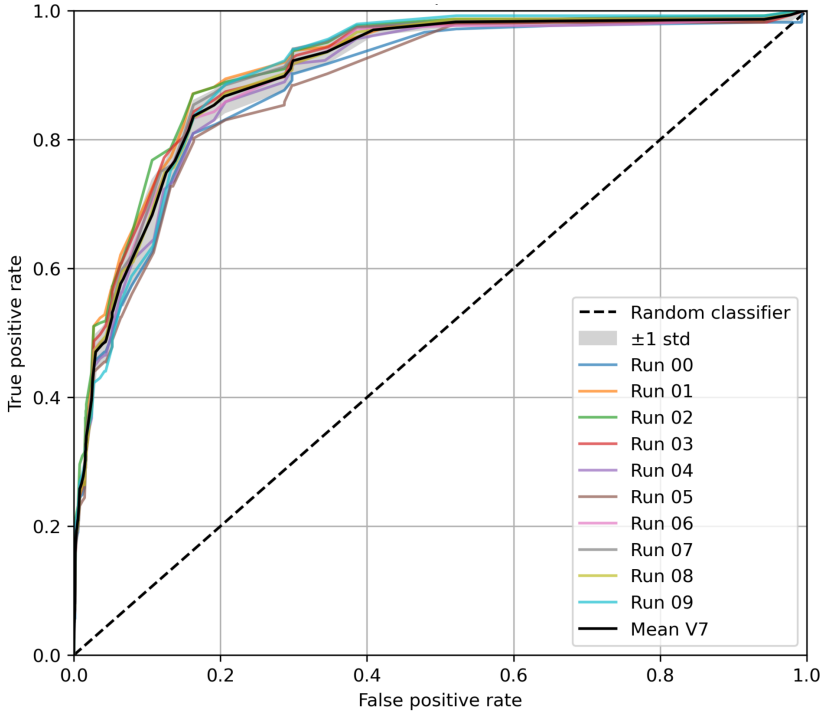

Figure 3.7: ROC curve of the susceptibility map (Mean AUC: 0.90).

3.3. Discussion

Five factors were identified as predisposing factors for landslide occurrence in the Khao Yai National Park. The identified factors Slope angle, Aspect, Land use, Lithology, and Distance to road are thereby common factors also found in susceptibility analysis in other study areas (eg. Sun et al., 2018 or Silalahi et al., 2019). However, the class *deciduous forest* of the factor Land use, for which an FR value of 3.12 was calculated, is unusual. In other study areas, forested and even sparsely forested areas are found to reduce landslide susceptibility (eg. Vakhshoori and Zare, 2016 or Sun et al., 2018). Especially in the rainy season, during which deciduous trees carry leaves, one would not expect a large difference to evergreen forests for which an FR value of 0.48 was calculated.

A potential explanation for the high FR value in areas dominated by deciduous trees could be that landslide susceptibility is not directly related to the vegetation type, but rather to the environmental conditions that favor the growth of deciduous trees. An investigation into the distribution of deciduous and evergreen trees in the study area revealed a link between soil water regimes and vegetation type. In areas with deciduous trees, soil water availability is limited during the dry season, preventing the trees from maintaining transpiration (Murata et al., 2012). However, during the wet season, the effect of the limited storage capacity would be reversed, leading to quicker saturation and the rapid buildup of excess pore water pressure, which can trigger landslides (Greco et al., 2023).

The derived susceptibility map demonstrates a robust classification with a mean AUC of 0.91, indicating an *excellent* classification. However, the calculated TSS of 0.67 suggests only a *good* fit for the classification model (Achu et al., 2023). It's important to note that AUC and TSS measure different aspects of the model's performance. AUC assesses the classification independently of any threshold, while TSS evaluates the model's performance based on a specific threshold. Consequently, TSS may be lower when there is no distinct boundary between positive and negative samples, even though the AUC remains high (Achu et al., 2023). To further improve the model, it is therefore most useful to focus on susceptibility indexes that are near the defined threshold.

One aspect that causes incorrect classifications of landslide susceptibility indexes with values close to the defined threshold is the simplicity of the frequency ratio model. Even though many studies have shown that the frequency ratio method can compete with more advanced statistical methods or machine learning approaches (e.g., Yilmaz, 2009 or Vakhshoori and Zare, 2016), it still has limitations. Since the landslide susceptibility index is calculated by summing the FR values of all factors without applying further constraints, this can lead to the classification of an area as susceptible to landslides when it is not physically possible. For example, in the case of Khao Yai National Park, a deciduous forest area within 50 meters of a road combined with volcanic rock lithology is statistically classified as susceptible to landslides, even if the terrain is flat at this location. However, this issue only impacts a small fraction of the study area. When evaluating the model performance with the AUC of the ROC curve, this aspect does not significantly influence the calculated performance value. This can also be observed in evaluations of modified frequency ratio methods that address this issue (Li et al., 2017). The frequency ratio method therefore overestimates landslide susceptibility and can be called a conservative method.

Another important aspect that influences the performance of the classification is that the landslide inventory used for training and validation contains uncertainties, which propagate into the evaluation of the susceptibility model's performance. Assuming that the automated landslide mapping method is not perfect, it is expected that incorrectly detected landslides may still be included in the landslide inventory. If these incorrectly detected landslides are included in the validation dataset but are not in a location classified as susceptible to landslides, they increase the number of *false negative* predictions. Consequently, incorrectly classified landslides in the landslide inventory decrease the calculated sensitivity of the susceptibility classification even though the "true sensitivity" is higher.

A similar effect on the *false positive* predictions of the susceptibility analysis is caused by the limited size of the landslide inventory. Due to the restricted temporal resolution of the satellite imagery, the landslide inventory only contains observations from the past 7 years. Consequently, the area of observed landslide nonoccurrence is widely overestimated (Lucchese et al., 2021). The random selection of nonoccurrence samples therefore includes a significant number of samples located in susceptible areas. This leads to an overestimation of *false positive* predictions and, therefore, reduces the calculated specificity of the susceptibility model. While this is a common issue affecting all susceptibility analysis studies (Lucchese et al., 2021), it becomes especially notable when evaluating susceptibility predictions based on a small landslide inventory with the TSS.

Taking these effects into account, the derived susceptibility map can be considered the result of an excellent classification. Overall, the presented methodology is a relatively simple and robust approach for quickly creating a landslide inventory over a large area, with performance comparable to similar methods (Amatya et al., 2022). Furthermore, the size of the analyzed area could be extended to a province or even an entire region without significant additional effort. However, a reduced performance should be expected, as the method is affected by land use changes and performs particularly well in forested areas. Additionally, the methodology is biased toward detecting large landslides visible in optical satellite imagery, potentially underestimating the exposure to smaller landslides, which can also cause significant damage. Therefore, the suitability of this methodology must be assessed individually for each location.

4

Field observations

In May 2024 a three week field visit was conducted to the Khao Yai National Park to gain an impression of the study area to be able to better justify assumptions in the modeling phase of the project. Furthermore, soil samples were taken in the area in which the Thai soil map shows *no data*. The sample locations were thereby focused on areas that were identified to be susceptible to landslides, as for these locations, information about the characteristics of the subsurface was most important. During the field visit, two parts of the Khao Yai National Park were visited, which had been identified as hot spot areas for landslide events based on the susceptibility map. One of these areas is the main road of the national park leading from the main entrance in the north to the visitor center in the middle of the park. The whole section of the road lies within the catchment M43A and has experienced a major landslide event in October 2020. The area is well developed for tourism, which makes it easy to move around by vehicle to visit a wide variety of places and take samples with a large spatial distribution (Figure 4.1a). The other visited area is catchment Ny6. This area of the national park is not developed and is only accessible on foot, accompanied by a local ranger (Figure 4.1b). This makes it difficult to visit a variety of places within the catchment to collect samples with a large spatial distribution.

(a) Catchment M 43A

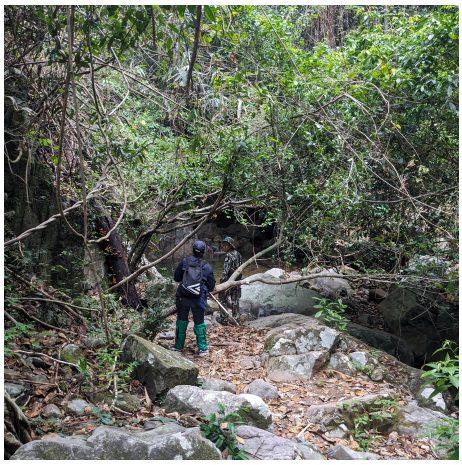

(b) Catchment Ny6

Figure 4.1: Visited study catchments with different states of development for tourism.

4.1. Data collection in the field

A total of 13 locations were selected for field observations (Figure 4.2). These locations were chosen either because of the Khao Yai measurement stations of Kasetsart University or because of historical landslide activity in those areas. The soil type was determined at all sample locations in the field. Where possible, hydraulic conductivity was measured in the field, and soil depth was estimated. Furthermore,

samples were taken for further analysis in the soil laboratory at Kasetsart University in Bangkok. In the laboratory, the shear strength of the soil was measured using a direct shear test, and the texture class was determined in the lab to verify the field tests. Additionally, landslides were mapped in the field as validation for the landslide inventory and the susceptibility map.

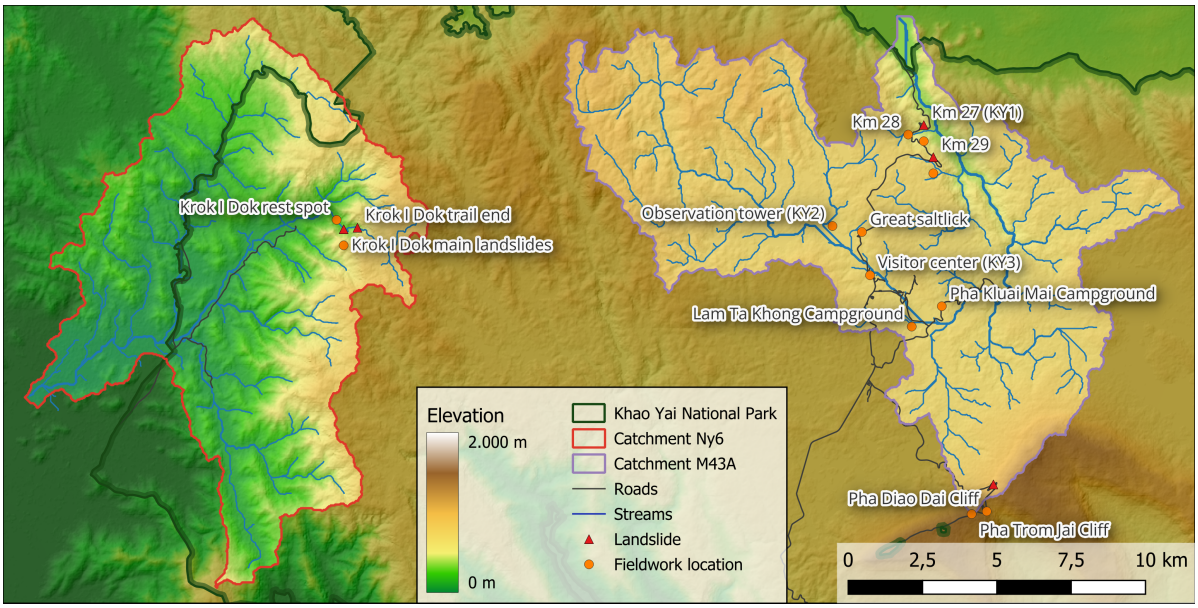

Figure 4.2: Fieldwork locations of three field visits to the Khao Yai National Park.

4.1.1. Soil observations

Texture class

The soil texture class was determined at 13 different locations in the field (Figure 4.2): 10 locations in catchment M43A and three in catchment Ny6. To determine the texture class in the field, a field test was used following the German soil mapping instructions (5th edition) (Eckelmann et al., 2005). This test can be performed by rolling the moist soil between both hands to estimate the cohesion. Through further indicators, the soil type can be classified into one of 21 groups. This allows an estimation of the texture class distribution with an accuracy of 5 % in the field, provided the person conducting the test is familiar with the procedure (Blume et al., 2016). Because of its simplicity, this test allowed for a larger spatial distribution compared to common soil sampling and analysis in the lab.

To validate the field method, samples were taken at the sample locations next to KY2 and KY3 in the field (Figure 4.2). One sieve with a 0.05 mm mesh opening was used to separate the sand fraction from the smaller fractions. Then, a hydrometer test was prepared to determine the silt and clay portions. Furthermore, raw data from sieve and hydrometer tests conducted in 2022 was used to determine the grain size distribution of three of the sample locations. The field laboratory results were then compared with the results of the field test to validate the accuracy of the field method.

Soil depth

Soil depth is one of the most important parameters when modeling landslides, yet almost no data is available on it. Therefore, the goal was to determine the soil depth at as many places as possible to calibrate a steady-state soil depth model following Von Rütte and Or (2013). Due to field heterogeneity and the presence of large rock fragments in the soil, manual augering to assess soil depth was not feasible (Figure 4.3a). Instead, soil depth was estimated in the field at locations where the soil profile was visible due to cuts in the landscape or rock outcrops (Figure 4.3b). This method strongly limited the spatial variability of observations but was still useful for a preliminary estimation of the soil depth.

(a) (b)

Figure 4.3: Soil depth estimation in the field (a) using a manual hand auger and (b) visible soil profiles in the field.

Shear strength

Next to soil depth, the shear strength parameters cohesion and angle of internal friction are the most important factors in determining slope stability (Milledge et al., 2012). Therefore, soil samples were taken at two landslide locations to determine the shear strength in the lab. At the landslide at km 27, near the measurement station KY1 (Figure 4.2), one set of five samples was taken from the slip surface of the landslide and another set from a location adjacent to the landslide. Another set of samples was taken from the runout material of a landslide in catchment Ny6 (Figure 4.2).

In the laboratory, rocks were removed from the samples (Figure 4.4b). The samples were then remolded to ensure an equally distributed density. The direct shear test was performed using an automatic shear machine, following the *Standard Test Method for Direct Shear Test of Soils Under Consolidated Drained Conditions* (ASTM, 1994). Each sample was first saturated and consolidated for 24 hours. The minimum required shear velocity was then calculated from the measured time required to reach 90 % consolidation. Thereafter, the shear velocity was set to 0.1 mm/min over a shear distance of 7.5 mm, which was sufficient for all samples to avoid pore pressure buildup according to the measured consolidation time. For the applied normal stress, stages of 31 kPa, 62 kPa, and 124 kPa were chosen based on the estimated pre-consolidation of the sample. These stages correspond to an expected slip surface depth of 2 m, 4 m, and 8 m.

(a) (b)

Figure 4.4: Direct shear test in the laboratory (a) using remolded samples due to stones in the undisturbed samples (b).

Hydraulic conductivity

Two inverse auger hole tests were performed on the plateau in catchment M43A, near the measurement stations KY2 and KY3 (Figure 4.2), to determine the hydraulic conductivity. The soil type at these locations ranges from clay to silty loam, with rocks being less abundant than in sandy soil types. On the slopes with sandy soils, no test could be performed due to the high abundance of rock fragments and the shallow soil depth. In catchment Ny6, no test could be performed because no location was found where it was possible to drill a hole of sufficient depth.

For the inverse auger hole test, a 50 cm deep hole with a diameter of 4 cm was drilled using a hand auger. The hole was then filled with water, and the drawdown of the water table was recorded every 5 seconds using a pressure diver located at the bottom of the filled borehole. From the measured drawdown, the hydraulic conductivity k_{sat} was determined using the following equations (Hoorn, 1979):

$$k_{sat} = 1.15 * r * \tan\alpha \tag{4.1}$$

$$\tan\alpha = \frac{\log(h_0 + \frac{r}{2}) - \log(h_t + \frac{r}{2})}{t} \tag{4.2}$$

from the radius of the whole r, the water level in the auger hole at the beginning of the measurement h_0, the water level in the hole at the end of the measurement h_t, and the measurement time t. The angle α can also be determined by plotting the observations in a semi-logarithmic space.

At the visitor center (KY3), the test was repeated three times to ensure the soil was saturated. At the observation tower (KY2), the test could only be performed once due to the long duration required because of the clayey soil and its remote location. Consequently, the soil was not fully saturated throughout the duration of the test.

4.1.2. Landslides

During the selection of the field sites, emphasis was placed on known locations identified as landslides in the landslide inventory. By visiting these locations, the records in the landslide inventory could be verified. In addition to the known locations, several small, undetected landslides were discovered in the field with the guidance of the National Park Rangers. Although most landslides are not officially documented, the local rangers are aware of their occurrence and locations (Figure 4.5b). Most of these locations are not accessible due to steep slopes and dense vegetation. However, they could still be observed and documented from a distance (Figure 4.5a). When accessible, the slope angle and length of the slip surface were measured.

(a) (b)

Figure 4.5: Landslide observations in the field (a) and determination of their location on the map of the National Park (b).

4.2. Field observations and laboratory results

The soil type was determined in 12 different locations spread across the study area during the field visit (Figure 4.6). In forested areas on the plateau in catchment M43A, silty loam was found in all but one location. In the open field area around the observation tower (station KY2), the dominant soil type was clay. This area also features multiple small lakes. At locations with steeper slopes, exclusively sandy loam was found. At all of these locations, the vegetation was also dominated by deciduous trees. The field test method was verified at three locations (km 27, km 29, and KY2) with laboratory analysis of soil samples taken from the same location (Figure D.6). Thus, samples from a location determined as sandy loam, silty loam, and clay were analyzed in the laboratory. The results from the laboratory thereby matched the results from the field test at all three locations.

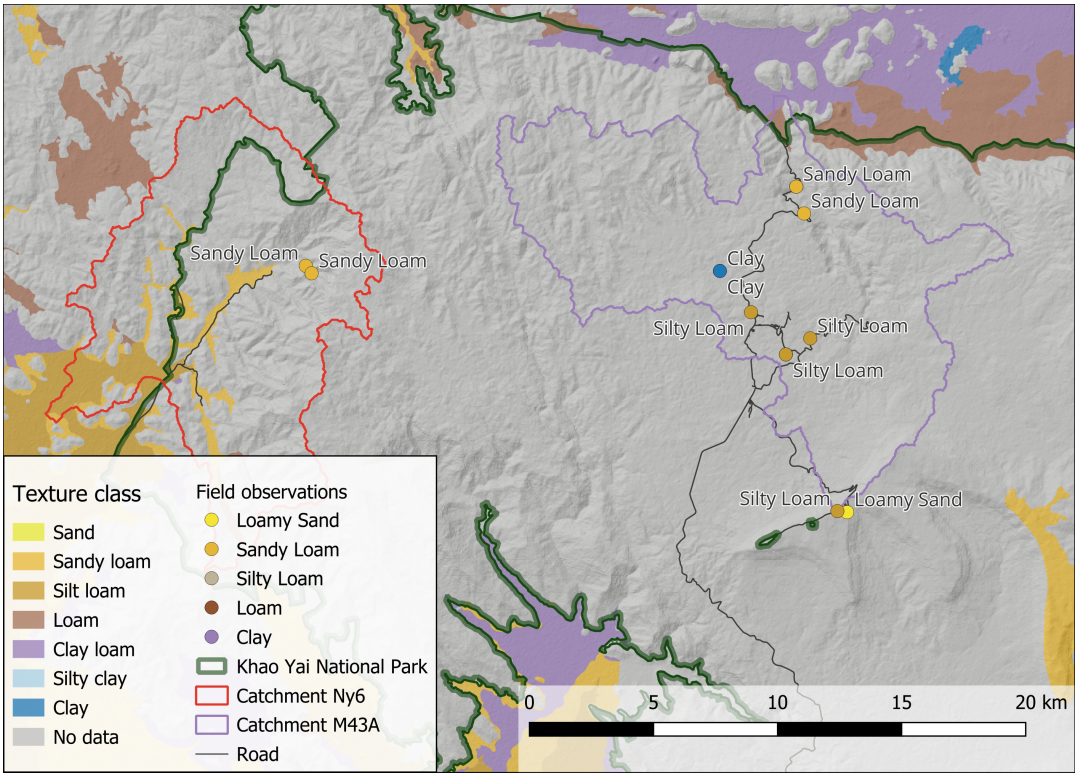

Figure 4.6: Field observations on soil texture class in study catchments Ny6 and M43A.

The auger hole test was performed at the observation tower (station KY2) and the visitor center (station KY3), where clay and silty loam soil were observed, respectively. The drawdown measured in the clayey soil translates to a hydraulic conductivity of 7.3×10^{-6} m/s (Figure 4.7). The drawdown in the loamy soil results in a hydraulic conductivity of 4.6×10^{-5} m/s. Both values are therefore in the center of the range of common values for hydraulic conductivity for the respective soil type (Blume et al., 2016).

Under fully saturated conditions in homogeneous soil, the drawdown observations plot in a straight line in semi-logarithmic space (Hoorn, 1979). At station KY3, this could be achieved after three repetitions of the test. Only the drawdown of the first 15 cm deviates from the line, which indicates that the upper layer of the soil was still not fully saturated. In the clayey soil at station KY2, the test was performed only once due to the slow drawdown. For this test, an accelerated drawdown could be observed over time. This could be due to multiple reasons. Smearing of the borehole walls from the hand auger influences the hydraulic conductivity. If closed pores reopen during the experiment, accelerated infiltration can be observed, as was the case in the experiment with clayey soil. Another possibility is a layered soil with higher hydraulic conductivity at the bottom part of the borehole than at the top. However, this explanation is unlikely based on the observation of the material extracted from the borehole. The increasing saturation of the soil around the borehole would suggest a decreasing hydraulic conductivity during the experiment and therefore cannot explain the observations.

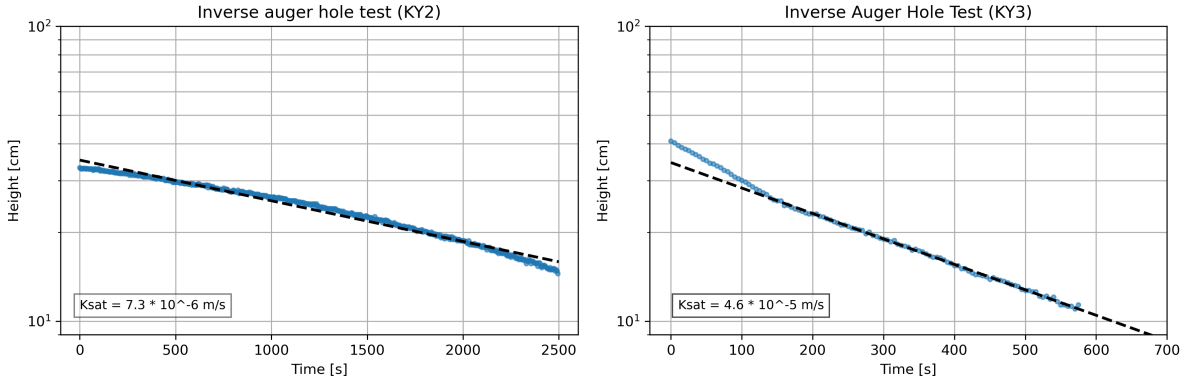

Figure 4.7: Inverse Auger Hole Test in clayey soil (left) and loamy soil (right).

The shear strength of samples taken from three locations was analyzed in the lab. Due to the soil's texture class and the remolding of the sample, no peak strength was observed, and only residual strength could be measured (Figure 4.8). The measured residual shear stresses for the different applied normal stresses of the sample set taken next to the landslide at km 27 all plot in one line and result in a measured cohesion of 15.5 kPa and an angle of internal friction of 33.9° (Figure 4.8). The analysis of the other two sample sets leads to similar results (Figure D.9 and D.10). The fact that all pairs of measured shear stress and normal stress plot on one line indicates a good quality of the laboratory test results (ASTM, 1994). The obtained results are therefore comparable to typical values for the soil type *sandy loam* (Dysli, 2000 and Minnesota Department of Transportation, 2007).

Using these measured values, a landslide back analysis was performed using the infinite slope assumption (Milledge et al., 2012) and landslide dimensions measured in the field. For the landslide at km 27, a slope angle of 38° and a slip surface depth of 0.8 m were observed. The calculation of the factor of safety showed that, based on the infinite slope model, a slope failure would be impossible with the shear parameter values measured in the laboratory and the landslide dimensions measured in the field, even under fully saturated conditions (Appendix H). This suggests that the shear strength parameters measured in the laboratory are not representative of real conditions in the field.

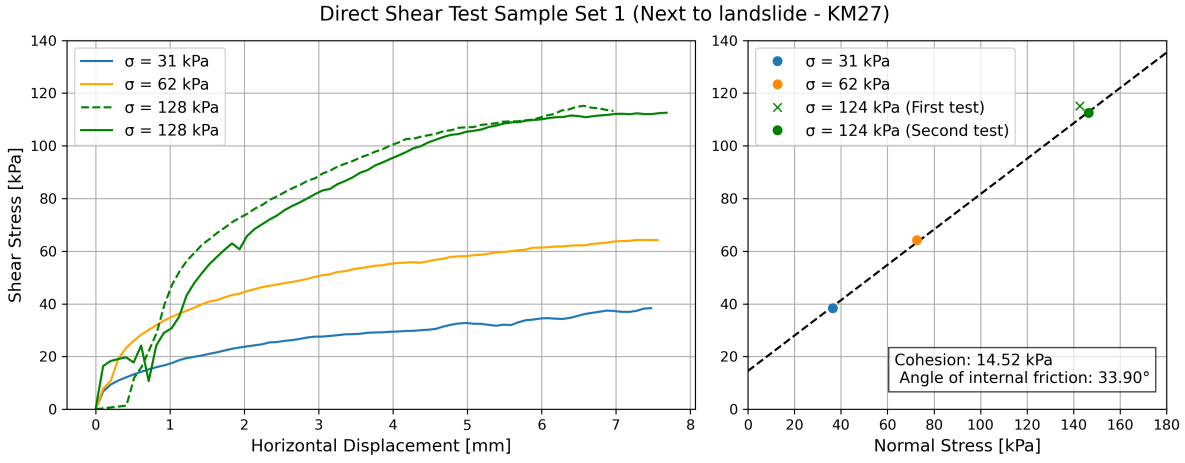

Figure 4.8: Direct shear test results for sample set taken next to the landslide at location km 27.

4.3. Discussion

During the field visit, the complexity of the study area was recognized. Observed features like waterfalls (Figure D.1a), pools (Figure D.1b), small reservoirs (Figure D.2), densely vegetated slopes (Figure D.3a), and large boulders in the streams ((Figure D.3b) and D.4a), but also other parts of the valley D.4b) make the setup of a fully distributed model for the area a challenging task. Including the observed features in detail is thereby not feasible. The observed heterogeneity of the study area however shows that a generalization of the study area is not feasible and that spatial information is required to explain hydrological processes.

The conducted field test to determine soil texture classes made it possible to determine the soil type with a large spatial distribution. The sample locations, however, were limited by the road and trail network within the study area. They nonetheless help to estimate the distribution of the soil type. Factors like lithology, topography, and hydrological processes are important drivers for the soil-forming geomorphology (Blume et al., 2016). However, no clear relationship between the observed soil types and factors like lithology and topography could be found.

Another study in the study area investigated whether vegetation cover could be used as a proxy to spatially determine the soil type and soil depth (Murata et al., 2009 and Murata et al., 2012). In the study area, evergreen forests as well as forests dominated by deciduous trees can be found, even though the climate of the region implies that evergreen forests should be the natural vegetation. Murata et al. (2012) found that under deciduous forests, the soil depth is significantly shallower. Furthermore, observed soil types under deciduous forests have a smaller water storage capacity compared to locations with evergreen forests. They therefore conclude that deciduous forests were formed in locations where the available soil water, due to soil depth and soil type, is too small to maintain evergreen forests during the dry period. These results match the observations in the field where *sandy loam* was exceptionally found in areas dominated by deciduous forests, and *silty loam* and *clay* were found in areas covered by evergreen forests. The hypothesis is therefore that the type of vegetation cover can be used to spatially distribute the soil type observations over the study area.

The results of the inverse auger hole test in the field were similar to the common values stated by (Blume et al., 2016) for the respective soil types. Furthermore, the inverse auger hole test is only intended to determine the magnitude of hydraulic conductivity rather than exact values (Hoorn, 1979). This suggests that literature values derived from observed soil types can be used instead of values measured in the field. Spatially distributed information about the soil type in the study area, therefore, also results in spatially distributed information on hydraulic conductivity.

The determined values for the shear parameters angle of internal friction and cohesion are not suitable for spatial determination of slope stability. Even though the values fall into the range of common values for the soil type (Dysli, 2000 and Minnesota Department of Transportation, 2007), they overestimate the actual shear strength of the soil in the field. Due to the heterogeneity of the soil, all samples contained grain sizes that exceeded the limits of the used specimen size during the laboratory analysis. This can lead to an overestimation of the shear strength of the soil when assuming a homogeneous sample (ASTM, 1994). Furthermore, the laboratory test was conducted under saturated and drained conditions. Under undrained conditions, which might occur in the field, the shear strength of the soil is reduced (Bishop, 1966). Additionally, the shear strength of sandy loam varies with changing state of saturation (El Hariri et al., 2023). The parameters angle of internal friction and cohesion are therefore subject to calibration when determining slope stability.

5

Physically-based multi-hazard model

Understanding hydrological processes like filling, storing, and draining of water in a slope to determine the antecedent conditions as well as understanding the processes during a trigger event is crucial to determine temporal landslide occurrence (Bogaard and Greco, 2016). Physically-based environmental models provide valuable insights into these hydrological subsurface processes, especially in catchments with limited observational data.

The LISEM software package, developed by the University of Twente, is a physically-based multi-hazard modeling software designed for the simulation of hydro-meteorological surface hazards. With this software, natural hazard events like flash floods and landslides can be modeled simultaneously. The potential of these models has been demonstrated in multiple case studies, such as Bout et al. (2022) and Bout et al. (2018), focusing on event-based simulation of flash floods and debris flows. LISEM therefore features a model setup for the simulation of multi-hazard events by providing the required input information to a pre-built interface. Furthermore, LISEM also supports the development of custom models with longer durations to assess hydrological processes, floods, and landslide hazards on a catchment scale. LISEM is open-source software, and as of version 0.2.4, it is still in the alpha phase. The software package, therefore, still contains various bugs.

5.1. Methodology

To assess the antecedent conditions and trigger mechanisms that led to the landslide event in September 2022, a fully distributed, physically-based model for catchment Ny6 in the Khao Yai National Park was developed using the LISEM software package. Due to various known bugs, the software was first tested on a synthetic, simplified catchment to understand the boundary conditions and assess the functionality of the different functions (Appendix F). Then, a modified hydrological model was developed to continuously model hydrological processes and monitor antecedent conditions related to landslides and slope stability. The developed model was then calibrated to the streamflow of catchment Ny6, and finally, the antecedent conditions and the trigger of the landslide event in September 2022 were simulated.

5.1.1. Model development

The developed model for the Khao Yai National Park follows the basic concepts of the pre-built event-based model of LISEM. However, conceptional modifications were necessary to allow continuous modeling of hydrological processes on catchment scale and calibration to streamflow (Figure 5.1). This includes large modifications like adding preferential lateral flow to the model as well as more detailed modifications to ensure a closed water balance which is crucial to continuously model soil moisture. For complex hydrological processes, like infiltration or flow processes, LISEM provides pre-developed functions. Other processes like precipitation, interception, or surface storage but also interactions between processes need to be developed manually. The physical laws to describe these processes are thereby identical to the pre-built event-based model (Bout et al., 2018).

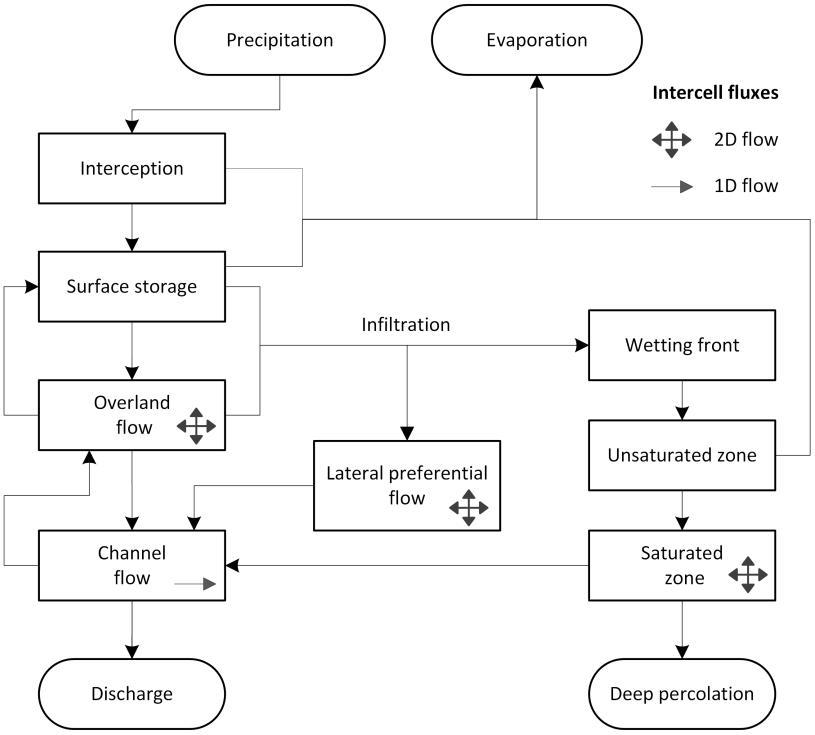

Figure 5.1: Conceptual physically-based hydrological model for the Khao Yai National Park.

The model is fully spatially distributed over a raster with a defined grid size of 30 m x 30 m. The different processes and the state of their respective storages are organized in layers (Figure 5.1). The internal time step in which flow processes are calculated is variable between 5 and 30 seconds, depending on the accuracy of the flow conditions required. The model output is generated for every simulated hour. At the beginning of each time step, water is added per grid cell as precipitation forcing to the model. This input is then distributed over the interception, surface storage, and overland flow layers, depending on the respective thresholds and storage stages. A part of the water is then evaporated from these layers, while another part is infiltrated into the subsurface. In the subsurface, the water is distributed into the wetting front, the unsaturated zone, the saturated zone, and the lateral preferential flow. Water is then moved between cells in the overland flow as well as in the flow layers in the subsurface. Finally, interactions between the flow layers and a defined channel are calculated, which then moves the water towards the outlet of the catchment to generate discharge.

Precipitation and Evapotranspiration

The precipitation forcing of the model can be provided either as a constant rainfall intensity or a spatially distributed rainfall intensity map. To account for the effect that the cell surface area increases with increasing slope angle, the rainfall input is corrected with the following equation:

$$dh = I_{\text{rain}} \times \frac{L_{\text{cell}}}{L_{\text{surface}}} = I_{\text{rain}} \times \cos(\theta) \tag{5.1}$$

where dh is the reduced water height to be added to the model, I_{rain} is the rainfall intensity, L_{cell} is the length of the grid cell, L_{surface} is the actual length of the surface in a grid cell, and θ is the slope angle.

Evapotranspiration is modeled either by using a constant potential evaporation value or measured potential evaporation. To obtain the actual evaporation the potential evaporation is multiplied by a calibrated crop factor. Furthermore, the evaporation is corrected for the slope similarly to the rainfall (Equation 5.1). Evaporated water heights are first subtracted from the interception storage. If the interception storage is empty, water is taken from the surface storage. Only if the surface storage is empty as well, water is taken from the unsaturated zone of the subsurface.

Interception and surface storage

In the developed model, interception is represented as a simple threshold process. The maximum interception storage of each grid cell is derived from the leaf area index (LAI) and the empirical relations found by Huene (1983) to link LAI and vegetation type to interception storage. Once the maximum interception storage is exceeded precipitation is directly added to the surface storage.

The surface storage is modeled with the concept of micro depression storage (S_{MD}) which can be derived from the standard deviation of surface heights (R_R) of a DEM and the slope angle θ. For various land cover types, R_R values are also available from literature (Kamphorst et al., 2000).

$$S_{\text{MD}} = 0.243, R_R + 0.010 R_R^2 + 0.012 R_R \cdot \cos(\theta) \tag{5.2}$$

From S_{MD} the runoff height h_{runoff} can be determined from the average water height on the surface h using a storage threshold at which runoff starts ($S_{\text{SD}} = 0.1 \cdot S_{\text{MD}}$):

$$h_{\text{runoff}} = \max\left(0.0, (h - S_{\text{SD}}) \cdot \left(1 - e^{-h \frac{h - S_{\text{SD}}}{S_{\text{MD}} - S_{\text{SD}}}}\right)\right) \tag{5.3}$$

Infiltration

For the infiltration of water into the subsurface, the LISEM function based on the method by Green and Ampt (1911) was used. This method assumes that a wetting front of fully saturated soil moves downwards into completely dry soil layers parallel to the soil surface. The function of the LISEM model however extends the method by adding percolation from the wetting front into the saturated zone and further percolation from the unsaturated zone in the groundwater zone. To determine the soil water retention curve the Farrel and Larson model is used (Farrell and Larson, 1972).

Surface flow

Surface flow is modeled either as overland flow or as channel flow. The custom model uses the standard flow functions of LISEM. Overland flow is modeled as dynamic flow using the Saint-Venant equations. Water can flow from one cell to multiple other cells at the same time but is thereby limited to four directions (Figure 5.2). Channel flow is modeled as a kinematic wave which is routed one dimensional through a local drainage network (Bout et al., 2018). Once overland flow reaches a cell with an active channel definition the water is instantly added to the channel if it still has capacity. Contrary to that, if water in the channel exceeds its capacity it is instantly added to the overland flow as flood water.

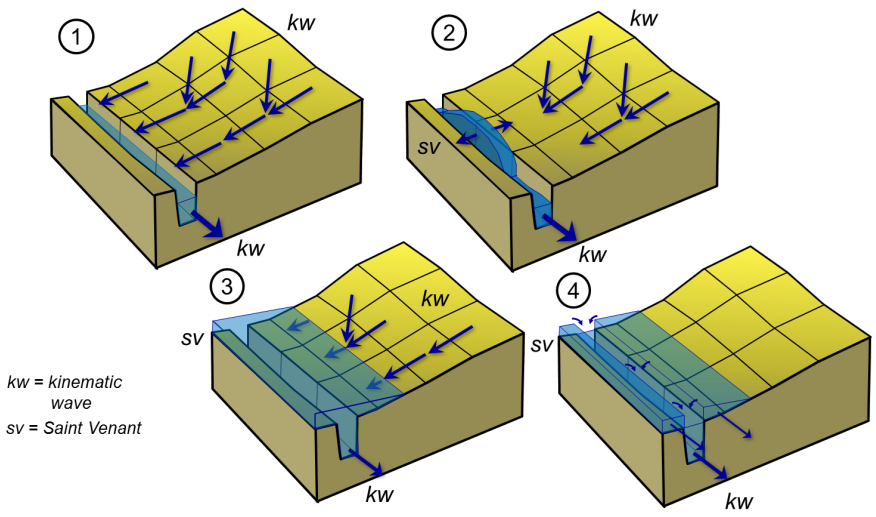

Figure 5.2: Overland flow processes and channel interactions in LISEM (Bout and Jetten, 2018).

Lateral preferential flow

Lateral preferential flow, or subsurface stormflow, is not implemented in the LISEM model because it is not a significant process in event-based multi-hazard modeling. However, for continuous streamflow modeling on a catchment scale, it is one of the core processes. Therefore, a calibration of the model to the observed streamflow without implementing preferential subsurface flow was not possible. However, flow paths of lateral preferential flow are complex and dependent on local conditions (Anderson et al., 2009). It was therefore implemented not fully physically based. Instead, the process is modeled using the overland flow function with added modifications to mimic preferential subsurface flow. The first modification is that the preferential flow layer is not fed by the surface storage but instead by the infiltration. Once a certain threshold in the height of the wetting front is exceeded, a part of the additionally infiltrated water is diverted into the preferential flow layer instead of the wetting front layer. Furthermore, the flow process is delayed with a time lag. This time lag only activates the flow process of the preferential subsurface flow layer at certain timesteps. The wetting front threshold, the diversion factor, and the time lag are therefore subject to calibration.

Groundwater flow

Groundwater flow is modeled with the transmissive flow equation of the LISEM model which is based on Darcy's law (Bout et al., 2018). If a channel is active in a cell, water is moved from the groundwater to the channel as base flow. The flux of the baseflow Q_{base} is determined from the hydraulic gradient $\frac{\partial h}{\partial x}$ caused by the head difference of the groundwater and the channel using Darcy's law:

$$Q_{\text{base}} = \frac{\partial h}{\partial x} \cdot k_{\text{sat}} \cdot (2.0 \cdot h_{\text{channel}} + w_{\text{channel}}) \cdot L_{\text{cell}}^2 \cdot dt \tag{5.4}$$

with the hydraudraulic conductivity k_{sat}, the water level in the channel h_{channel}, the width of the channel w_{channel}, the size of the grid cell L_{cell}, and the used time step dt. Additionally, deep percolation was added to the model, which allows for a constant sink of water from the groundwater layer. The constant for deep percolation, as well as dx, are calibration factors.

Slope stability

Due to a bug in the slope stability function of the LISEM, the slope stability function had to be redefined as a custom function. Similar to the the LISEM function, the custom function follows the infinite slope method which estimates the factor of safety (F_S) based on driving and resisting forces:

$$F_S = \frac{c' + \cos^2 \beta \cdot (H\gamma_s - H\gamma_w) \tan \phi'}{\gamma_s H \cos \beta \sin \beta} \tag{5.5}$$

Where:

c' : Effective cohesion (kPa)
β : Slope angle (degrees)
H : Depth of the soil layer (m)
γ_s : Unit weight of the soil (kN/m^3)
γ_w : Unit weight of water (kN/m^3)
ϕ' : Effective angle of internal friction (degrees)

Grid cells with a F_S < 1 are defined as unstable. The infinite slope method is thereby limited by the slope's length to soil depth ratio, which has to be greater than 10 (Milledge et al., 2012). The slope stability function of LISEM extends the infinite slope model to the iterative failure method (Bout et al., 2018). With this method, the possible failure of a neighboring cell, which would increase the slope angle, is considered iteratively during the calculation of F_S. This leads to the failure of groups of cells rather than single cells. Once the bug in LISEM is fixed, the iterative failure method function would therefore be preferable over the implemented custom function.

Model input and output

Next to the precipitation data, essentially only three datasets are required from which all physically-based model input parameters can be derived. These datasets are a DEM, a land use map, and a map containing information about the soil type. From the DEM, the catchment boundaries, the local drainage network (LDD), and therefore also the channel network can be derived. If single soil depth observations are available, a steady state soil depth map can also be derived from the DEM (Von Rütte and Or, 2013).

The land cover map can be used to determine Manning's friction values n and the standard deviation of surface heights R_R by linking land cover classes with empirical literature values (George, 1989 and Kamphorst et al., 2000). All other required parameters are derived automatically by the model if a soil type map is provided, which contains information about the portion of sand and clay in the soil. Furthermore, the model settings can be adjusted to either use initial conditions from a previous model run or apply field capacity as the standard value for the saturation state of the catchment.

The standard output of the model is the discharge and water level at the outlet of the catchment, which is generated after every simulated hour. Furthermore, the water balance is calculated and the water balance error is reported. Additionally, the states of the groundwater and soil moisture layers are saved. From these, the state of slope stability is calculated every simulated hour as well. Optionally, the setting can be changed to report and save the states of all layers. This however increases the required simulation time significantly.

5.1.2. Data preparation

The performance of a fully distributed, physically-based model is highly dependent on the quality of the input dataset. Due to the limited calibration factors, the potential to compensate for errors in the input data through calibration is restricted. Therefore, the preparation of the input dataset is one of the most important steps when developing a fully distributed, physically-based model. Obtained spatial datasets may require corrections before they are usable in the model. In the case of the Khao Yai National Park model, corrections were necessary for the precipitation observations, discharge observations, DEM, and soil type map to achieve the required data quality. Furthermore, the channel network and soil depth map had to be derived from the available datasets.

Precipitation

Radar rainfall observations were provided by Kasetsart University in two different forms. The first dataset contains hourly observations from a single radar station without corrections for the years 2018 to 2022. The second dataset is a composite, calculated from two radar stations for September 2022. Additionally, the data was already scaled by an hourly mean field bias correction factor, calculated from the rain gauges around the study area (Mapiam et al., 2023). However, the bias correction factors for single images range from 0.01 to 253, which exceeds the usual limits of 0.2 to 5.0. To use the radar images as input in the model, the radar observations were projected onto the model grid using the bilateral interpolation filter of LISEM.

To test the influence of the provided precipitation input and the bias correction factor, three additional input datasets were derived from the obtained radar observations and the available rain gauge information. For the first input dataset, the bias factor was capped at the usual limits of 0.2 and 5.0 to reduce outliers in the data. For the second dataset, bias correction factors exceeding 2.0 were redefined by calculating the moving average over three hours. Furthermore, images with a factor exceeding 5.0 were manually checked to analyze what caused the bias correction algorithm to fail. These checked images were then either completely removed or smoothed by calculating a moving average. In total, 9 out of 264 images were adjusted for the chosen simulation period. Additionally, a dataset was prepared that contained rain gauge measurements interpolated with inverse distance weighting (IDW) to be used as a baseline.

Discharge

At the water level gauge Ny6 the water level is measured continuously with a temporal resolution of 15 minutes. Through a rating curve, which is constructed annually, the water level measurements h

can be translated into discharge observations Q. When comparing the rating curves of different years significant differences are noticeable (Figure E.2). On the other hand, the stream cross-section at the measurement location, which is also measured annually, does not change significantly, especially not at higher bank levels (Figure E.3). Therefore, the differences in the given rating curves do not seem reasonable. A closer inspection of the constructed rating curves (Figure E.4 to E.7) showed that only two point measurements with a discharge higher than 30 m³/s were taken in recent years. As a result, the rating curves from 2019 to 2021 are strongly biased towards low flow conditions.

To obtain a generalized rating curve valid for multiple years the power law (Equation 5.6) was fitted on the point observation of the years 2020 to 2023 (Domeneghetti et al., 2012). For better comparison, the yearly rating curves were normalized by transforming the stage of zero discharge h_0 to zero for all rating curves.

$$Q = a(h - h_0)^b \tag{5.6}$$

The parameters a and b are thereby scaling factor and exponent of the power law respectively which are fitted to the observation data. Furthermore, the 95 % confidence interval was calculated for the generalized rating curve (Figure 5.3). It is notable that the generalized rating curve only differs slightly from the 2022 rating curve. However, the upper part of the rating curve is based on only one point measurement on the 29th of September 2022, which also explains the similarity between the generalized and 2022 rating curves.

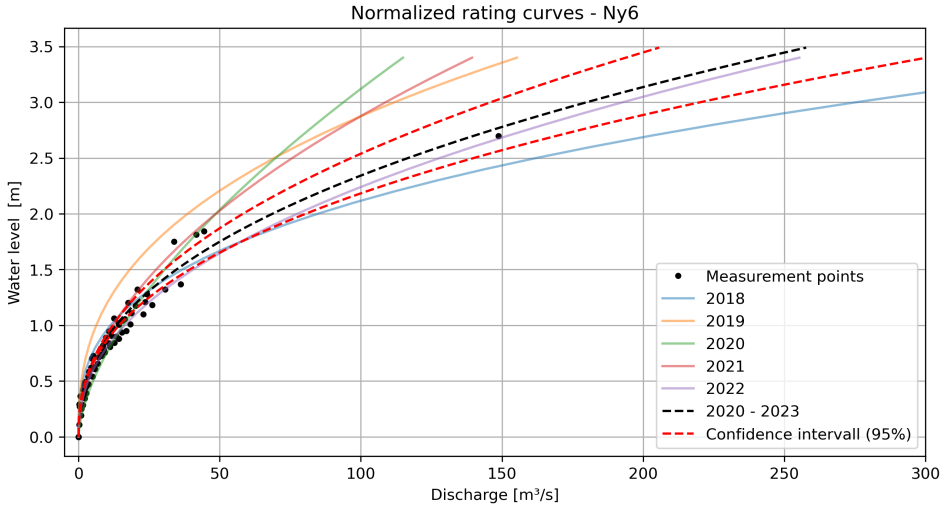

Figure 5.3: Normalized rating curves and generalized rating curve fitted to observations from 2020 to 2023.

DEM

The DEM serves as the base layer of the model, defining its spatial resolution. Two DEMs, PALSAR (12.5 m) and SRTM (30 m) were tested as input. The SRTM DEM was then selected for two reasons. Firstly, the PALSAR DEM contains more noise, leading to more pits in the model area. Secondly, using the 30 m DEM reduces simulation time by a factor of 10, which is crucial for modeling long periods. Pits in the DEM were filled using the pit-filling algorithm of LISEM, ensuring full connectivity in the drainage network according to the LDD. However, the overland flow function in LISEM does not strictly follow the LDD but allows flow to neighboring cells, excluding diagonal cells (Bout et al., 2018). Consequently, pits remain in the overland flow layer even after the pit-filling algorithm. To address this, an edge-preserving bilinear filter was applied to smoothen the DEM, significantly improving connectivity between grid cells for the overland flow function. Additionally, grid cells with a slope angle of zero cannot be interpreted correctly by LISEM. Therefore, random noise in the order of millimeters was added to flat areas to avoid numerical errors.

The boundary conditions of the different flow functions must be defined manually in LISEM. In this case, the boundary of the developed model is determined by the boundaries of the study catchment. Consequently, a closed boundary condition was selected, which must be defined within the DEM. The closed boundary is achieved by extending the DEM with one cell that has a value higher than the maximum value of the DEM. This ensures a closed water balance and a closed boundary at the edge of the catchment. The functionality of this method has been explored in depth on a synthetic catchment (Appendix F.1).

Channel

The channel network was derived from the LDD by the definition of a minimum upslope area of 0.5 km². The river width was determined with a custom logarithmic relationship based on field observations following the method of Frasson et al. (2019) on a local scale. The channel depth was limited by the soil depth to ensure stable base flow. Furthermore, the slope of the channel was derived from the slope angle of the DEM and smoothed with the bilateral filter to ensure stable flow conditions.

Due to continuous problems with pits in steep upslope areas caused by the directional flow limitations of the overland and groundwater flow functions, the channel network was extended into these upslope areas, where no channels exist in reality, to bypass the pits. In these extensions, the channel network was defined with a width similar to the cell size, and Manning's friction coefficient was applied similarly to overland flow instead of using the channel coefficient.

Soil type

Within the LISEM environment, hydrological parameters of the subsurface such as the hydraulic conductivity k_{sat}, the saturated soil moisture θ_S, or the soil water retention curve are derived from the texture class using empirical relations developed by Saxton and Rawls (2006). The texture class was taken from the soil map of the Land Development Department in Thailand. However, large areas within the study area are marked as unknown on the soil map (Figure 2.4). Therefore, the field observations were used to derive the texture class in the unknown area (Figure 5.4a), following the assumption that the present forest types are determined by the soil properties which has been shown by previous studies close to the study area (Murata et al., 2009 and Murata et al., 2012).

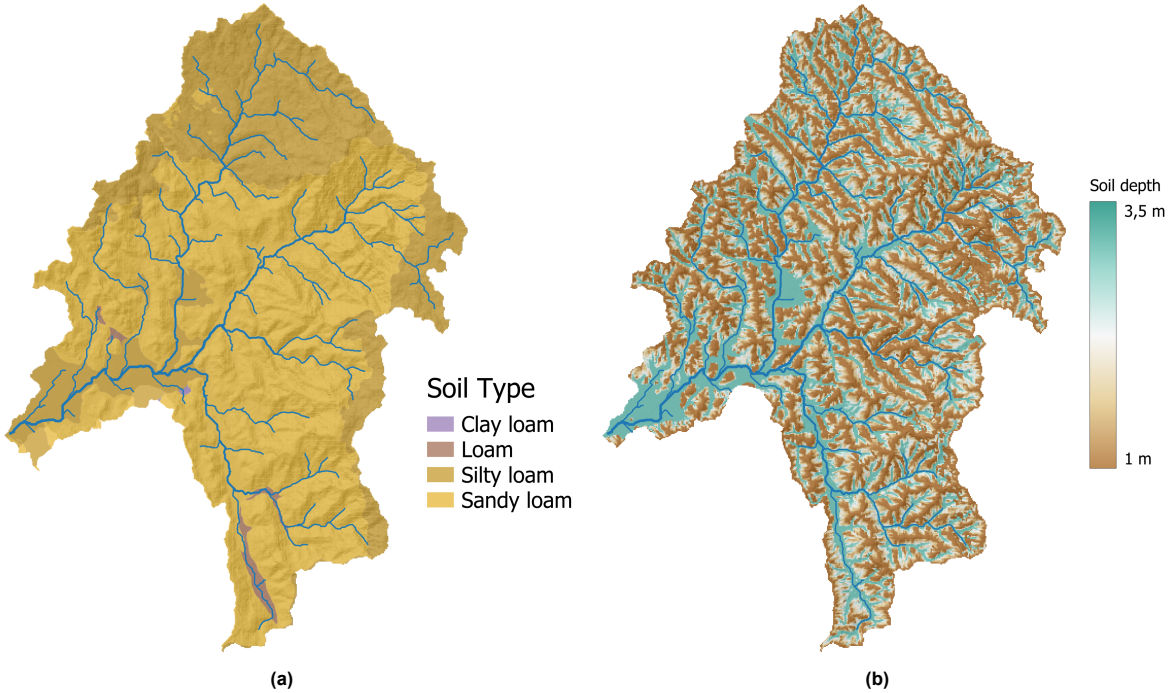

Figure 5.4: Soil type (a) and soil depth determined with steady state soil depth model (b).

The organic content of the soil was derived from a soil profile in the study area which is available in the SoilGrids database (Poggio et al., 2021). The relevant factor was thereby the distribution of organic content over the soil depth. Based on this soil profile, average values of 20 g/kg and 5 g/kg were calculated for the top layer and deeper layers of the soil.

Soil depth

The soil depth information given to the model determines the storage size of the subsurface and therefore influences the state of saturation of the subsurface. As no spatial information on soil depth is available, it has to be estimated based on the topography and single observations in the field. Soil depth was modeled using a steady-state soil model by Von Rütte and Or (2013) (Figure 5.4b). The model is based on a production and a transport parameter which determines the distribution of soil from the steep slopes into the valleys. To estimate appropriate production and transport parameters, the model was calibrated to the observations from the field by iterating the production and transport parameters to minimize the root mean square errors (RMSE) between modeled and observed soil depth in the field. In the calibration, a RMSE of 0.34 could be achieved. Unfortunately, due to the small number of field observations, a validation of the calibrated model was not possible.

The resulting soil depths within a single slope are too heterogeneous to allow for numerically stable flow conditions in the subsurface. Therefore, similar to the method used by Von Rütte and Or (2013), this model result was only used as a baseline. The modeled soil depth was further smoothed using a bilateral filter, which eliminates noise while preserving edges between different groups of values. Additionally, a minimum soil depth of 1 m was introduced to allow subsurface flow in every grid cell. Due to the complex geomorphology, it is not possible to represent the actual soil depth in every grid cell with a steady-state soil model. Instead, the goal is to create a soil depth input that accurately represents storage capacities and gradients in soil depth. Finally, the soil depth was reduced to the minimum value of 1 m on slopes with angles greater than 35° to create stable conditions in the initial state.

5.1.3. Model calibration and testing

Even though physically-based models usually require little calibration, possible uncertainties or a bias in the model input datasets may still make calibration necessary. Physical input parameters are thereby scaled with a constant factor. For most input datasets, like the precipitation forcing or the soil depth, this bias correction was already done in the data preparation phase. However, the conceptual modification of the model which introduced non-physically-based elements, made a calibration of introduced calibration parameters necessary.

The calibration was initially performed on a single event that occurred on the 19th and 20th of September 2022. A physically-based approach was adopted by calibrating individual processes to the different components of the observed hydrograph (Figure 5.5), following the theory of the three-component hydrograph separation model (Ogunkoya and Jenkins, 1993). After achieving satisfactory calibration results for the first event, the subsequent event on the 22nd of September was added to the calibration period to further generalize the calibration.

In the conceptual design of the model, soil moisture content is a key parameter. This parameter controls the infiltration rate and distributes the forced input across the different surface and subsurface layers. Consequently, the initial conditions of the model are of significant importance, as stable conditions can only be achieved if the soil moisture remains within reasonable margins. Additionally, since the state of the soil moisture governs the infiltration rate, the resulting streamflow is highly dependent on soil moisture. Therefore, calibration had to be conducted iteratively, with calibration parameters and initial conditions being determined simultaneously.

To achieve reasonable initial conditions, a model spinup was performed, which was split into two phases. In the first phase, only the groundwater model was initialized, with an initial groundwater height set to 50 % of the soil depth and a simulation time of one month. The results from this first spinup phase were then used as input for the second phase. In the second phase, the field capacity derived from the soil type (Saxton and Rawls, 2006) was used as the initial condition for soil moisture. This phase

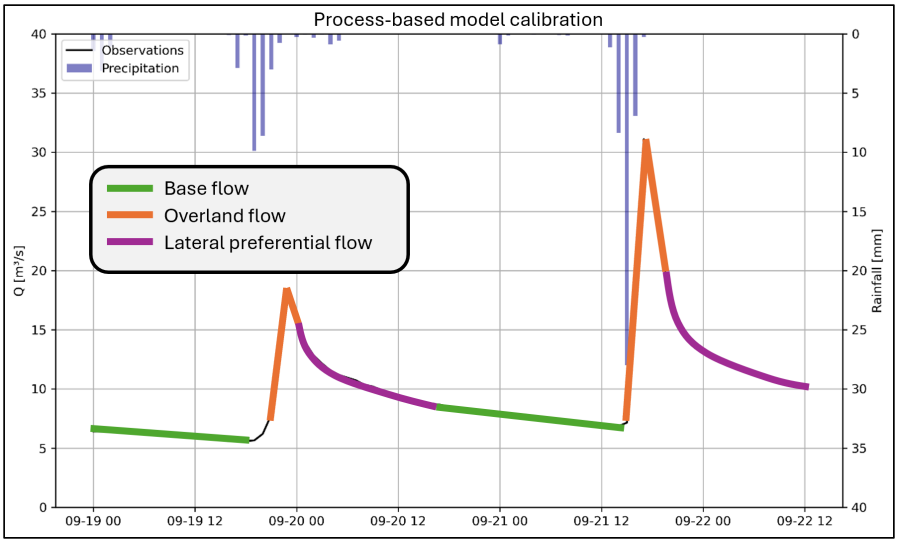

Figure 5.5: Different flow processes visible in the hydrograph of the calibration period.

was conducted with the full model, including forcing from rainfall radar observations, over a period of 17 days.

Once a satisfactory model result was achieved, the model was tested for a period of two weeks, from September 18th to September 30th. The performance of the model was evaluated by calculating the Nash-Sutcliffe Efficiency (NSE) for the simulated and observed streamflow:

$$\text{NSE} = 1 - \frac{\sum_{i=1}^{n} \left(Q_{\text{obs},i} - Q_{\text{sim},i}\right)^2}{\sum_{i=1}^{n} \left(Q_{\text{obs},i} - \overline{Q_{\text{obs}}}\right)^2} \tag{5.7}$$

with:

$Q_{\text{obs},i}$: Observed value at time step i
$Q_{\text{sim},i}$: Simulated value at time step i
$\overline{Q_{\text{obs}}}$: Mean of the observed values
n : Number of observations

5.1.4. Assessment of antecedent conditions and trigger event

The largest rainfall event of 2022, which triggered multiple landslides in the study area, occurred on September 29th, 2022. To assess the antecedent conditions of this event, hydrological processes were simulated for 10 days prior to the event. To evaluate the influence of different precipitation inputs, simulations were conducted using the original bias-corrected radar observations, radar observations with capped bias correction factors, and radar observations with smoothened bias correction factors. The results were then compared to those from a simulation using precipitation derived from rain gauge measurements with inverse distance weighting. This period was modeled with a timestep of 30 seconds.

Using the resulting antecedent conditions, the hazard event on September 29th, 2022, was simulated with three different forcing methods: the original bias-corrected radar observations, radar observations with capped bias correction factors, and precipitation derived from inverse distance weighting or rain gauge observations. Due to the high flow velocities during this extreme event, a timestep of 30 seconds was insufficient, as it limited the theoretical maximum flow velocity to 1 m/s in a DEM with a 30 m resolution (Bout and Jetten, 2018). Consequently, the event was modeled with a timestep of 5 seconds to achieve accurate flow approximations. To assess landslide trigger mechanisms during the event, slope stability was continuously calculated using the wetting front and groundwater layer to determine pore pressure in the soil. A grid cell is classified as unstable when the factor of safety falls below the threshold of one.

5.2. Results

A fully spatially distributed, physically-based model was developed for Khao Yai National Park. The developed model incorporates all relevant hydrological processes and is capable of continuously simulating streamflow and soil moisture of a catchment. The performance of the model was tested under different precipitation forcing. Furthermore, antecedent conditions were assessed for a landslide event in Khao Yai National Park in September 2022. Additionally, it was tested if the developed model is capable of simulating the flash flood and slope failure events that occurred in the study area on September 29th, 2022.

5.2.1. Streamflow

The calibrated model was tested with four different versions of precipitation forcing. The goal was thereby to prove that streamflow can be modeled continuously and to determine the required quality in precipitation forcing. Depending on the used version, precipitation inputs vary significantly (Figure 5.6). The IDW precipitation product functions as a baseline to determine the added value of using radar observations as model forcing. When comparing the observed rainfall from rain gauges with the radar observations, it is notable that in the first half of the tested period, the rain gauge observations were smaller than the radar observations, while in the second half, more rain was recorded in the rain gauges than measured by the radar. The difference in the versions of radar observations is due to the different handling of the bias correction factor. By capping the bias correction factor, single outliers in the radar observations can be removed. This correction is especially significant on extreme outliers like on September 22nd, where one defective image resulted in 20 mm extra precipitation. The smoothing of the bias correction factor mostly results in only small corrections by reducing the volatility.

The test of the model using the IDW precipitation input was not successful. While the timing of the discharge peaks is well represented in the model results, the magnitude is either far over- or underestimated (Figure 5.7). This matches the observation that the precipitation derived with IDW either over- or underestimates the radar observations (Figure 5.6). For this test, an NSE of less than zero was calculated, which suggests that the streamflow can be predicted better by the mean of the observations. Surprisingly, using the radar observation with original bias correction factors results in similar model performance. However, this has a different reason. The first two events of the test period can still be simulated well. The third peak, however, is overestimated by about 50 %. After this, no stable condition can be reached anymore due to the model's sensitivity to sudden changes in soil moisture.

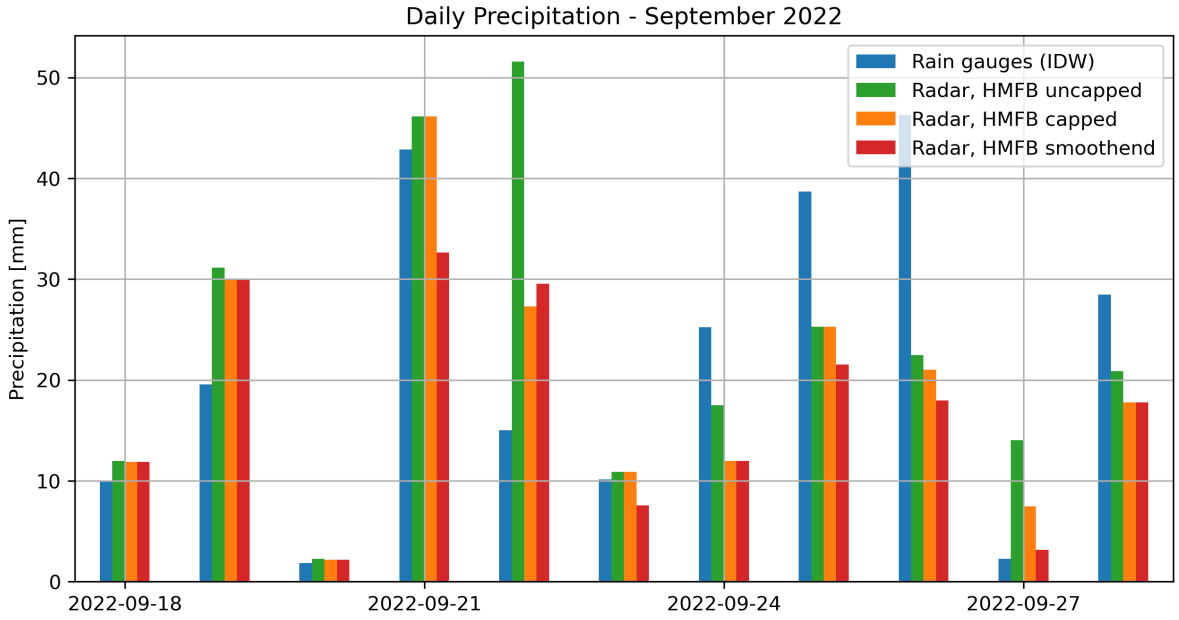

Figure 5.6: Mean daily precipitation in catchment Ny6 for different precipitation products.

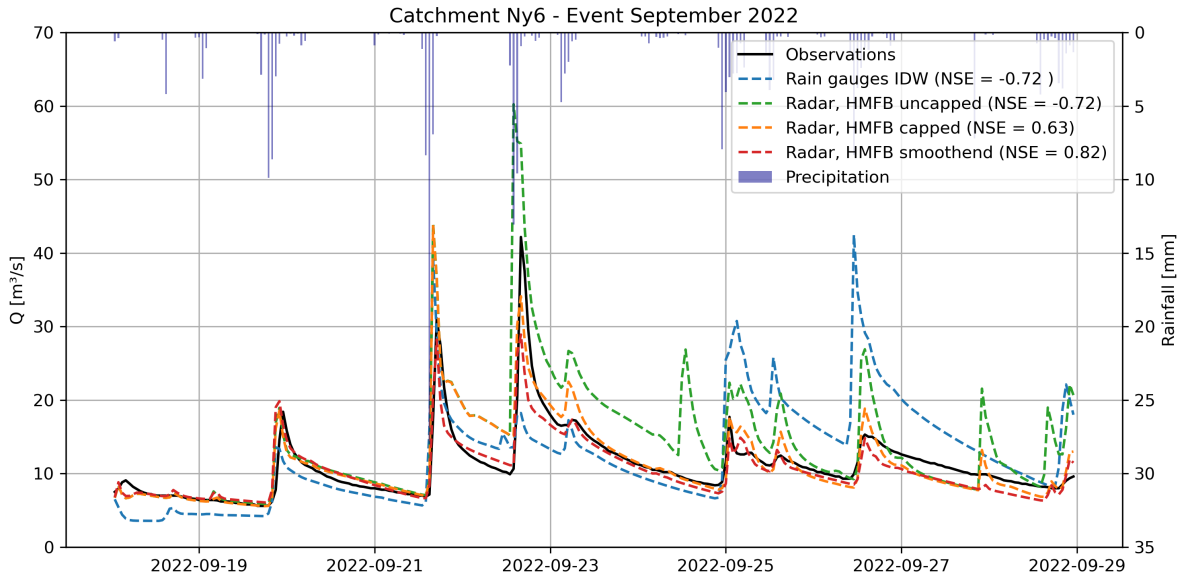

Figure 5.7: Modeled streamflow using different precipitation products.

When the outlier is removed by capping the bias correction factor, the model performance significantly increases. With that version, the timing and shape of all observed peaks are represented well. The calculated NSE resulted in a value of 0.63, which is considered a satisfactory model result (Moriasi et al., 2015). The model performance could be further improved by smoothing the bias correction factor of the radar observations. With that, a model fit resulting in an NSE of 0.82 could be achieved. This value indicates a good to very good performance (Moriasi et al., 2015). These results not only show the value of using radar observations as spatially distributed precipitation input but also prove that the developed model is capable of continuously simulating streamflow as long as the stability of the model is not disturbed by outliers in the forcing data.

Additionally, the discharge of the different flow types into the channel was tracked to determine the contribution of various flow paths to the streamflow (Figure 5.8). During the relatively short testing period of 10 days, the contribution of the base flow remained constant, independent of rain events. The flow type with the largest contribution was the preferential lateral flow. The contribution of overland flow was marginal and only appeared during streamflow peaks. However, in the interpretation of these results, it must be taken into account that the contribution of each flow type is tracked at the point of interaction with the channel. Therefore, overland flow that infiltrates before reaching the channel will be fully counted as subsurface flow.

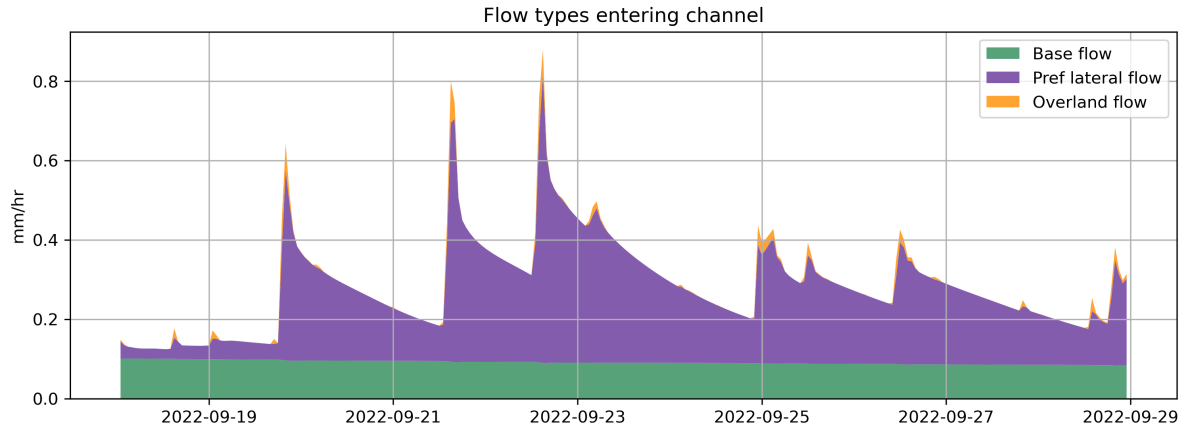

Figure 5.8: Flow rate of different flow types entering the channel.

5.2.2. Antecedent conditions

To assess the antecedent conditions for the landslide event on September 29th, 2022, the states of the subsurface water storages, namely, the wetting front, the unsaturated zone, and the saturated zone, were analyzed. The states of these subsurface layers were sampled at the locations where landslides were observed in 2022 to calculate the mean value for each respective parameter (Figure 5.9). Of the three factors analyzed, the wetting front is the most dynamic. During dry conditions, no wetting front is observed in the model results. A rain event then leads to a sharp increase in the height of the wetting front. However, after the rain event, the water in the wetting front fully percolates into the unsaturated zone. The storage in the unsaturated zone is determined by the soil moisture. The initial conditions of the testing period result from the model spin-up. While the soil moisture at the beginning of the testing period was moderate, with a value of 0.25, it steadily increased to 0.33, which represents 80 % saturation in the dominant soil type. The intervals between the different rain events were not sufficient for significant drainage into the saturated zone. However, an increase of 0.08 m was also simulated in the saturated zone during the period leading up to the landslide event.

When comparing these results with the IDW model version, it can be observed that for the first week, the states of the subsurface storages develop similarly, independently from the applied precipitation input. The overestimation of the rain events on September 25th and 26th however cause the soil moisture to reach a saturation state which enables increased percolation into the saturated zone. Therefore, the antecedent conditions of the landslide event would be overestimated with a precipitation input derived from rain gauge measurements.

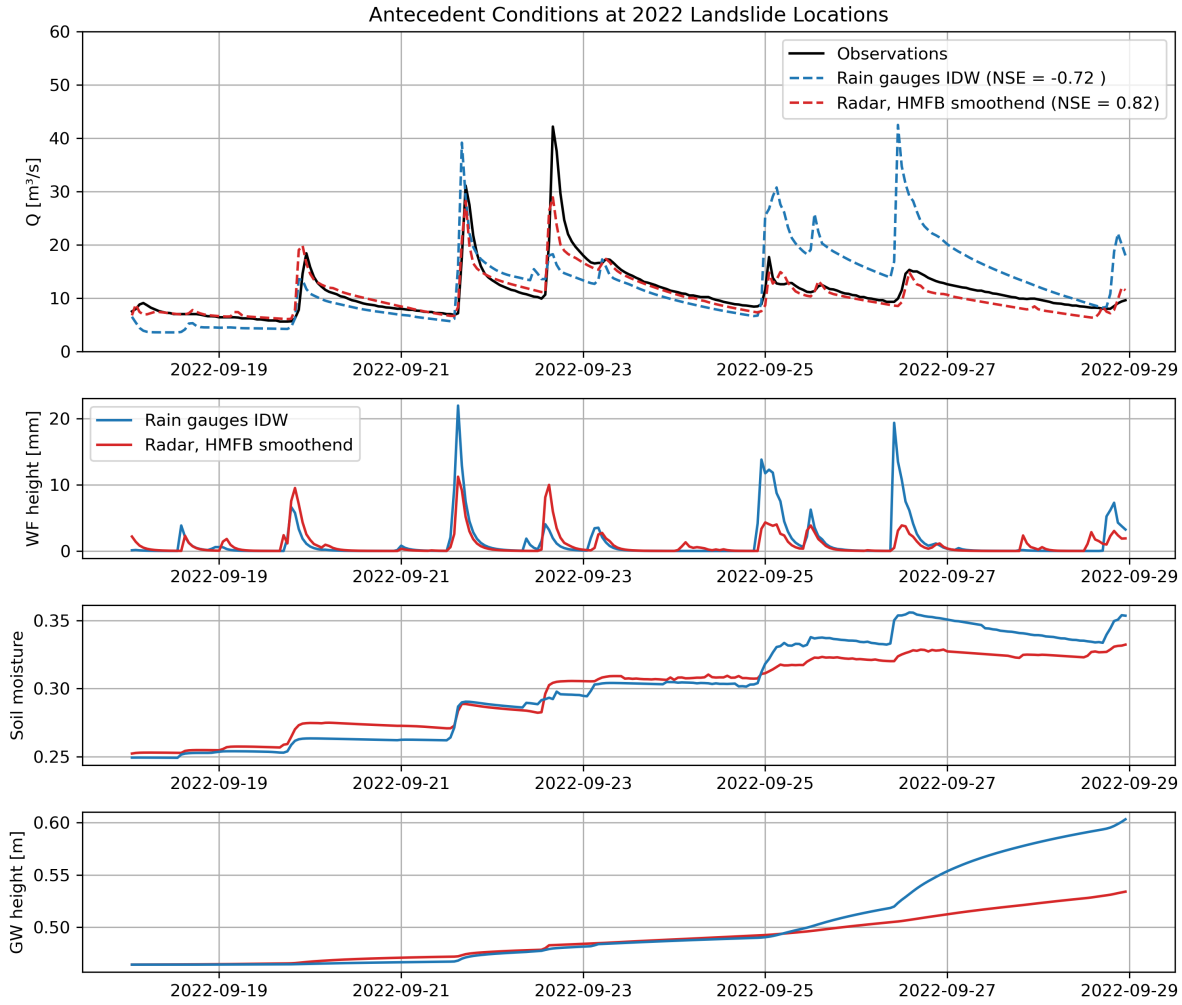

Figure 5.9: Mean value of antecedent conditions at 2022 landslide locations.

5.2.3. Landslide trigger event

Using the antecedent conditions determined from the preceding 10-day period, the landslide trigger event of September 29th, 2022 was simulated (Figure 5.10). Two versions of precipitation inputs were tested, the input derived by IDW from rain gauge observations and the original radar composite with uncapped bias correction. Further corrected versions of the radar composite were not used, as the uncapped version could already not provide sufficient precipitation to fit the observed streamflow. For both versions, the antecedent conditions determined with the smoothened radar observations were used as this version showed the best model performance.

Both tested versions of precipitation input are not fully able to accurately reflect the real rainfall patterns of the storm event. When using the precipitation input derived by Inverse Distance Weighting (IDW), the observed flood peak's height is reached, but the timing of the peak is shifted by three hours. Considering a catchment response time of about two hours, this shift is significant. The peak shift can be attributed to differences in observations at the rain gauges used for interpolation of spatial precipitation during the event (Figure G.2). The majority of the precipitation was measured at station STN1590, which is located at the catchment outlet. By deriving the spatial rainfall distribution using inverse distance weighting, the actual rainfall patterns are not accurately represented, leading to a concentration of precipitation input near the catchment outlet. This results in an accelerated catchment response due to the shorter spatial flow distances.

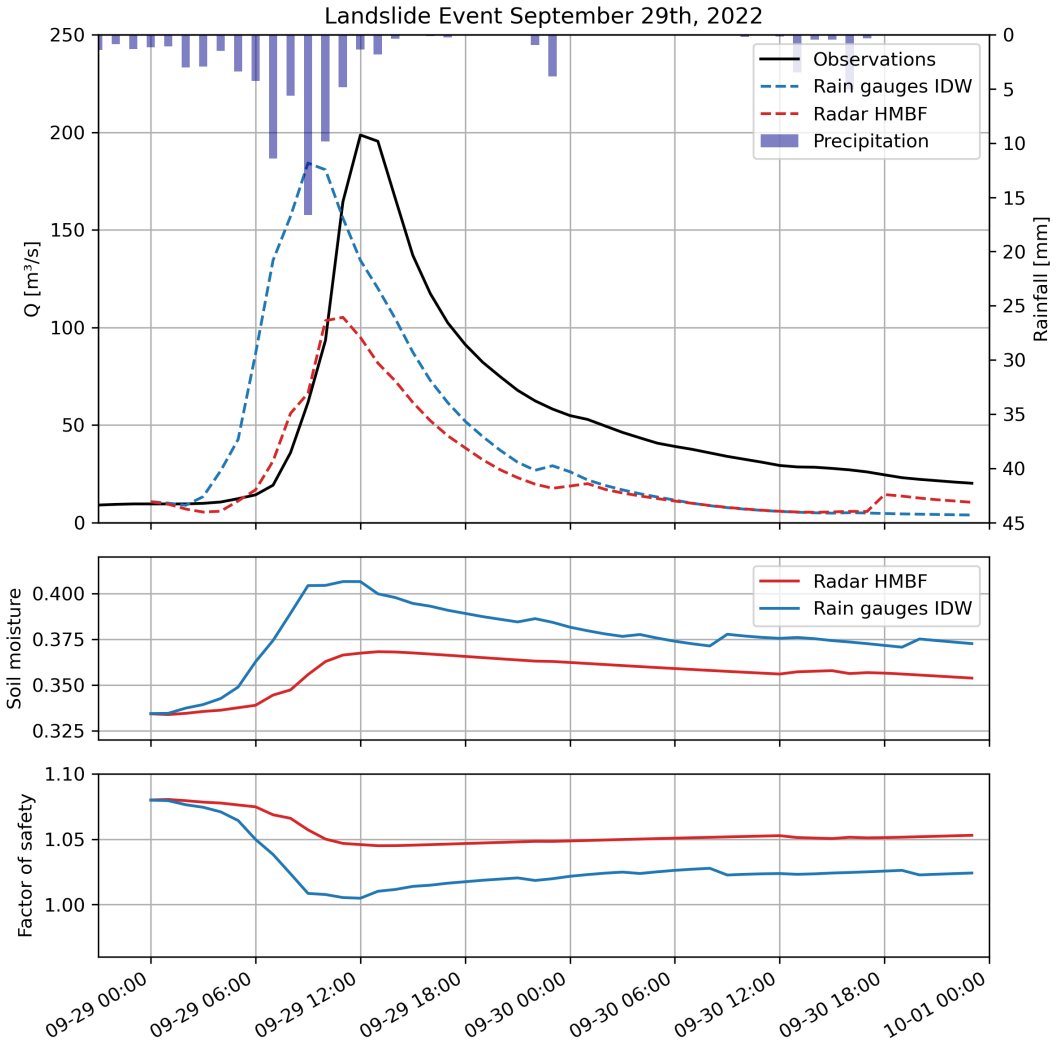

Figure 5.10: Modeled streamflow, soil moisture, and factor of safety for the landslide event on September 29th, 2022.

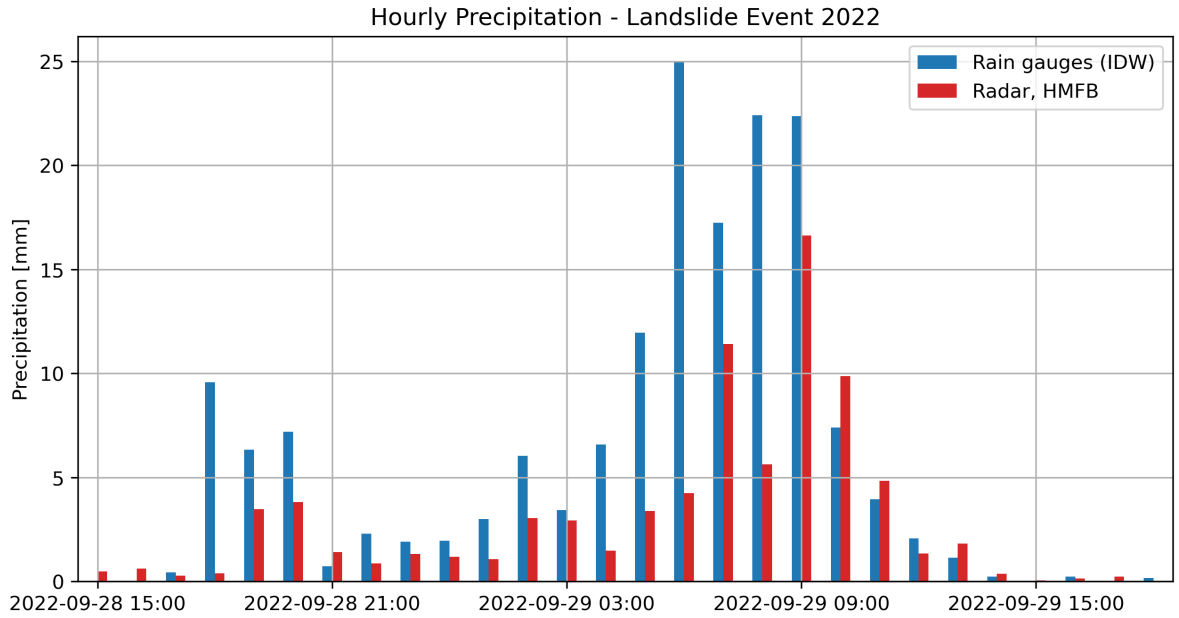

Figure 5.11: Difference in precipitation observed by rain gauges and radar during the 2022 landslide event.

When radar observations are used as precipitation input, the correct timing of the flood peak can be simulated. The discharge however is underestimated by 50 %. The comparison of the rain gauge and the radar observation reveals, that the radar observation largely underestimated the precipitation for the storm event (Figure 5.11). Only from 9:00 am onwards the radar observations did match the rain gauge measurements. Usually, these differences are corrected with the bias correction factor. However, the possible corrections are limited by the recorded spatial distribution of precipitation. During the storm event on September 29th, only limited precipitation could be recorded by the radar for the hours 6:00 am to 8:00 am (Figure G.1). At the same time, a precipitation of 100 mm was measured by the rain gauges STN1590 (Figure E.1). The majority of the storm event was therefore missed by the weather radar.

Even though the rainfall patterns during the storm event were not fully captured, a response in soil moisture at the landslide locations is still observable. When applying precipitation forcing derived from rain gauge observations, soil moisture suddenly increases from 0.33 to 0.41, representing fully saturated conditions. However, this results in only a 10 % relative change in the factor of safety. This indicates that topography is the primary driver of landslides at the investigated location, with hydrology being a secondary driver due to the generally unstable slope conditions. When using radar observations as input, the increase in soil moisture is smaller, reaching a saturation level of 90 %, which corresponds to a 5 % relative change in slope stability. This result, however, was expected given the missing radar observations.

With increasing slope angle, the influence of hydrological processes in the subsurface on slope stability decreases (Figure H.1). This, however, does not diminish the importance of these processes, as pore pressure build-up in the soil still triggers landslides. Instead, it increases the complexity in spatially determining slope stability, as changes in the factor of safety due to infiltration are small. After the simulated storm event, a factor of safety smaller than 1.10 was calculated for most steep slope areas in the catchment. However, an overestimation of unstable slopes is common, as unconditionally unstable slopes are also included. For three of the four recorded landslides, the slope stability decreased from an F_S > 1.10 to an F_S of 1.0. An impact of the trigger event was therefore still observable, even though its spatial distribution was not fully captured.

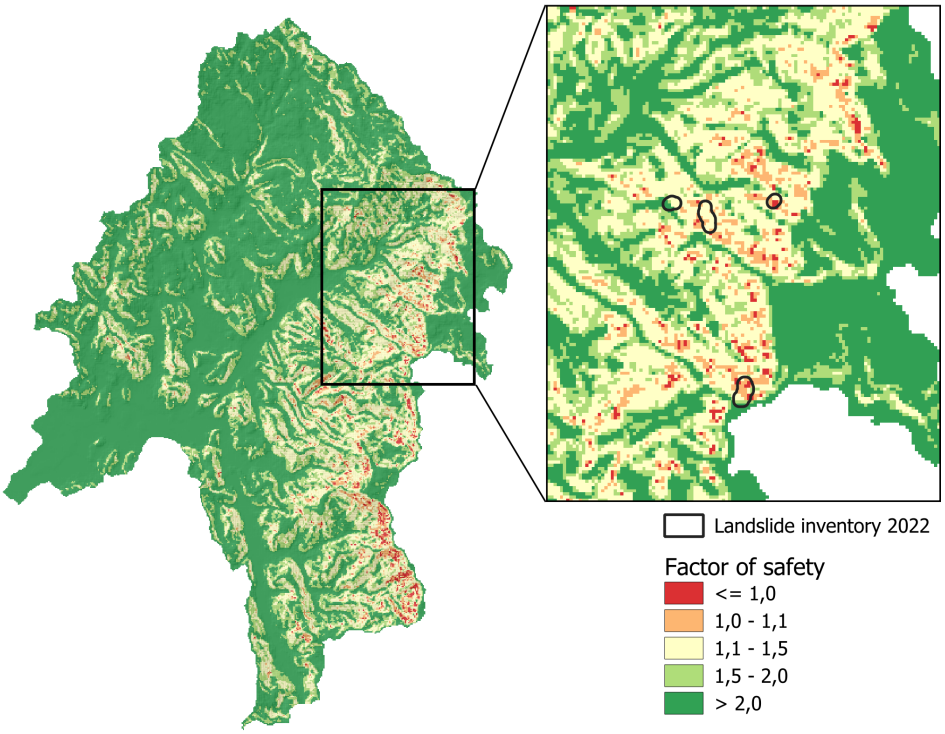

Figure 5.12: Factor of safety after storm event on September 29th, 2022.

5.3. Discussion

The developed fully spatially distributed physically-based model of the Khao Yai National Park was successfully tested for a period of two weeks, during which good model performance was achieved using radar observations as precipitation input. The introduction of preferential lateral flow to the model was crucial in representing the hydrologic behavior of the catchment, as it proved to be the dominant flow path in the peak generation of streamflow. Therefore, the developed model showed significantly increased performance in streamflow modeling compared to other previously developed catchment models within the LISEM environment (Vargas et al., 2021 and Rahmati et al., 2013).

The continuously good fit of the model to the observed streamflow also suggests that soil moisture can be modeled continuously. Due to the structure of the model, the state of the soil moisture controls the distribution of the precipitation input into the different flow paths. The assumption is therefore that as long as the resulting streamflow fits the observation, the modeled soil moisture must be correct too. The contrary could be observed when the model was faced with an outlier in the input data, which resulted in a sudden change in the state of soil moisture. Even though the model was given normal precipitation input afterward, a fit to the streamflow could not be achieved as the state of the soil moisture did not match the real soil moisture conditions anymore. Being able to continuously simulate fully spatial distributed soil moisture is thereby an important step towards the prediction of flash floods and landslides (Grillakis et al., 2016 and Javelle et al., 2010).

These findings are, however, limited by the relatively short testing period of two weeks. To prove the model's capability to continuously maintain its good performance, the simulated period needs to be extended. A longer simulation time would also increase the probability of outliers in the input data, which cannot be filtered by the presented smoothing method. Therefore, continuously checking and, if necessary, correcting the state of the modeled soil moisture would be advantageous. For this, either satellite-based methods (Brocca et al., 2012) or field measurements could be used. This would significantly increase the robustness of the model. This approach would also minimize the need for manual corrections to the radar observations.

The requirement of spatially distributed precipitation forcing with good quality for physically-based models has been shown in the result. For that, weather radar observations are currently considered the best option in regions with complex topography and limited ground measurements (Sokol et al., 2021). The capability of weather radar to provide information with the required quality has also been shown in the testing phase of the model. However, in mountainous regions in a tropical climate rainfall observations are still a challenging task. This can lead to the situation that single extreme events are missed, as was the case for the analyzed hazard event of September 29th. It therefore has to be accepted in the design of a multi-hazard early warning system that a potential trigger event might be missed.

Therefore, antecedent conditions play an even more important role in the temporal prediction of landslide occurrence. This significance was also evident in the analyzed events. During the tested period, the density of rainfall events was significantly higher compared to the preceding weeks. With continuous new input, soil water could not drain, leading to a consistent build-up of soil moisture toward the landslide event. The contribution of antecedent conditions to soil water was equivalent to 50 % of the water required for fully saturated soil conditions. Although the actual contribution of antecedent rainfall cannot be determined due to missing observations during the trigger event, it can be concluded that the density of smaller rain events before the hazard event increased the probability of slope failure. The importance of antecedent soil moisture conditions varies per event (Mostbauer et al., 2018). To draw generalized conclusions about the contribution of antecedent conditions, a larger variety of events should be analyzed.

However, even if the trigger event can be captured in its full magnitude and spatial extent, determining specific landslides remains challenging. In the study area, the majority of landslides occur on slopes steeper than 35°. The stability of these slopes is generally low, meaning the relative changes in slope stability caused by hydrological factors are small. Additional limitations arise from the large uncertainty in soil depth and slope stability parameters. The heterogeneity of the subsurface cannot be spatially represented with the current methods available. As a result, slope stability is underestimated in some areas and overestimated in others. Therefore, the developed model should be used to determine temporal landslide occurrence by analyzing regional slope stability rather than assessing the stability of exact locations (Aristizábal et al., 2016).

6 Conclusion

The aim of this research was to determine potentials and limitations of using weather radar information to model antecedent conditions and nowcast trigger events of landslides with a physically-based multi-hazard model in the Khao Yai National Park in Thailand. To achieve this, first the spatial landslide occurrence in the study area was analyzed to then assess temporal landslide occurrence with the developed fully distributed physically-based model. By testing the model with precipitation forcing of different quality, the potentials and limitations of using weather radar information could be determined.

As a first sub-goal, the landslide inventory for Khao Yai National Park had to be extended to increase the significance of the analysis results. The developed automatic landslide detection algorithm, based on remotely sensed relative changes in NDVI, is a relatively quick and robust method for detecting new landslides and creating a landslide inventory for a defined area. This approach works especially well in areas with little to no human activity, where land use changes do not influence the analysis. However, due to the limited optical resolution of available satellites, small landslides are often not detected by the applied method. A total of 142 landslides were detected from 2017 to 2023 to extend the landslide inventory.

From the extended landslide inventory, spatial landslide occurrence was analyzed by linking the landslide observations to predisposing factors using the frequency ratio method. Landslide susceptibility in Khao Yai National Park can be described by the predisposing factors of *Slope angle*, *Aspect*, *Land use*, *Lithology*, and *Distance to road*. The expanded landslide inventory was large enough to create a robust classification for landslide susceptibility. Although the frequency ratio method is relatively simple, it has demonstrated good performance in deriving the susceptibility map for the study area, where land use changes are minimal.

The third sub-goal was the development of a fully distributed physically-based multi-hazard model for the Khao Yai National Park. The developed model is based on the LISEM environment and includes the three relevant flow processes *overland flow*, *preferential lateral flow*, and *saturated subsurface flow*. A good model performance could be achieved in the testing phase of the model, resulting in an NSE of 0.82 when using radar information with a smoothened bias correction factor as precipitation forcing. Due to the model's sensitivity to sudden soil moisture changes, good representations of soil water contents can be assumed while the model contains a good performance in predicting streamflow.

With the developed model, antecedent conditions and trigger mechanisms of a landslide event in September 2022 were assessed. Due to the density of smaller precipitation events within 10 days prior to the hazard event, a continuous build-up in soil moisture could be observed. The antecedent precipitation thereby contributed to at least 50 % of the added pore water causing the slope failure event. The mechanisms of the trigger event could not be analyzed in detail due to missing observations in the weather radar observations. Furthermore, the determination of temporal occurrence of a specific landslide is limited by the uncertainty in soil depth. Instead, the regional probability of slope

failure should be determined through sudden changes in the relative slope stability.

To achieve good model performance, the developed model requires high-quality spatially distributed forcing. This level of quality could not be attained by spatially interpolating rain gauge measurements using the inverse distance weighting method. However, when weather radar observations were used as forcing, good performance was achieved in modeling streamflow and antecedent conditions. Due to the volatility of the hourly mean field bias correction factor, a moving average filter had to be applied to smooth the precipitation input. This method, however, cannot be applied when nowcasting precipitation with the weather radar. Therefore, better performance is expected when using weather radar information for modeling antecedent conditions than for nowcasting trigger events.

7

Recommendations

To further improve the presented work and address open questions, the following actions are recommended:

- The applied methodology for creating the landslide inventory and deriving the susceptibility map resulted in an excellent classification. However, before scaling up the method to a larger region, it is important to test whether this excellent performance is dependent on the specific characteristics of the study area. Particular emphasis should be placed on evaluating the potential influence of land use changes on the methodology.

- Even though the developed physically-based model yields good results, the conclusions drawn cannot be generalized due to the limited testing period. The model should therefore be calibrated and tested over a longer period, including multiple landslide events. This requires a time series spanning several years. Due to the extensive computation time required, the model should be set up on a machine with high computational power (e.g., DelftBlue). Additionally, an automated calibration method is necessary, as manual calibration over a long time series is not feasible. Implementing such a method would also enhance the model's transferability to other catchments.

- Furthermore, it is recommended to set up the model for another catchment to test its performance under different conditions. To avoid missing precipitation observations, a catchment with available radar observations with a high quality index should be selected. Catchment M43A is suggested as an additional study area because all required input information is already available. Additionally, soil moisture observations from stations managed by Kasetsart University could be used to calibrate the model not only against observed streamflow but also against observed soil moisture. This would also provide an opportunity to test further advancements of the model by implementing continuous correction of the modeled soil moisture using field observations.

- The model itself could also be improved further. Currently, preferential lateral flow is not modeled with a physically-based approach. Instead, a calibrated time lag is used to match the observed catchment response. Therefore, it is recommended to explore options for implementing preferential lateral flow based on physical parameters. This would also eliminate the need for extensive calibration.

- Additionally, further options should be explored to reduce the volatility of the hourly mean field bias correction factor in the radar observations. The application of a moving average filter has already resulted in significantly better model performance. However, future efforts should focus on improving the accuracy of rainfall predictions rather than solely enhancing the performance of the hydrological model.

References

Achu, A. L., C. D. Aju, M. Di Napoli, P. Prakash, G. Gopinath, et al. (2023). “Machine-learning based landslide susceptibility modelling with emphasis on uncertainty analysis”. In: *Geoscience Frontiers* 14.6, p. 101657. DOI: 10.1016/j.gsf.2023.101657.

Amatya, P., D. Kirschbaum, and T. Stanley (2022). “Rainfall-induced landslide inventories for Lower Mekong based on Planet imagery and a semi-automatic mapping method”. en. In: *Geoscience Data Journal* 9.2, pp. 315–327. DOI: 10.1002/gdj3.145.

Amatya, P., D. Kirschbaum, T. Stanley, and H. Tanyas (2021). “Landslide mapping using object-based image analysis and open source tools”. en. In: *Engineering Geology* 282, p. 106000. DOI: 10.1016/j.enggeo.2021.106000.

Anderson, A. E., M. Weiler, Y. Alila, and R. O. Hudson (2009). “Subsurface flow velocities in a hillslope with lateral preferential flow”. en. In: *Water Resources Research* 45.11. DOI: 10.1029/2008WR007121.

Aristizábal, E., J. I. Vélez, H. E. Martínez, and M. Jaboyedoff (2016). “SHIA_Landslide: a distributed conceptual and physically based model to forecast the temporal and spatial occurrence of shallow landslides triggered by rainfall in tropical and mountainous basins”. en. In: *Landslides* 13.3, pp. 497–517. DOI: 10.1007/s10346-015-0580-7.

ASF DAAC (2014). *PALSAR_Radiometric_Terrain_Corrected_high_res*. DOI: 10.5067/Z97HFCNKR6VA.

ASTM, D. 3.-9. (1994). “3080, Standard test method for direct shear test of soils under consolidated drained conditions”. In: *Annual book of ASTM standards* 4, pp. 290–295.

Bishop, A. W. (1966). “The Strength of Soils as Engineering Materials”. en. In: *Géotechnique* 16.2, pp. 91–130. DOI: 10.1680/geot.1966.16.2.91.

Blume, H.-P., G. W. Brümmer, H. Fleige, R. Horn, E. Kandeler, et al. (2016). *Scheffer/SchachtschabelSoil Science*. en. Berlin, Heidelberg: Springer Berlin Heidelberg. ISBN: 978-3-642-30941-0 978-3-642-30942-7. DOI: 10.1007/978-3-642-30942-7.

Bogaard, T. and R. Greco (2016). “Landslide hydrology: from hydrology to pore pressure”. en. In: *WIREs Water* 3.3, pp. 439–459. DOI: 10.1002/wat2.1126.

– (2018). “Invited perspectives: Hydrological perspectives on precipitation intensity-duration thresholds for landslide initiation: proposing hydro-meteorological thresholds”. en. In: *Natural Hazards and Earth System Sciences* 18.1, pp. 31–39. DOI: 10.5194/nhess-18-31-2018.

Bout, B. and V. G. Jetten (2018). “The validity of flow approximations when simulating catchment-integrated flash floods”. In: *Journal of Hydrology* 556, pp. 674–688. DOI: 10.1016/j.jhydrol.2017.11.033.

Bout, B., L. Lombardo, C. J. van Westen, and V. G. Jetten (2018). “Integration of two-phase solid fluid equations in a catchment model for flashfloods, debris flows and shallow slope failures”. In: *Environmental Modelling & Software* 105, pp. 1–16. DOI: 10.1016/j.envsoft.2018.03.017.

Bout, B. van den, C. Tang, C. van Westen, and V. Jetten (2022). “Physically based modeling of coseismic landslide, debris flow, and flood cascade”. English. In: *Natural Hazards and Earth System Sciences* 22.10, pp. 3183–3209. DOI: 10.5194/nhess-22-3183-2022.

Braaten, J. (2024). *Sentinel-2 Cloud Masking with s2cloudless*. https://developers.google.com/earth-engine/tutorials/community/sentinel-2-s2cloudless.

Brocca, L., F. Ponziani, T. Moramarco, F. Melone, N. Berni, et al. (2012). “Improving Landslide Forecasting Using ASCAT-Derived Soil Moisture Data: A Case Study of the Torgiovannetto Landslide in Central Italy”. en. In: *Remote Sensing* 4.5, pp. 1232–1244. DOI: 10.3390/rs4051232.

Chacón, J., C. Irigaray, T. Fernández, and R. El Hamdouni (2006). “Engineering geology maps: landslides and geographical information systems”. en. In: *Bulletin of Engineering Geology and the Environment* 65.4, pp. 341–411. DOI: 10.1007/s10064-006-0064-z.

Chaikaew, N., C. Kumsap, C. Wutthisakkaroon, and S. Pimmasarn (2023). “Landslide Susceptibility Mapping Using LiDAR Data: A Case Study of Khao Yai National Park, Thailand”. en. In: *International Journal of Geoinformatics* 19.3, pp. 1–12. DOI: 10.52939/ijg.v19i3.2597.

Cremonini, R. and D. Tiranti (2018). “The Weather Radar Observations Applied to Shallow Landslides Prediction: A Case Study From North-Western Italy”. In: *Frontiers in Earth Science* 6. URL: https://www.frontiersin.org/articles/10.3389/feart.2018.00134 (visited on 01/08/2024).

Department of Mineral Resources (2015). *Geological map of Thailand 1: 250000*. Bangkok.

Domeneghetti, A., A. Castellarin, and A. Brath (2012). “Assessing rating-curve uncertainty and its effects on hydraulic model calibration”. English. In: *Hydrology and Earth System Sciences* 16.4, pp. 1191–1202. DOI: 10.5194/hess-16-1191-2012.

Dysli, M. (2000). “Swiss Standard SN 670 010b, Characteristic coefficients of soils”. In: *Strasse und Verkehr* 86.2000, pp. 93–94.

Eckelmann, W., H. Sponagel, W. Grottenthaler, K.-J. Hartmann, R. Hartwich, et al. (2005). *Bodenkundliche Kartieranleitung. KA5*. de. URL: https://www.schweizerbart.de/publications/detail/isbn/9783510959204/Bodenkundliche_Kartieranleitung_5_Aufl (visited on 07/18/2024).

El Hariri, A., A. E. E. Ahmed, and P. Kiss (2023). “Sandy Loam Soil Shear Strength Parameters and Its Colour”. en. In: *Applied Sciences* 13.6, p. 3847. DOI: 10.3390/app13063847.

Farrell, D. A. and W. E. Larson (1972). “Modeling the pore structure of porous media”. en. In: *Water Resources Research* 8.3, pp. 699–706. DOI: 10.1029/WR008i003p00699.

Fayne, J. V., A. Ahamed, J. Roberts-Pierel, A. C. Rumsey, and D. Kirschbaum (2019). “Automated Satellite-Based Landslide Identification Product for Nepal”. EN. In: *Earth Interactions* 23.3, pp. 1–21. DOI: 10.1175/EI-D-17-0022.1.

Fowze, J. S. M., D. T. Bergado, S. Soralump, P. Voottipreux, and M. Dechasakulsom (2012). “Rain-triggered landslide hazards and mitigation measures in Thailand: From research to practice”. In: *Geotextiles and Geomembranes*. Special Issue: Mitigation of Geo-Disasters due to Climate Change 30, pp. 50–64. DOI: 10.1016/j.geotexmem.2011.01.007.

Frasson, R. P. d. M., T. M. Pavelsky, M. A. Fonstad, M. T. Durand, G. H. Allen, et al. (2019). “Global Relationships Between River Width, Slope, Catchment Area, Meander Wavelength, Sinuosity, and Discharge”. en. In: *Geophysical Research Letters* 46.6, pp. 3252–3262. DOI: 10.1029/2019GL082027.

Froude, M. J. and D. N. Petley (2018). “Global fatal landslide occurrence from 2004 to 2016”. English. In: *Natural Hazards and Earth System Sciences* 18.8, pp. 2161–2181. DOI: 10.5194/nhess-18-2161-2018.

George, J. (1989). *Guide for selecting Manning’s roughness coefficients for natural channels and flood plains*. en. Tech. rep. DOI: 10.3133/wsp2339.

Greco, R., P. Marino, and T. A. Bogaard (2023). “Recent advancements of landslide hydrology”. en. In: *WIREs Water* 10.6, e1675. DOI: 10.1002/wat2.1675.

Green, W. H. and G. Ampt (1911). “Studies on Soil Phyics.” In: *The Journal of Agricultural Science* 4.1, pp. 1–24.

Grillakis, M. G., A. G. Koutroulis, J. Komma, I. K. Tsanis, W. Wagner, et al. (2016). “Initial soil moisture effects on flash flood generation – A comparison between basins of contrasting hydro-climatic conditions”. In: *Journal of Hydrology*. Flash floods, hydro-geomorphic response and risk management 541, pp. 206–217. DOI: 10.1016/j.jhydrol.2016.03.007.

Hoorn, J. W. v. (1979). “Determining hydraulic conductivity with the inversed augerhole and infiltrometer methods”. English. In: *Proceedings of the International Drainage Workshop, May 1978, Wageningen, 150-154, ILRI publication 25, 1979*. URL: https://research.wur.nl/en/publications/determining-hydraulic-conductivity-with-the-inversed-augerhole-an (visited on 07/18/2024).

Huene, J. von (1983). *Die Interzeption des Niederschlags in landwirtschaftlichen Pflanzenbeständen*. URL: https://scholar.google.com/scholar_lookup?hl=en&volume=57&publication_year=1981&pages=1-53&journal=Arbeitsbericht+Deutscher+Verband+f%C3%BCr+Wasserwirtschaft+und+Kulturbau%2C+DVWK&author=J+Von+Hoyningen%E2%80%90Huene&title=Die+Interzeption+des+Niederschlags+in+Landwirtschaftlichen+Pflanzenbest%C3%A4nden (visited on 07/18/2024).

Javelle, P., C. Fouchier, P. Arnaud, and J. Lavabre (2010). “Flash flood warning at ungauged locations using radar rainfall and antecedent soil moisture estimations”. In: *Journal of Hydrology*. Flash Floods: Observations and Analysis of Hydrometeorological Controls 394.1, pp. 267–274. DOI: 10.1016/j.jhydrol.2010.03.032.

Kamphorst, E. C., V. Jetten, J. Guérif, J. Pitk a ¨ nen, B. V. Iversen, et al. (2000). “Predicting Depressional Storage from Soil Surface Roughness”. en. In: *Soil Science Society of America Journal* 64.5, pp. 1749–1758. DOI: 10.2136/sssaj2000.6451749x.

Kavzoglu, T., E. Kutlug Sahin, and I. Colkesen (2015). “Selecting optimal conditioning factors in shallow translational landslide susceptibility mapping using genetic algorithm”. In: *Engineering Geology* 192, pp. 101–112. DOI: 10.1016/j.enggeo.2015.04.004.

Khao Yai National Park (2021). “Khao Yai National Park | About KYNP”. In: URL: https://www.khaoyainationalpark.com/en/about (visited on 08/21/2024).

Kirschbaum, D., T. Stanley, and S. Yatheendradas (2016). “Modeling landslide susceptibility over large regions with fuzzy overlay”. en. In: *Landslides* 13.3, pp. 485–496. DOI: 10.1007/s10346-015-0577-2.

Kitamura, S., T. Yumoto, P. Poonswad, P. Chuailua, K. Plongmai, et al. (2002). “Interactions between Fleshy Fruits and Frugivores in a Tropical Seasonal Forest in Thailand”. In: *Oecologia* 133.4, pp. 559–572. URL: https://www.jstor.org/stable/4223456 (visited on 08/20/2024).

Land Development Department (2018). *Soil Series Map of Thailand 1:25,000*. Bangkok.

– (2020). *Land Use Map In North-Eastern Part of Thailand*. Bangkok.

Lee, S. and B. Pradhan (2007). “Landslide hazard mapping at Selangor, Malaysia using frequency ratio and logistic regression models”. en. In: *Landslides* 4.1, pp. 33–41. DOI: 10.1007/s10346-006-0047-y.

Li, L., H. Lan, C. Guo, Y. Zhang, Q. Li, et al. (2017). “A modified frequency ratio method for landslide susceptibility assessment”. en. In: *Landslides* 14.2, pp. 727–741. DOI: 10.1007/s10346-016-0771-x.

Lucchese, L. V., G. G. de Oliveira, and O. C. Pedrollo (2021). “Investigation of the influence of nonoccurrence sampling on landslide susceptibility assessment using Artificial Neural Networks”. In: *CATENA* 198, p. 105067. DOI: 10.1016/j.catena.2020.105067.

Mandrekar, J. N. (2010). “Receiver Operating Characteristic Curve in Diagnostic Test Assessment”. In: *Journal of Thoracic Oncology* 5.9, pp. 1315–1316. DOI: 10.1097/JTO.0b013e3181ec173d.

Mapiam, P. P., M. Methaprayun, A. Jotisankasa, and T. Bogaard (2023). *Investigating the quality of radar composites in a mountainous region in northeastern Thailand*. en. Tech. rep. EGU23-4828. Copernicus Meetings. DOI: 10.5194/egusphere-egu23-4828.

Methaprayun, M., A. Jotisankasa, R. Khunwisetkul, T. Bogaard, and P. Puttaraksa Mapiam (2023). “Low-cost sensor observations for flash flood and landslide early warning systems in the mountainous area”. In: EGU–4872. DOI: 10.5194/egusphere-egu23-4872.

Milledge, D., D. Griffiths, S. Lane, and J. Warburton (2012). “Limits on the validity of infinite length assumptions for modelling shallow landslides”. In: *Earth Surface Processes and Landforms* 37, n/a–n/a. DOI: 10.1002/esp.3235.

Minnesota Department of Transportation (2007). *Pavement Design*. Minnesota Department of Transportation. St. Paul, MN.

Moriasi, D. N., M. W. Gitau, N. Pai, and P. Daggupati (2015). “Hydrologic and water quality models: Performance measures and evaluation criteria”. In: *Transactions of the ASABE* 58.6, pp. 1763–1785.

Mostbauer, K., R. Kaitna, D. Prenner, and M. Hrachowitz (2018). “The temporally varying roles of rainfall, snowmelt and soil moisture for debris flow initiation in a snow-dominated system”. en. In: *Hydrology and Earth System Sciences* 22.6, pp. 3493–3513. DOI: 10.5194/hess-22-3493-2018.

Murata, N., S. Ohta, A. Ishida, M. Kanzaki, C. Wachirinrat, et al. (2009). “Comparison of soil depths between evergreen and deciduous forests as a determinant of their distribution, Northeast Thailand”. en. In: *Journal of Forest Research* 14.4, pp. 212–220. DOI: 10.1007/s10310-009-0127-7.

– (2012). “Soil depth and soil water regime in a catchment where tropical dry evergreen and deciduous forests coexist”. en. In: *Journal of Forest Research* 17.1, pp. 37–44. DOI: 10.1007/s10310-010-0248-z.

Ngandam Mfondoum, A. H., P. Wokwenmendam Nguet, J. V. Mefire Mfondoum, M. Tchindjang, S. Hakdaoui, et al. (2021). “Adapting sudden landslide identification product (SLIP) and detecting real-time increased precipitation (DRIP) algorithms to map rainfall-triggered landslides in Western Cameroon highlands (Central-Africa)”. In: *Geoenvironmental Disasters* 8.1, p. 17. DOI: 10.1186/s40677-021-00189-9.

Ogunkoya, O. O. and A. Jenkins (1993). “Analysis of storm hydrograph and flow pathways using a three-component hydrograph separation model”. In: *Journal of Hydrology* 142.1, pp. 71–88. DOI: 10.1016/0022-1694(93)90005-T.

OpenTopography (2013). “Shuttle Radar Topography Mission (SRTM) Global”. In: DOI: 10.5069/G9445JDF.

Perera, E. N. C., A. M. C. T. Gunaratne, and S. B. D. Samarasinghe (2022). “Participatory Landslide Inventory (PLI): An Online Tool for the Development of a Landslide Inventory”. en. In: *Complexity* 2022, e2659203. DOI: 10.1155/2022/2659203.

Phạm, T., D. Bui, I. Prakash, and M. Dholakia (2015). “Landslide Susceptibility Assessment at a Part of Uttarakhand Himalaya, India using GIS – based Statistical Approach of Frequency Ratio Method”. In: *International Journal of Engineering Research and* V4, pp. 338–344. DOI: 10.17577/IJERTV4IS110285.

Piciullo, L., M. Calvello, and J. M. Cepeda (2018). “Territorial early warning systems for rainfall-induced landslides”. en. In: *Earth-Science Reviews* 179, pp. 228–247. DOI: 10.1016/j.earscirev.2018.02.013.

Pimmasarn, S., N. Chaikaew, N. Tripati, and C. Wuthisakkarun (2022). “Landslide Susceptibility Assessment in Khao Yai National Park.” th. In: *Defence Technology Academic Journal* 4.10, pp. 81–89. URL: https://sc01.tci-thaijo.org/index.php/dtaj/article/view/240295 (visited on 01/06/2024).

Poggio, L., L. M. de Sousa, N. H. Batjes, G. B. M. Heuvelink, B. Kempen, et al. (2021). “SoilGrids 2.0: producing soil information for the globe with quantified spatial uncertainty”. English. In: *SOIL* 7.1, pp. 217–240. DOI: 10.5194/soil-7-217-2021.

Potthoff, E. C. (2022). “Spatially distributed modelling of hydro-meteorological hazards for a physical deterministic analysis of flash flood occurrence”. en. In.

Rahmati, M., R. Neyshabouri, A. fakheri fard, M. M. Oskouei, A. Ahmadi, et al. (2013). “Rainfall-runoff prediction using LISEM model in Lighvan watershed, North West of Iran”. In: *Technical Journal of Engineering and Applied Sciences* 3, pp. 1893–1901.

Regmi, A. D., K. Yoshida, H. R. Pourghasemi, M. R. DhitaL, and B. Pradhan (2014). “Landslide susceptibility mapping along Bhalubang — Shiwapur area of mid-Western Nepal using frequency ratio and conditional probability models”. en. In: *Journal of Mountain Science* 11.5, pp. 1266–1285. DOI: 10.1007/s11629-013-2847-6.

Ridd, M. F. and C. K. Morley (2011). “The Khao Yai Fault on the southern margin of the Khorat Plateau, and the pattern of faulting in Southeast Thailand”. In: *Proceedings of the Geologists’ Association*. Environmental Change in sub-Saharan Africa 122.1, pp. 143–156. DOI: 10.1016/j.pgeola.2010.08.008.

Royal Irrigation Department (2024). *Daily Mean Gage Height and Rating Curve*.

Rozalis, S., E. Morin, Y. Yair, and C. Price (2010). “Flash flood prediction using an uncalibrated hydrological model and radar rainfall data in a Mediterranean watershed under changing hydrological conditions”. In: *Journal of Hydrology*. Flash Floods: Observations and Analysis of Hydrometeorological Controls 394.1, pp. 245–255. DOI: 10.1016/j.jhydrol.2010.03.021.

Saxton, K. E. and W. J. Rawls (2006). “Soil Water Characteristic Estimates by Texture and Organic Matter for Hydrologic Solutions”. en. In: *Soil Science Society of America Journal* 70.5, pp. 1569–1578. DOI: 10.2136/sssaj2005.0117.

Scheip, C. M. and K. W. Wegmann (2021). “HazMapper: a global open-source natural hazard mapping application in Google Earth Engine”. English. In: *Natural Hazards and Earth System Sciences* 21.5, pp. 1495–1511. DOI: 10.5194/nhess-21-1495-2021.

Schmidt-Thomé, P., T. Tatong, P. Kunthasap, and S. Wathanaprida (2018). “Community based landslide risk mitigation in Thailand”. In: *Episodes* 41. DOI: 10.18814/epiiugs/2018/018017.

Silalahi, F. E. S., Pamela, Y. Arifianti, and F. Hidayat (2019). “Landslide susceptibility assessment using frequency ratio model in Bogor, West Java, Indonesia”. In: *Geoscience Letters* 6.1, p. 10. DOI: 10.1186/s40562-019-0140-4.

Sokol, Z., J. Szturc, J. Orellana-Alvear, J. Popová, A. Jurczyk, et al. (2021). “The Role of Weather Radar in Rainfall Estimation and Its Application in Meteorological and Hydrological Modelling—A Review”. en. In: *Remote Sensing* 13.3, p. 351. DOI: 10.3390/rs13030351.

Stanley, T. A., D. B. Kirschbaum, G. Benz, R. A. Emberson, P. M. Amatya, et al. (2021). “Data-Driven Landslide Nowcasting at the Global Scale”. In: *Frontiers in Earth Science* 9, p. 640043. DOI: 10.3389/feart.2021.640043.

Sun, X., J. Chen, Y. Bao, X. Han, J. Zhan, et al. (2018). “Landslide Susceptibility Mapping Using Logistic Regression Analysis along the Jinsha River and Its Tributaries Close to Derong and Deqin County, Southwestern China”. en. In: *ISPRS International Journal of Geo-Information* 7.11, p. 438. DOI: 10.3390/ijgi7110438.

Thai Meterological Department (2015). *CLIMATOLOGICAL DATA FOR THE PERIOD 1981-2010*. Tech. rep. Bangkok: Climate Center. URL: http://climate.tmd.go.th/content/file/75 (visited on 08/21/2024).

Toet, W., L. van der Plas, D. van Wijngaarden, N. Aberson, and J. van Lith (2023). "A study on applying OpenRiverCam software to determine river discharge levels and the design of a rain radar calibration model in Thailand". In.

UNISDR (2015). "Sendai Framework for Disaster Risk Reduction 2015 - 2030". en. In: *UN world conference on disaster risk reduction*. URL: http://www.wcdrr.org/uploads/Sendai_Framework_for_Disaster_Risk_Reduction_2015-2030.pdf.

Vakhshoori, V. and M. Zare (2016). "Landslide susceptibility mapping by comparing weight of evidence, fuzzy logic, and frequency ratio methods". In: *Geomatics, Natural Hazards and Risk* 7.5, pp. 1731–1752. DOI: 10.1080/19475705.2016.1144655.

Vargas, M. M., S. Beskow, C. R. de Mello, M. M. de Moura, M. C. M. Nunes, et al. (2021). "Capability of LISEM to estimate flood hydrographs in a watershed with predominance of long-duration rainfall events". en. In: *Natural Hazards* 109.1, pp. 593–614. DOI: 10.1007/s11069-021-04850-2.

Von Rütte, J. and D. Or (2013). "Rainfall-triggered shallow landslides at catchment scale: Threshold mechanics-based modeling for abruptness and localization". In: *Water Resources Research* 49. DOI: 10.1002/wrcr.20418.

Wang, Q., D. Wang, Y. Huang, Z. Wang, L. Zhang, et al. (2015). "Landslide Susceptibility Mapping Based on Selected Optimal Combination of Landslide Predisposing Factors in a Large Catchment". en. In: *Sustainability* 7.12, pp. 16653–16669. DOI: 10.3390/su71215839.

Yilmaz, I. (2009). "Landslide susceptibility mapping using frequency ratio, logistic regression, artificial neural networks and their comparison: A case study from Kat landslides (Tokat—Turkey)". In: *Computers & Geosciences* 35.6, pp. 1125–1138. DOI: 10.1016/j.cageo.2008.08.007.

A

Landslide Inventory

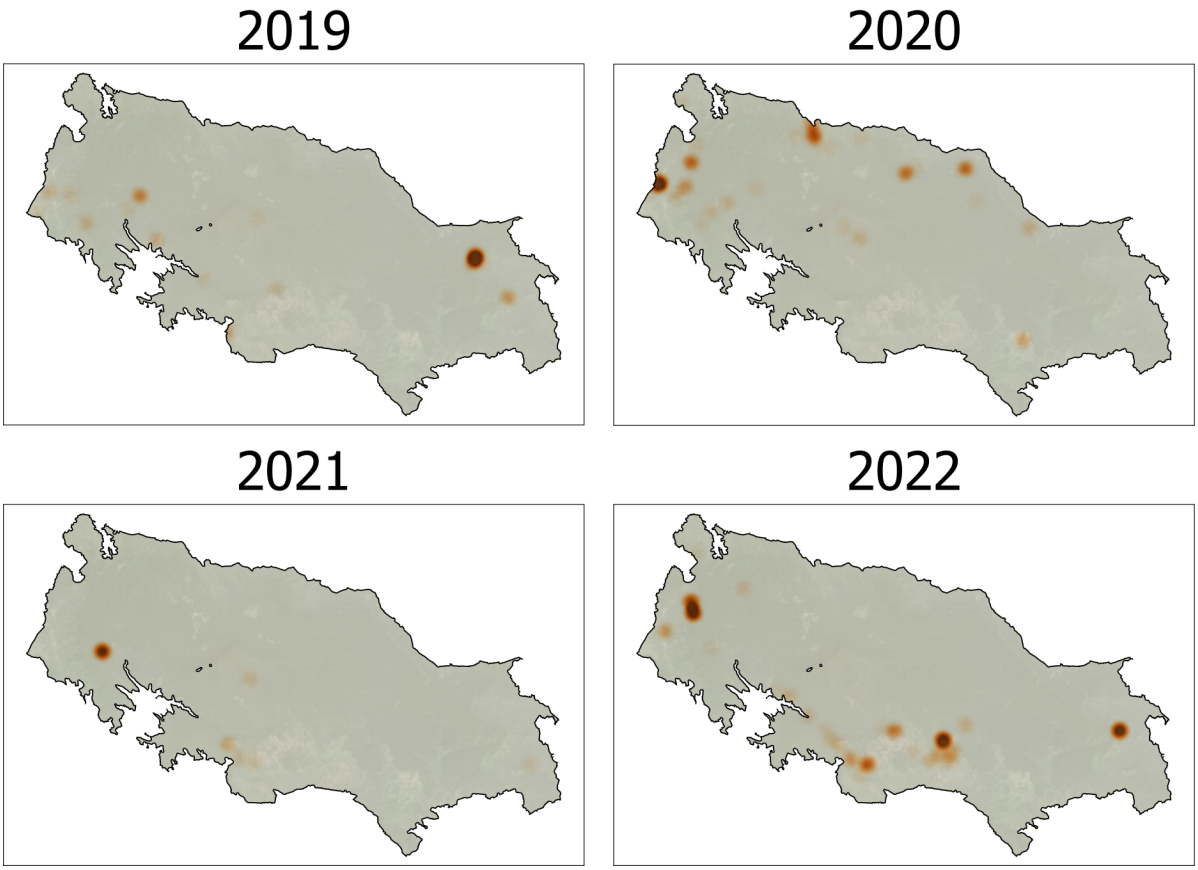

Figure A.1: Heat map of landslide events per year. Different hot spots can be identified for the years 2019 to 2022.

Table A.1: Landslide inventory, coordinates given in CRS: EPSG:32647.

Landslide ID	Easting [m]	Northing [m]	Year	Area [m²]
1_2017	807379.18	1584163.35	2017	1850
2_2017	806033.42	1573079.99	2017	2180
3_2017	807486.23	1584144.44	2017	1316
4_2017	809642.00	1583196.17	2017	2643
5_2017	807174.95	1584259.73	2017	6308
6_2017	753791.11	1575328.97	2017	663
7_2017	799041.28	1582736.49	2017	833
8_2017	757598.37	1581351.36	2017	977
9_2017	754430.70	1575776.84	2017	685
10_2017	807302.71	1573423.69	2017	2562
11_2017	794574.13	1579796.35	2017	924
1_2018	774984.51	1573273.52	2018	925
2_2018	807612.53	1584124.29	2018	678
1_2019	768397.53	1579003.01	2019	1223
2_2019	799251.28	1584232.91	2019	1800
3_2019	736210.00	1593775	2019	1069
4_2019	733045.28	1594216.09	2019	941
5_2019	738753.26	1589259.37	2019	1564
6_2019	733073.62	1593984.84	2019	670
7_2019	799050.15	1583425.25	2019	2151
8_2019	800606.74	1583411.71	2019	870
9_2019	747131.59	1593564.42	2019	3422
10_2019	745074.50	1591401.57	2019	1001
11_2019	798996.46	1583647.36	2019	944
12_2019	799519.37	1583646.24	2019	1484
13_2019	760723.12	1573092.14	2019	923
14_2019	804333.78	1577734.91	2019	2799
15_2019	731147.33	1590866.34	2019	1075
16_2019	760602.99	1571989.55	2019	1680
17_2019	798808.97	1582981.67	2019	2177
18_2019	749652.88	1586727.41	2019	935
19_2019	749704.26	1586700.52	2019	909
20_2019	799255.22	1584545.87	2019	1396
21_2019	799147.90	1584345.2	2019	762
22_2019	799210.49	1584345.43	2019	1774
23_2019	742738.29	1608864.56	2019	662
24_2019	799359.41	1583889.81	2019	848
25_2019	799399.92	1583776.78	2019	761
26_2019	765241.60	1589948.71	2019	762
27_2019	756898.42	1580618.95	2019	765
1_2020	738121.33	1598686.03	2020	815
2_2020	782267.53	1592743.5	2020	756
3_2020	739475.66	1589322.99	2020	670
4_2020	759405.12	1601048.51	2020	905
5_2020	748010.80	1594745.69	2020	847
6_2020	743471.45	1592352.47	2020	795
7_2020	757042.82	1602221.1	2020	961

Continued on next page

Table A.1 – Continued from previous page

Landslide ID	Easting [m]	Northing [m]	Year	Area [m²]
8_2020	741054.79	1591202.51	2020	1219
9_2020	736495.61	1608155.23	2020	847
10_2020	781030.06	1597860.66	2020	1262
11_2020	743678.32	1592306.91	2020	670
12_2020	780371.06	1597815.2	2020	2212
13_2020	771297.59	1597125.07	2020	3902
14_2020	735575.40	1593567.25	2020	1581
15_2020	737797.57	1598752.37	2020	1189
16_2020	731257.82	1594062.52	2020	833
17_2020	757135.10	1603502.38	2020	1823
18_2020	754479.28	1602968.39	2020	940
19_2020	757356.50	1602716.96	2020	670
20_2020	764349.96	1602579.92	2020	839
21_2020	737913.48	1598893.84	2020	678
22_2020	732899.64	1595171.61	2020	1364
23_2020	732773.36	1595102.64	2020	3303
24_2020	756803.13	1602999.73	2020	2622
25_2020	738152.61	1598709.05	2020	919
26_2020	780419.37	1597921.14	2020	914
27_2020	738690.70	1601476.5	2020	962
28_2020	772889.39	1598269.87	2020	925
29_2020	737114.29	1595182.23	2020	1675
30_2020	757753.92	1601585.36	2020	684
31_2020	789677.37	1571235.34	2020	685
32_2020	756592.83	1604929.62	2020	3067
33_2020	736741.25	1594943.34	2020	1147
34_2020	732284.75	1597107.15	2020	684
35_2020	761684.82	1588707.44	2020	847
36_2020	737525.29	1599145.58	2020	1002
37_2020	789492.04	1571120.48	2020	1872
38_2020	733220.10	1595719.04	2020	1082
39_2020	733101.13	1595657	2020	3440
40_2020	790540.34	1588697.23	2020	1667
41_2020	732966.74	1595893.4	2020	1413
42_2020	764217.58	1586962.04	2020	1582
1_2021	807722.31	1573697.85	2021	930
2_2021	740877.81	1591227.46	2021	834
3_2021	741339.91	1591217.59	2021	5101
4_2021	762626.84	1574709.69	2021	1259
5_2021	760713.09	1576754.32	2021	2072
6_2021	764305.34	1586898.6	2021	1359
7_2021	741299.08	1591133.68	2021	1927
8_2021	749232.77	1581745.37	2021	742
9_2021	764797.22	1573845.42	2021	1166
1_2022	762734.79	1574660.33	2022	931
2_2022	776920.80	1577494.89	2022	666
3_2022	760842.07	1576601.35	2022	670
4_2022	761133.98	1576309.88	2022	683

Continued on next page

Table A.1 – Continued from previous page

Landslide ID	Easting [m]	Northing [m]	Year	Area [m²]
5_2022	777044.05	1577341.01	2022	1768
6_2022	769803.96	1578953.59	2022	664
7_2022	778333.59	1574272.18	2022	1008
8_2022	767861.12	1579210.35	2022	810
9_2022	763869.82	1572939.36	2022	763
10_2022	762743.39	1574519.97	2022	866
11_2022	762724.21	1574327.3	2022	978
12_2022	756092.20	1581259.37	2022	1442
13_2022	752847.53	1584049.93	2022	739
14_2022	741084.37	1591653.08	2022	795
15_2022	759755.53	1577446.55	2022	1268
16_2022	804514.85	1578924.67	2022	7653
17_2022	804477.39	1578789.82	2022	838
18_2022	774995.63	1574289.09	2022	1193
19_2022	758799.90	1578919.06	2022	919
20_2022	775047.99	1574225.65	2022	666
21_2022	778033.69	1574207.45	2022	756
22_2022	778682.90	1575617.79	2022	2243
23_2022	751149.03	1585268.53	2022	654
24_2022	765568.88	1573426.55	2022	2190
25_2022	738570.77	1599056.04	2022	673
26_2022	776487.79	1575516.14	2022	2213
27_2022	737589.93	1599035.82	2022	1459
28_2022	753192.32	1584408.41	2022	970
29_2022	737930.43	1598904.26	2022	4343
30_2022	772611.47	1575889.98	2022	850
31_2022	733885.68	1594375.5	2022	2818
32_2022	780417.24	1579802.97	2022	973
33_2022	769203.87	1578678.18	2022	833
34_2022	738280.91	1597224.58	2022	8592
35_2022	780856.02	1579714.23	2022	761
36_2022	765285.89	1574095.7	2022	823
37_2022	777198.09	1574410.48	2022	731
38_2022	769715.19	1578924.73	2022	2302
39_2022	738397.42	1606466.71	2022	926
40_2022	764347.60	1571783.56	2022	763
41_2022	765206.12	1573705.54	2022	683
42_2022	777007.79	1577658.02	2022	755
43_2022	765036.71	1573954.46	2022	752
44_2022	777013.72	1577544.16	2022	3919
45_2022	765368.93	1573904.57	2022	838
46_2022	746113.06	1600954.65	2022	1281
47_2022	777528.05	1577268.79	2022	2224
1_2023	738699.51	1598928.91	2023	3065
2_2023	804576.55	1578941.12	2023	684
3_2023	760762.62	1576755.47	2023	1847

B

Predisposing factors

B.1. Input maps

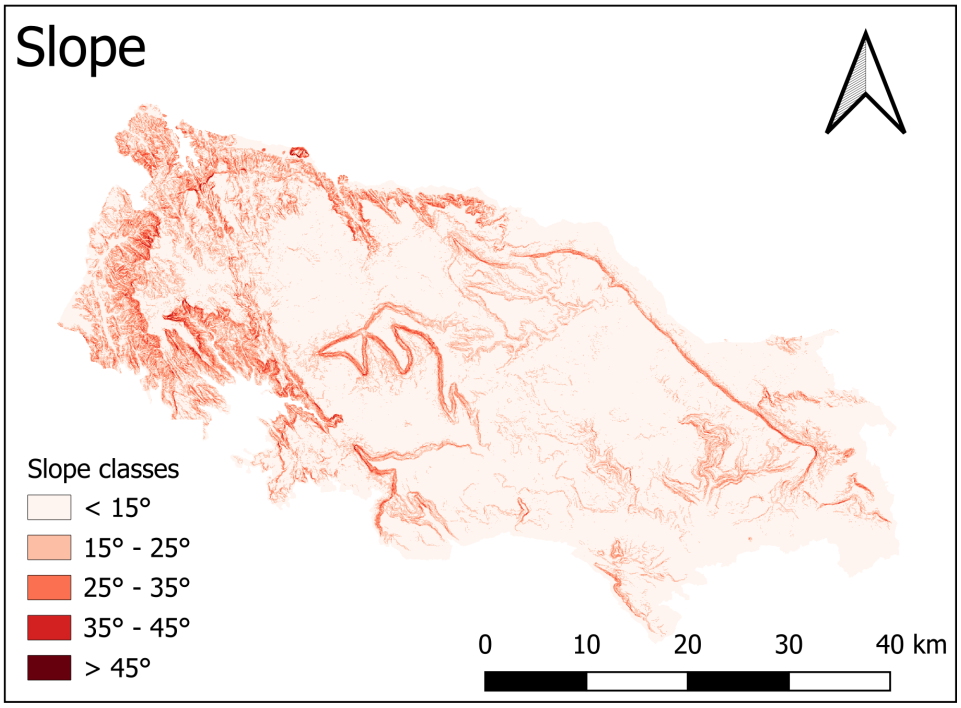

Figure B.1: Predisposing factor: Slope.

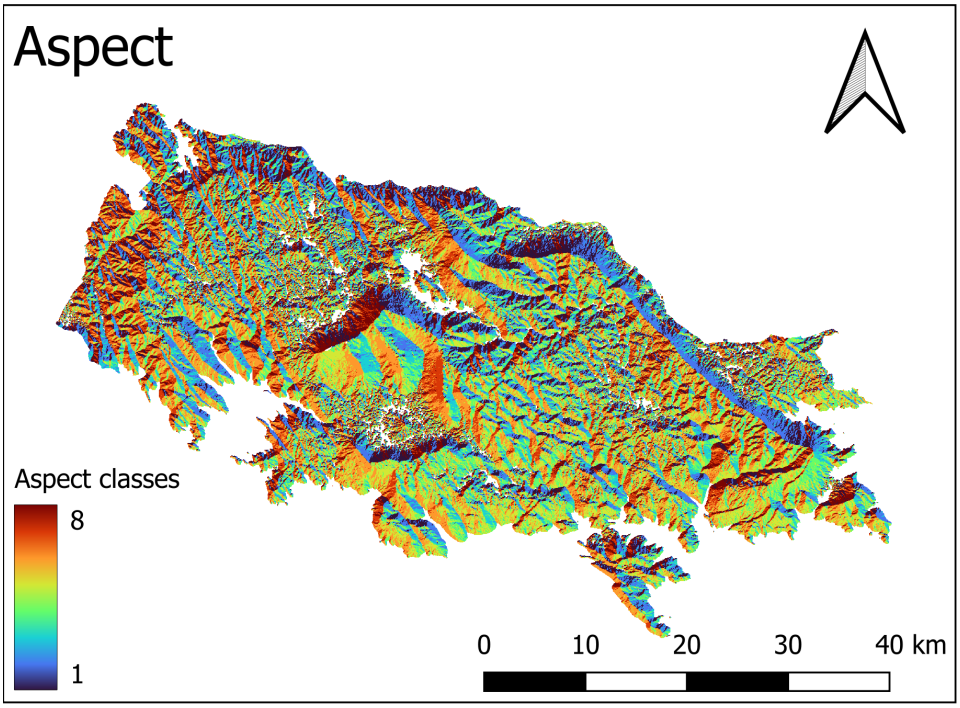

Figure B.2: Predisposing factor: Aspect.

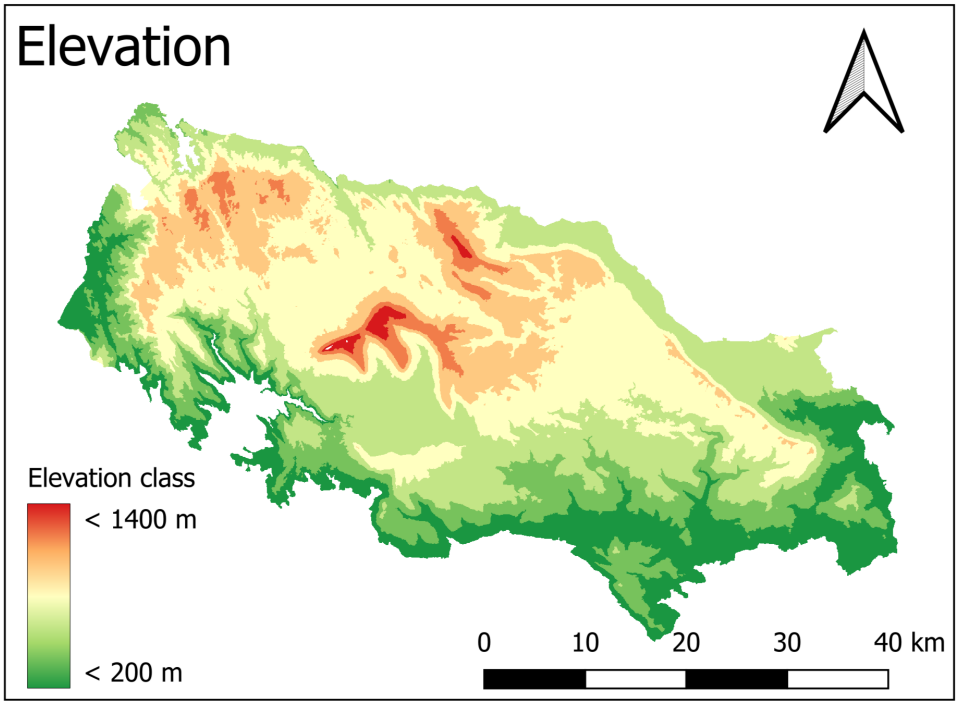

Figure B.3: Predisposing factor: Elevation.

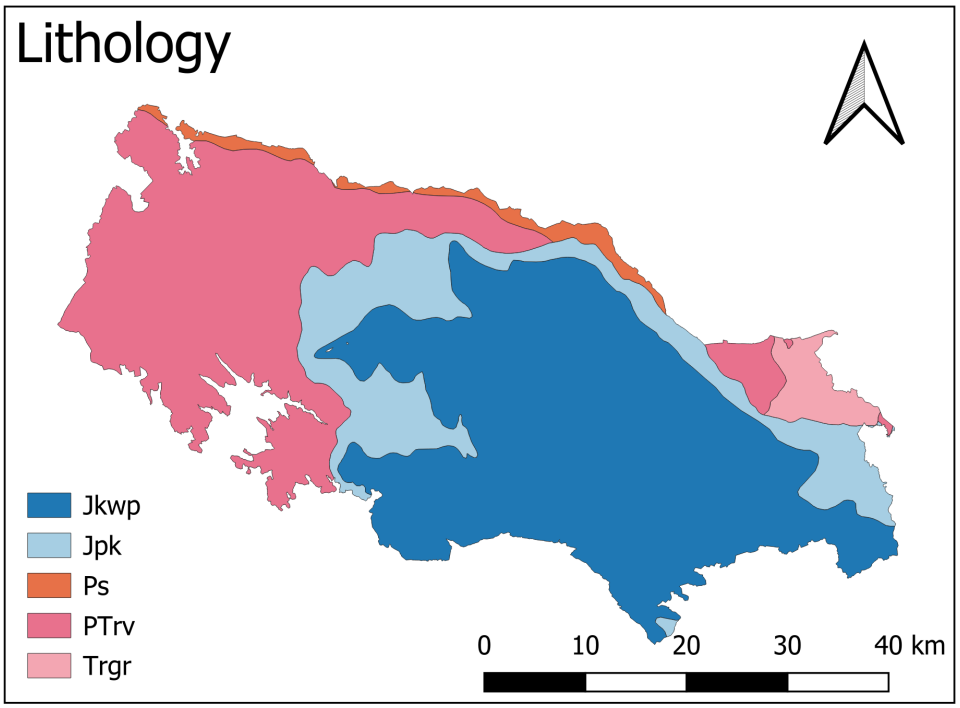

Figure B.4: Predisposing factor: Lithology.

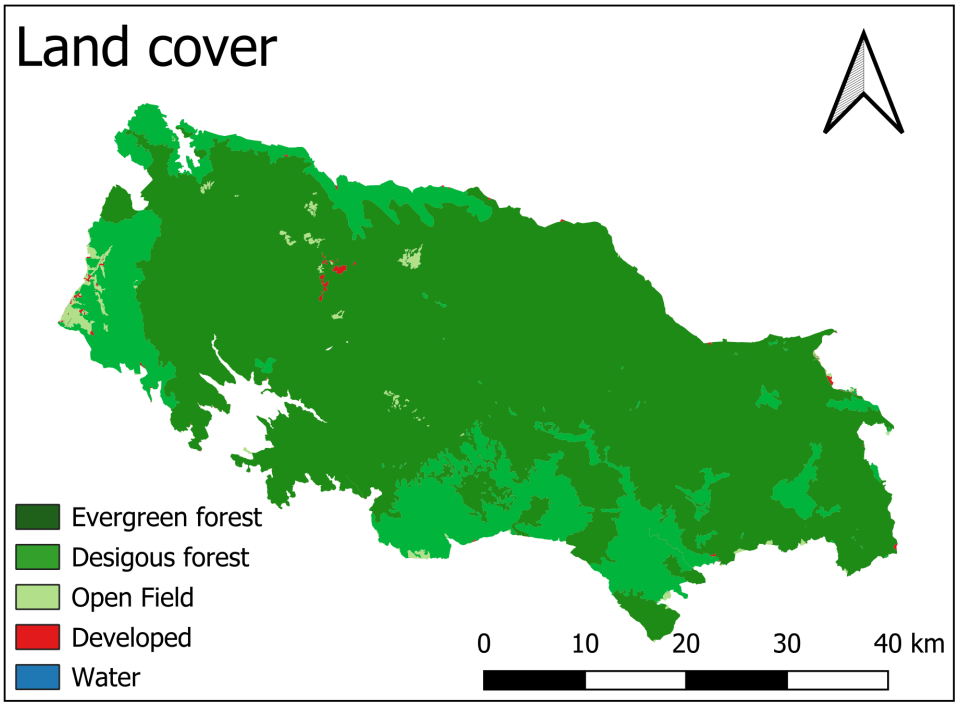

Figure B.5: Predisposing factor: Land cover.

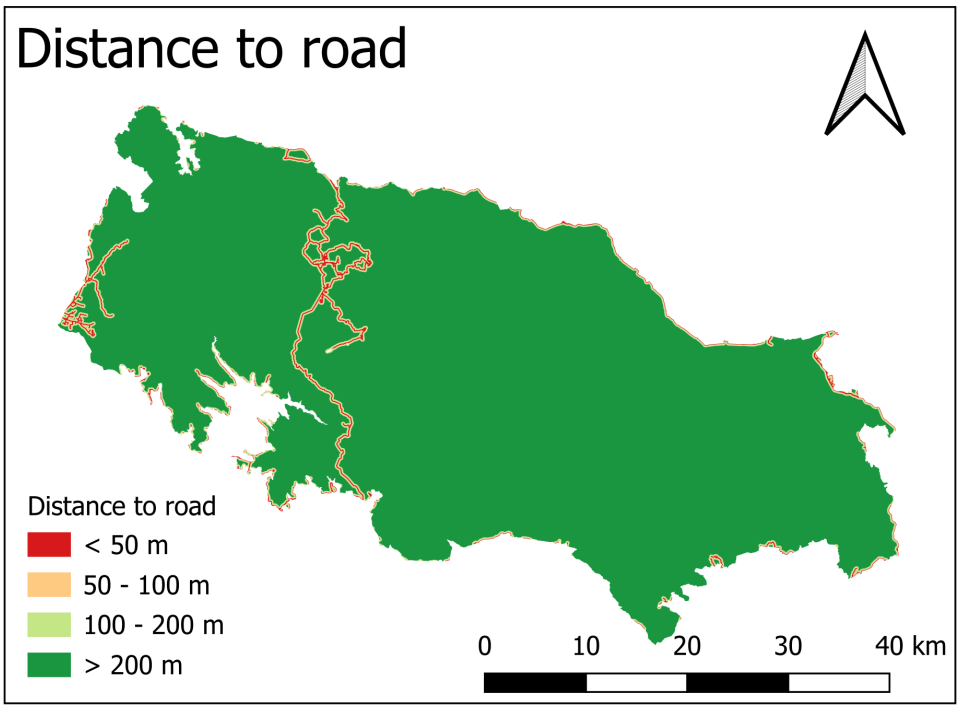

Figure B.6: Predisposing factor: Distance to road.

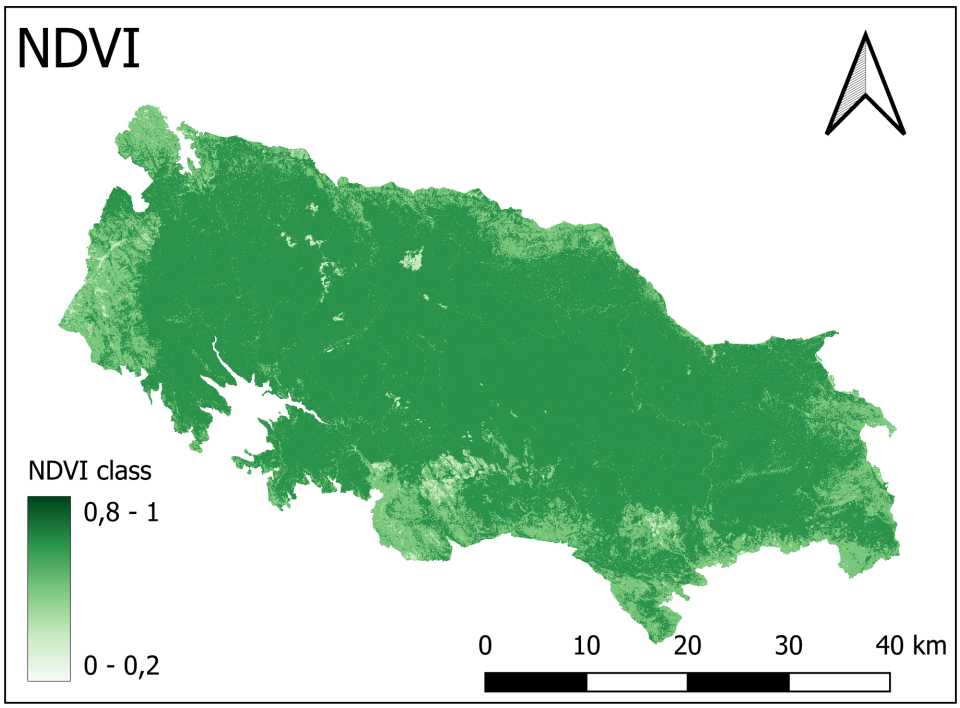

Figure B.7: Predisposing factor: NDVI.

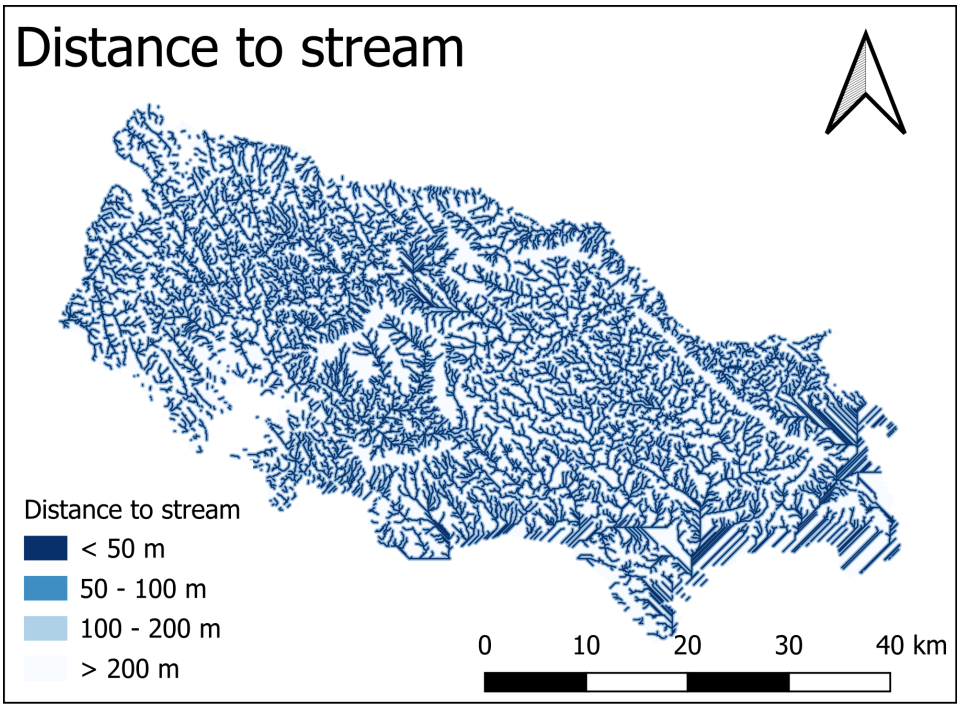

Figure B.8: Predisposing factor: Distance to stream.

B.2. FR values of all classes

Table B.1: Full results of frequency ratio analysis, also including insignificant classes

Factor	Class	Landslide area [km²]	Landslide ratio [%]	Class area [km²]	Class ratio [%]	FR
Slope (30 m DEM)	< 15°	0.0164	8.41	1614.1	73.06	0.115
	15° - 25°	0.0633	32.46	402.59	18.22	1.781
	25° - 35°	0.0580	29.74	159.64	7.23	4.116
	35° - 45°	0.0459	23.54	30.04	1.36	17.312
	> 45°	0.0114	5.85	3.00	0.14	43.005
Slope (12.5 m DEM)	< 15°	0.0216	11.09	1551.46	70.31	0.158
	15° - 25°	0.0566	29.06	436.83	19.8	1.468
	25° - 35°	0.0544	27.93	176.24	7.99	3.496
	35° - 45°	0.0465	23.87	37.37	1.69	14.094
	> 45°	0.0157	8.06	4.64	0.21	38.323
Aspect (30 m DEM)	Flat	0.0035	1.8	206.51	9.36	0.192
	N	0.0445	22.9	200.54	9.09	2.52
	NE	0.0298	15.34	260.12	11.79	1.301
	E	0.0212	10.91	239.52	10.85	1.005
	SE	0.0171	8.8	255.89	11.6	0.759
	S	0.0178	9.16	316.13	14.33	0.639
	SW	0.0217	11.17	331.61	15.03	0.743
	W	0.0152	7.82	225.05	10.2	0.767
	NW	0.0235	12.09	171.15	7.76	1.559
Aspect (12.5 m DEM)	Flat	0.0064	3.29	166.66	7.56	0.435
	N	0.0715	36.76	414.06	18.78	1.957
	E	0.0461	23.7	502.53	22.8	1.04
	S	0.036	18.51	635.48	28.83	0.642
	W	0.0345	17.74	485.79	22.04	0.805
Elevation	< 200 m	0.0275	14.18	333.57	15.2	0.933
	200 m - 400 m	0.0313	16.14	328.75	14.98	1.077
	400 m - 600 m	0.0723	37 .29	554.5	25.28	1.475
	600 m - 800 m	0.0436	22.49	631.12	28.77	0.782
	800 m - 1000 m	0.0158	8.15	289.62	13.2	0.617
	1000 m - 1200 m	0.0034	1.75	56.3	2.57	0.683
Landuse	Desigous forest	0.1144	58.82	416.34	18.87	3.117
	Developed	0.0001	0.05	5.16	0.23	0.22
	Evergreen forest	0.0754	38.77	1763.05	79.92	0.485
	OpenField	0.0046	2.37	21.6	0.98	2.415
Lithology	Sandstone	0.0593	30.49	1031.15	46.77	0.652
	Siltstone	0.0287	14.76	340.43	15.44	0.956
	Volcanic	0.105	53.98	726.48	32.95	1.638
	Limestone	0.0008	0.41	51.43	2.33	0.176
	Granite	0.0007	0.36	55.03	2.5	0.144
Distance to road	< 50 m	0.0106	5.45	24.23	1.1	4.958
	50 m - 100 m	0.0007	0.36	23.48	1.07	0.338
	100 m - 200 m	0.0031	1.59	46.42	2.11	0.757
	> 200 m	0.1801	92.6	2110.39	95.73	0.967
NDVI (median)	< 0.2	0.0004	0.21	0.64	0.03	7.067
	0.2 - 0.4	0.0418	21.46	30.32	1.37	15.622
	0.4 - 0.6	0.093	47.74	420.16	19.04	2.508
	0.6 - 0.8	0.0596	30.6	1756.05	79.56	0.385

Continued on next page

Table B.1 – continued from previous page

Factor	Class	Landslide area [km²]	Landslide ratio [%]	Class area [km²]	Class ratio [%]	FR
NDVI (maximum)	0.2 - 0.4	0.0052	2.67	4.98	0.23	11.808
	0.4 - 0.6	0.0405	20.77	43.64	1.98	10.5
	0.6 - 0.8	0.1405	72.05	2121.86	96.16	0.749
	> 0.8	0.0088	4.51	36.01	1.63	2.765
Distance to stream (30 m DEM)	< 50 m	0.0367	18.85	579.46	25.83	0.73
	50 m - 100 m	0.0253	12.99	386.63	17.24	0.754
	100 m - 200 m	0.0432	22.19	631.95	28.17	0.788
	> 200 m	0.0895	45.97	645.22	28.76	1.598
Distance to stream (12.5m DEM)	< 50 m	0.0544	27.93	645.22	25	1.117
	50 m - 100 m	0.0425	21.82	645.22	25	0.873
	100 m - 200 m	0.0661	33.93	645.22	25	1.357
	> 200 m	0.0317	16.27	645.22	25	0.651

C

Best combination of predisposing factors

Table C.1: Combination of different predisposing factors: (1) Slope, (2) Aspect, (3) Landuse, (4) Lithology, (5) Distance to road

Version	Combined classes	AUC validation	AUC validation std
V5	(1) + (2) + (3) + (4) + (5)	0.90	0.010
V6	(1) + (2) + (3) + (4)	0.90	0.009
V7	(1) + (2) + (3) + (5)	0.90	0.010
V8	(1) + (2) + (4) + (5)	0.85	0.018
V9	(1) + (3) + (4) + (5)	0.90	0.008
V10	(2) + (3) + (4) + (5)	0.78	0.010
V11	(1) + (2) + (3)	0.90	0.009
V12	(1) + (2) + (4)	0.85	0.017
V13	(1) + (2) + (5)	0.85	0.016
V14	(1) + (3) + (4)	0.90	0.007
V15	(1) + (3) + (5)	0.91	0.007
V16	(1) + (4) + (5)	0.87	0.013
V17	(2) + (3) + (4)	0.78	0.010
V18	(2) + (3) + (5)	0.76	0.009
V19	(2) + (4) + (5)	0.67	0.024
V20	(3) + (4) + (5)	0.76	0.008
V21	(1) + (3)	0.90	0.006

Table C.2: Portion of areas classified as very low, low, moderate, high and very high in susceptibility map V7

Susceptibility	Area [km²]	Area Ratio [%]	Landslide Pixel (10 m x 10 m)	Landslide Ratio [%]	Landslide Density [Pixel / km²]	FR
Very Low	1069.49	48.53	30	1.54	0.03	0.03
Low	775.13	35.18	354	18.23	0.46	0.52
Moderate	301.30	13.67	775	39.91	2.57	2.92
High	49.02	2.22	488	25.13	9.96	11.32
Very high	8.68	0.39	295	15.19	33.99	38.95

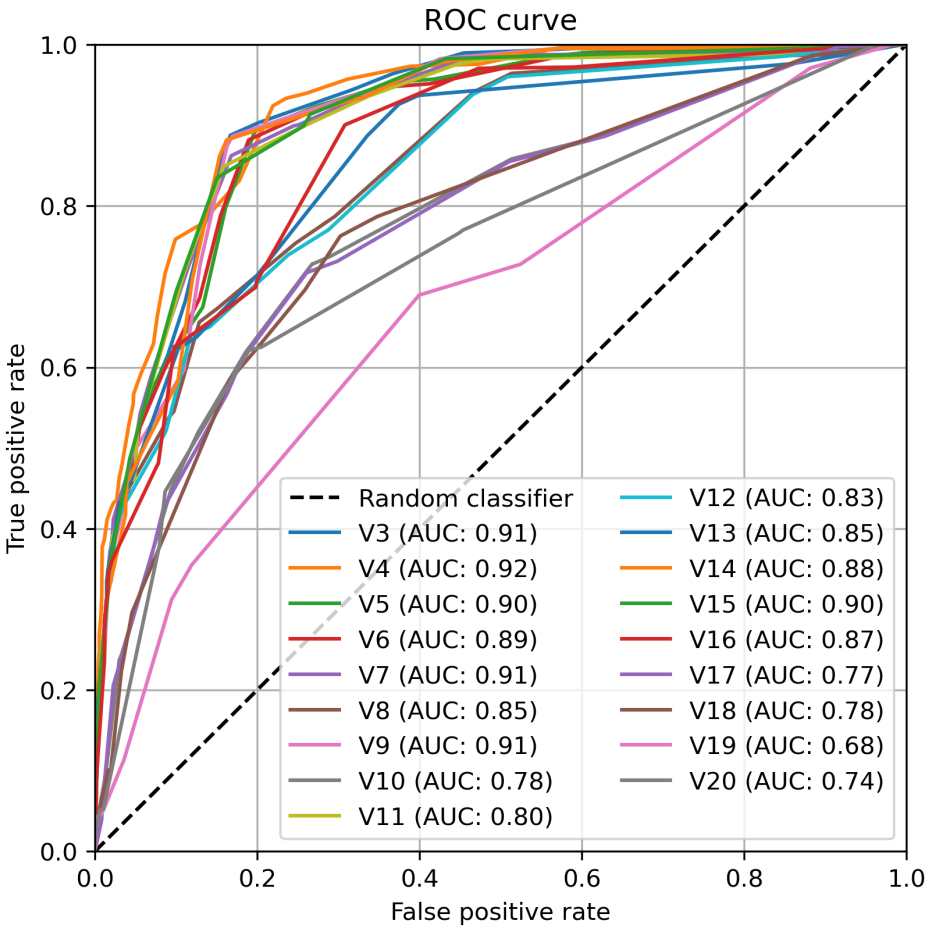

Figure C.1: ROC curve of susceptibility maps from different combinations of predisposing factors. All landslide points were used as training samples in this pre analysis.

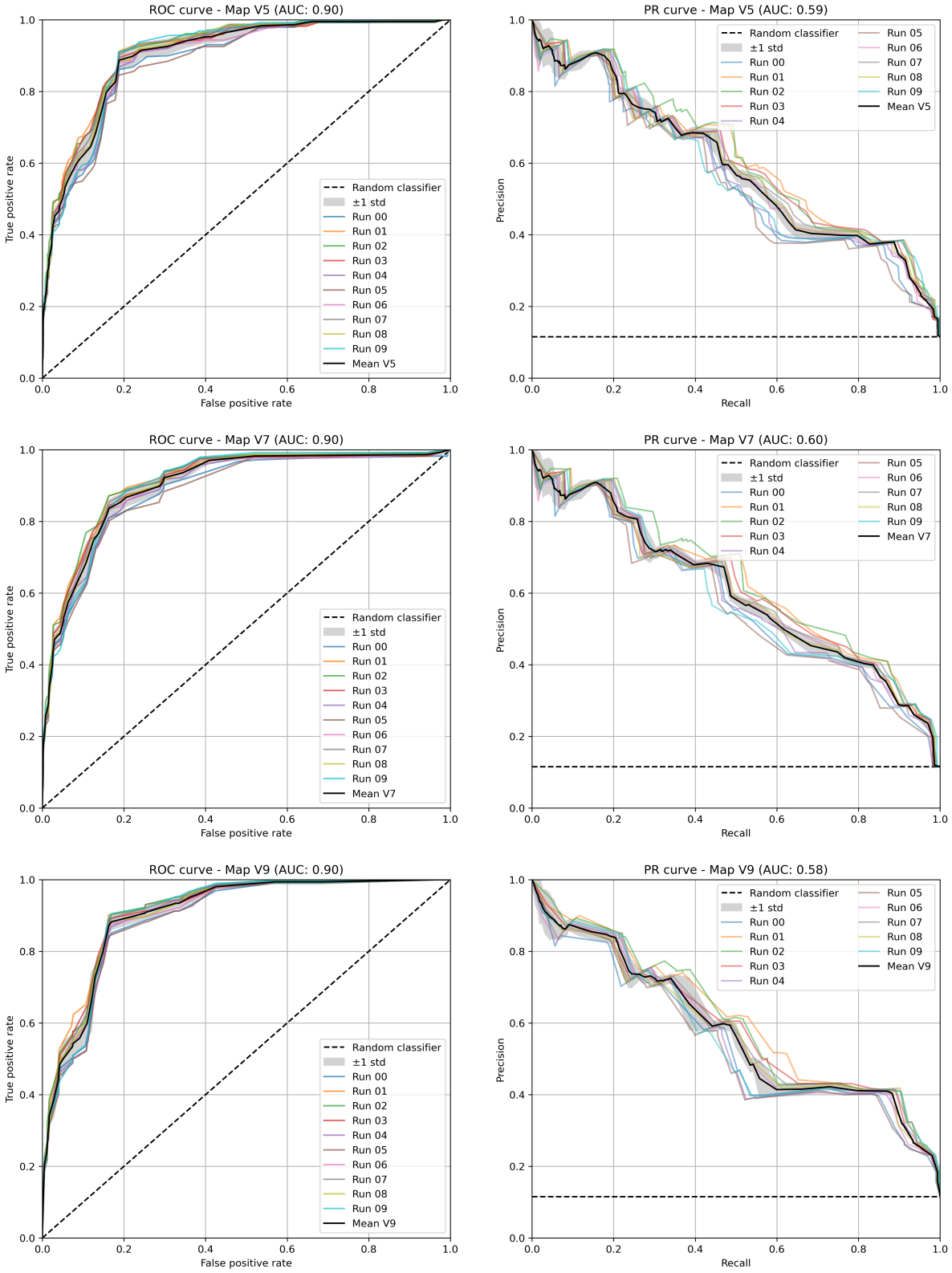

Figure C.2: ROC and PR curves from validation period of all versions with mean AUC of 0.90 from all 10 calibration/validation runs (Part 1).

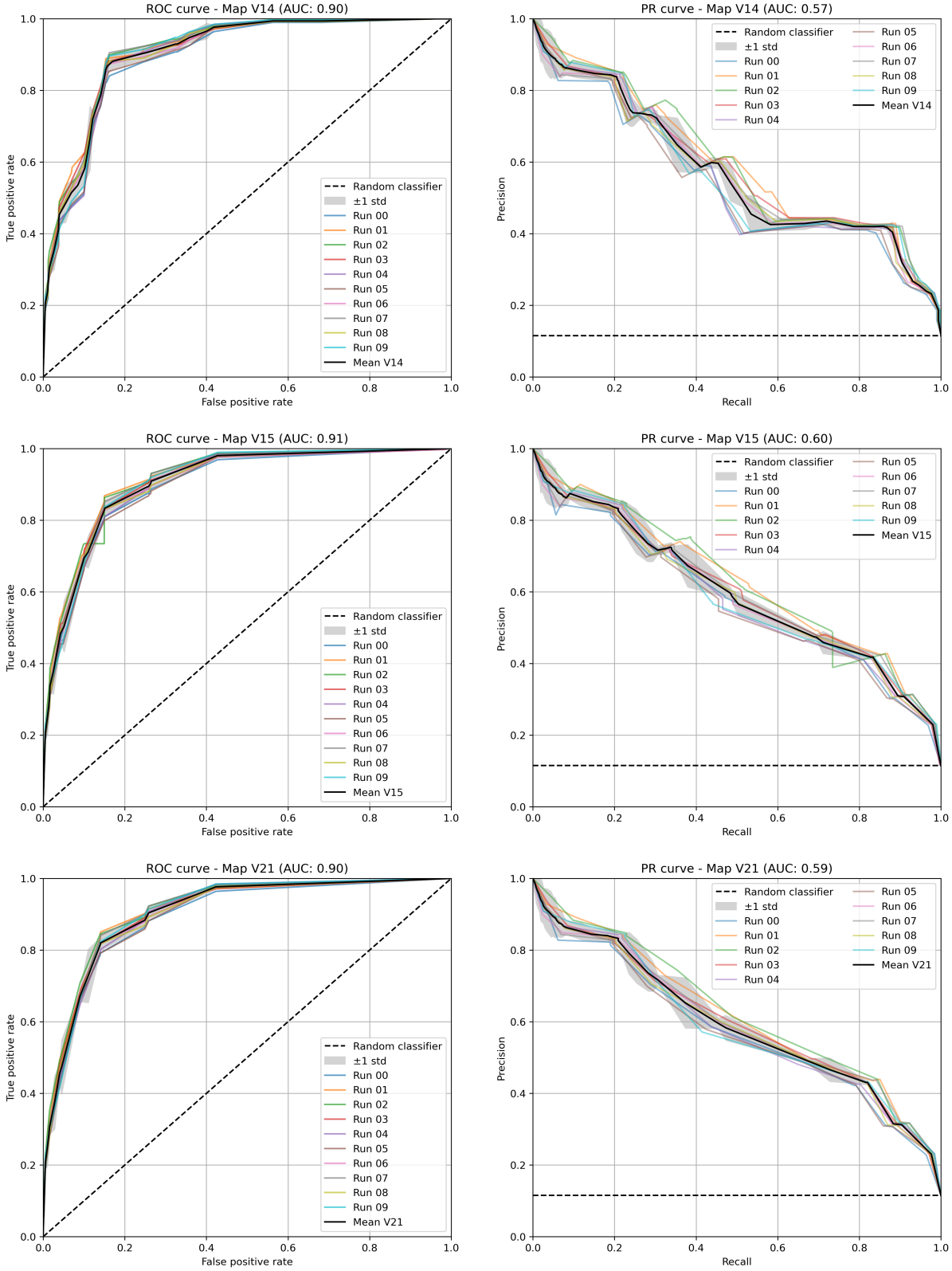

Figure C.3: ROC and PR curves from validation period of all map versions with mean AUC of 0.90 from all 10 calibration/validation runs (Part 2).

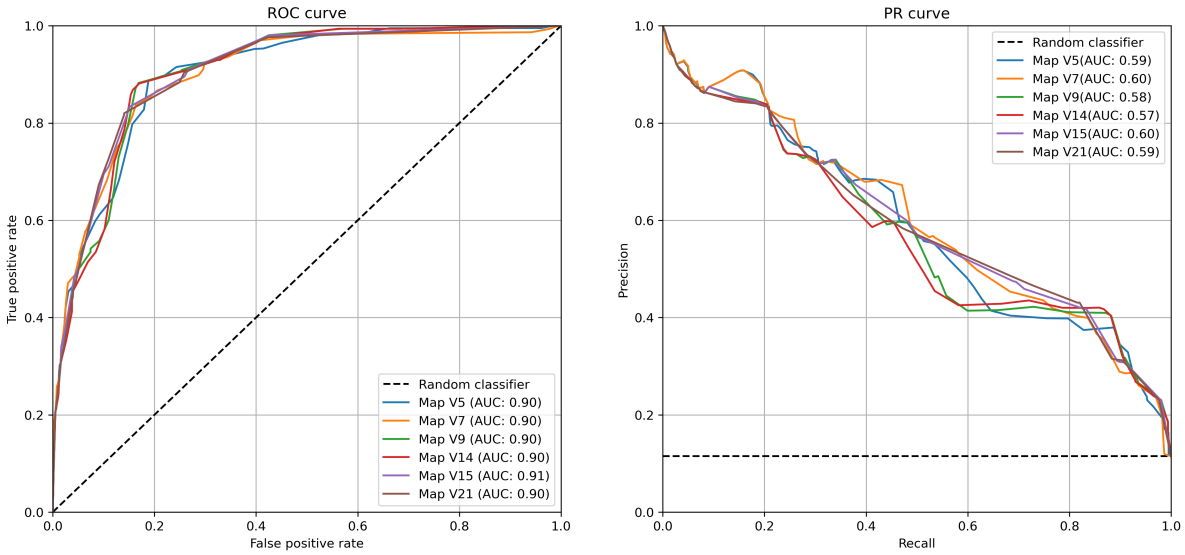

Figure C.4: Mean ROC and PR curve of all 10 calibration/validation runs of map versions with AUC > 0.90.

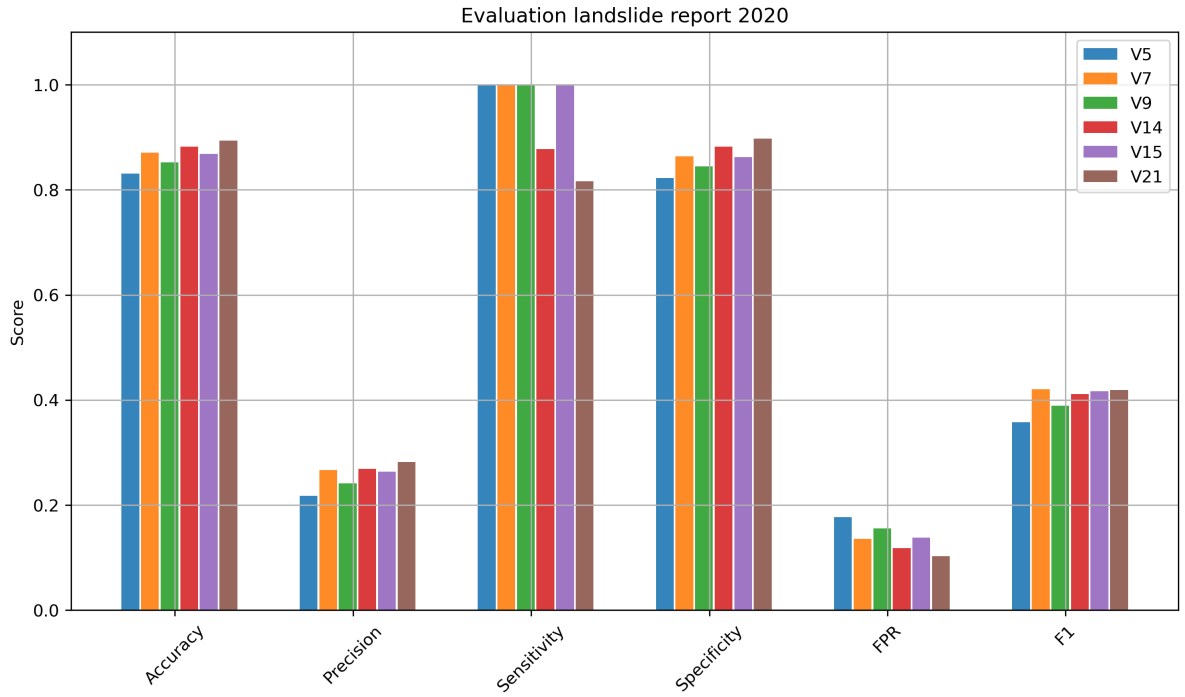

Figure C.5: Additional performance metrics calculated from known locations of the landslide report 2020 to determine which map version can predict this single landslide even best. The combination used for Map V7 thereby shows the best overall performance.

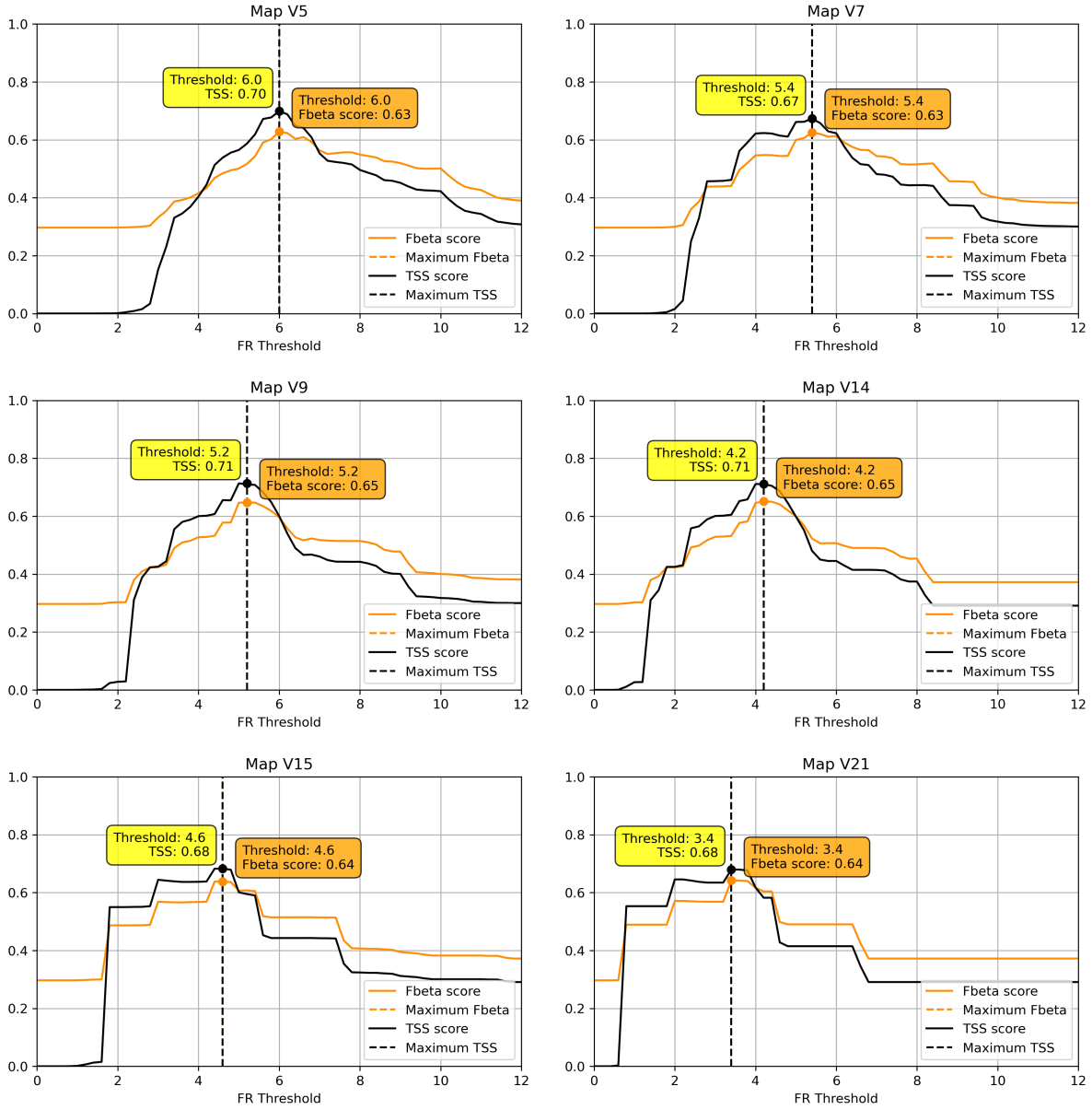

Figure C.6: Determination of FR threshold between low and moderate susceptibility for all map versions with AUC larger than 0.90. The threshold is determined by the maximum F_{betha} and TSS score calculated from the validation samples.

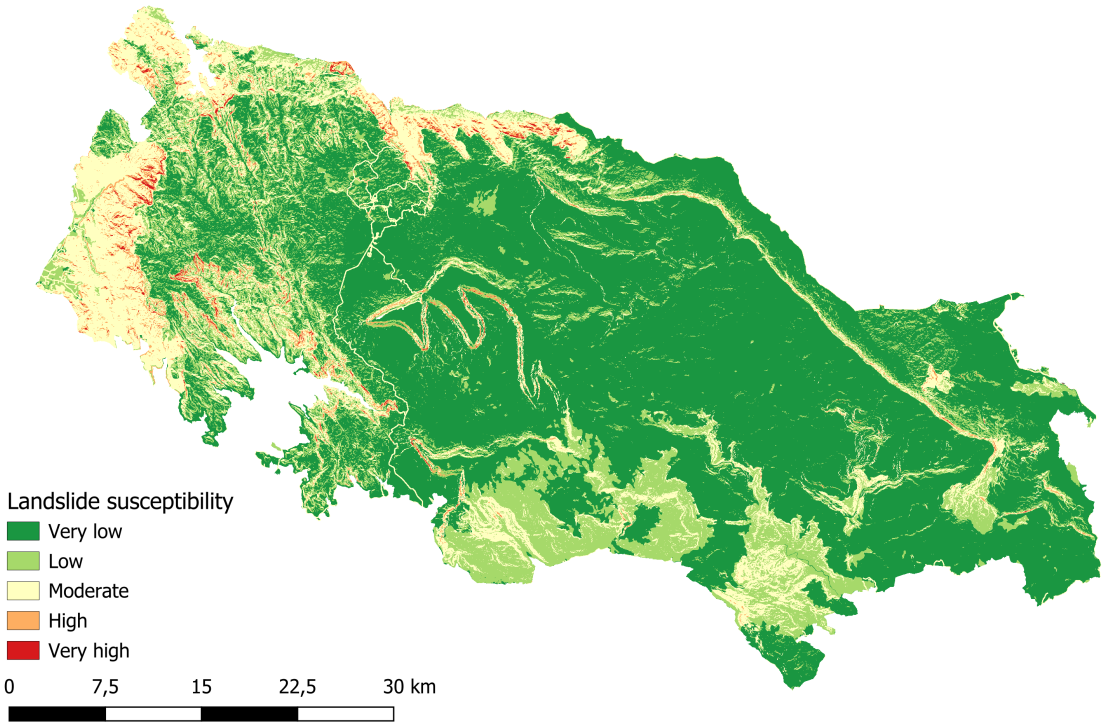

Figure C.7: Map V5: Susceptibility map derived from predisposing factors Slope, Aspect, Land cover, Lithology, and Distance to road.

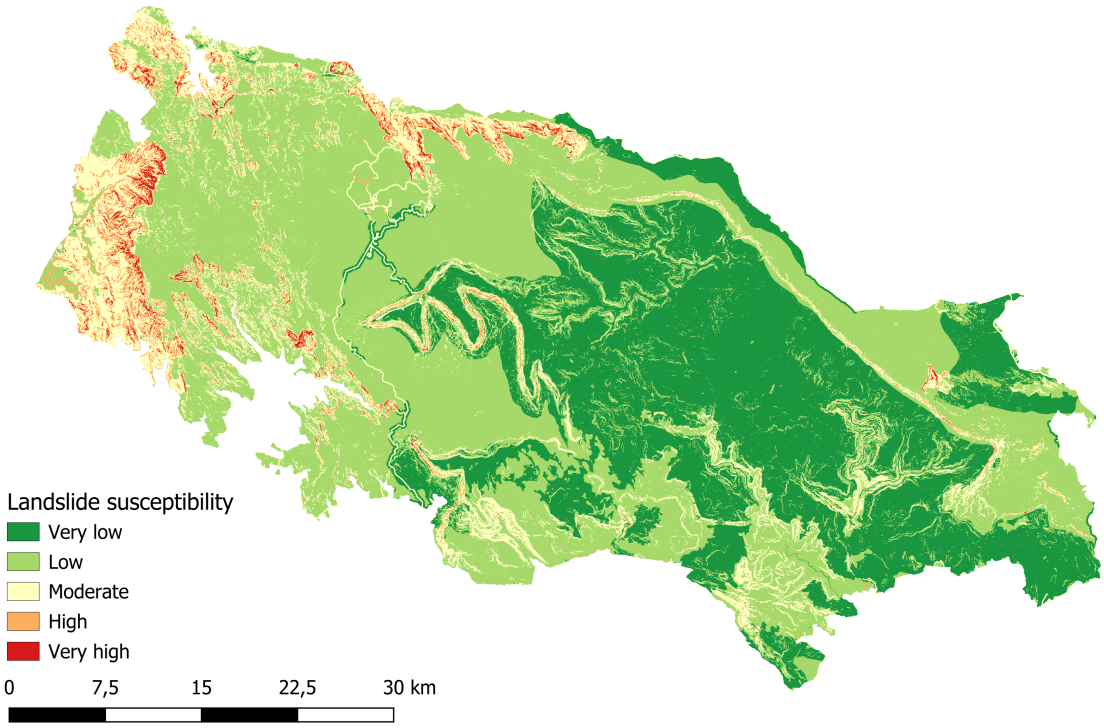

Figure C.8: Map V9: Susceptibility map derived from predisposing factors Slope, Land cover, Lithology, and Distance to road.

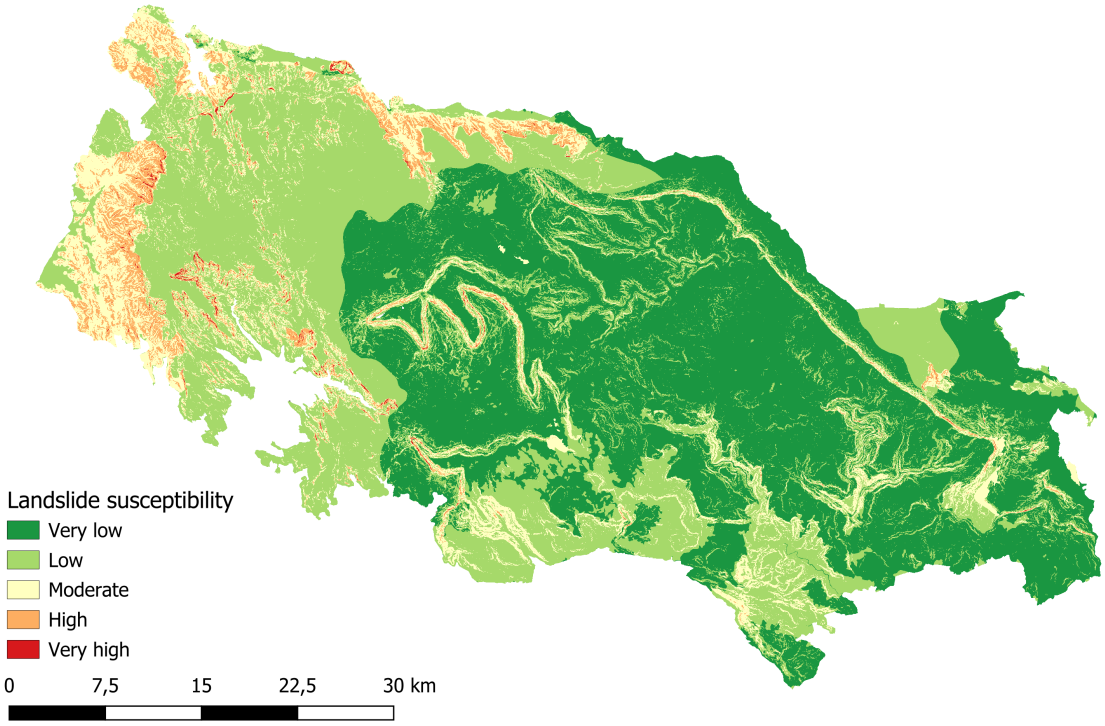

Figure C.9: Map V14: Susceptibility map derived from predisposing factors Slope, Land cover, and Lithology.

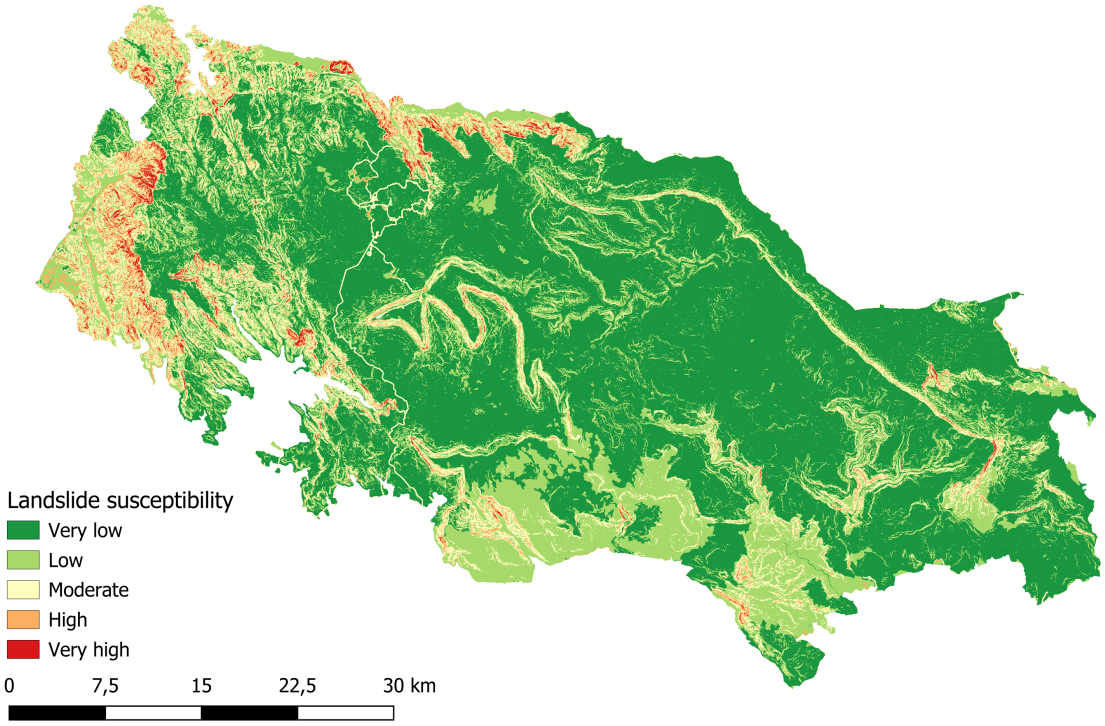

Figure C.10: Map V15: Susceptibility map derived from predisposing factors Slope, Land cover, and Distance to road.

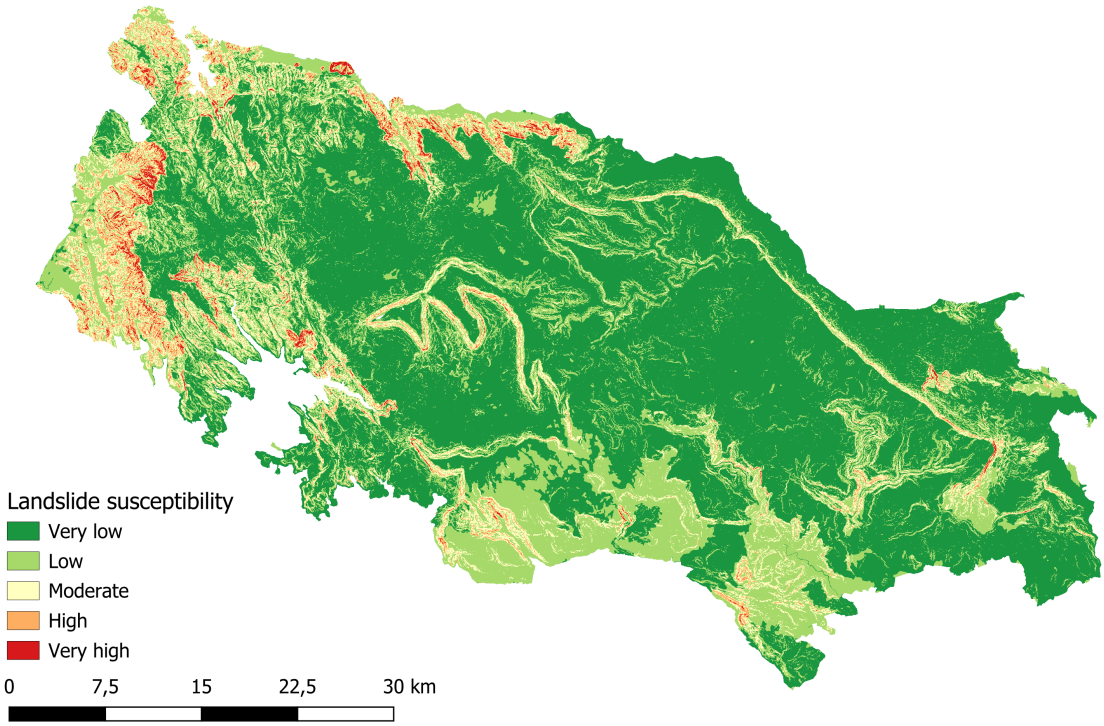

Figure C.11: Map V21: Susceptibility map derived from predisposing factors Slope and Land cover.

D

Additional Fieldwork Pictures and Results

D.1. Field site pictures

(a) (b)

Figure D.1: Waterfalls (a) and waterslides (b) add additional complexity to the stream in catchment Ny6.

Figure D.2: One of many small reservoirs within study catchment Ny6.

(a) **(b)**

Figure D.3: Densely vegetated slopes (a) and stream (b) in catchment Ny6.

(a) (b)

Figure D.4: Large boulders in the streams of catchment Ny6 (a) but also in locations further away from the stream (b).

Figure D.5: Large landslide in catchment M43A with different stabilization attempts.

D.2. Additional results

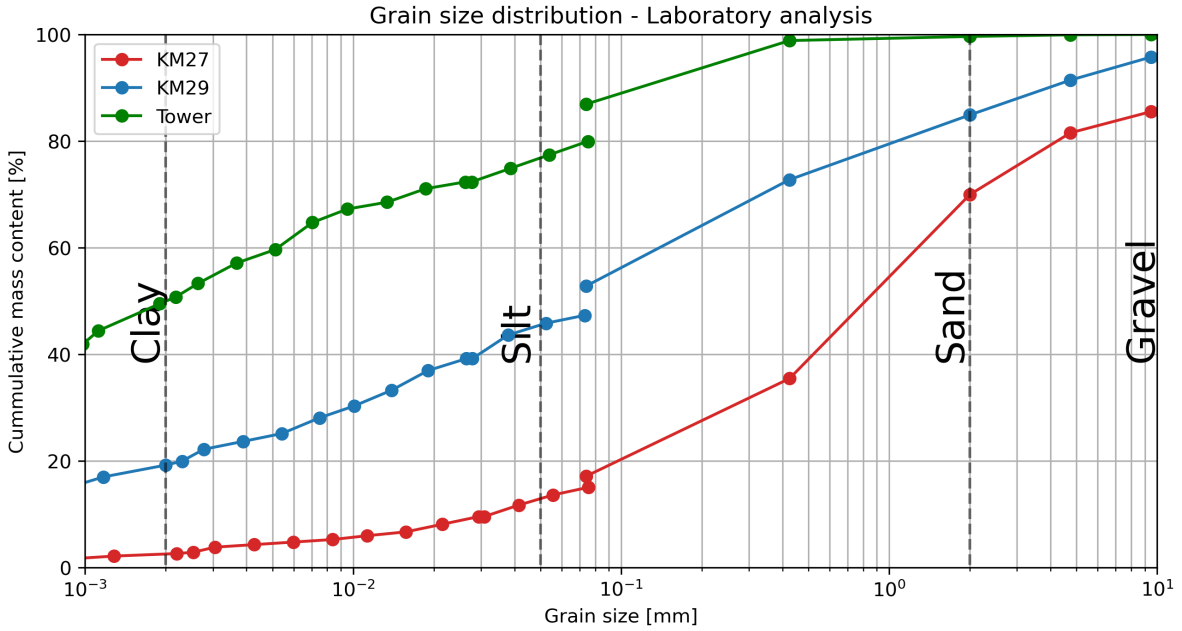

Figure D.6: Grain size distribution determined in the laboratory to verify the field method.

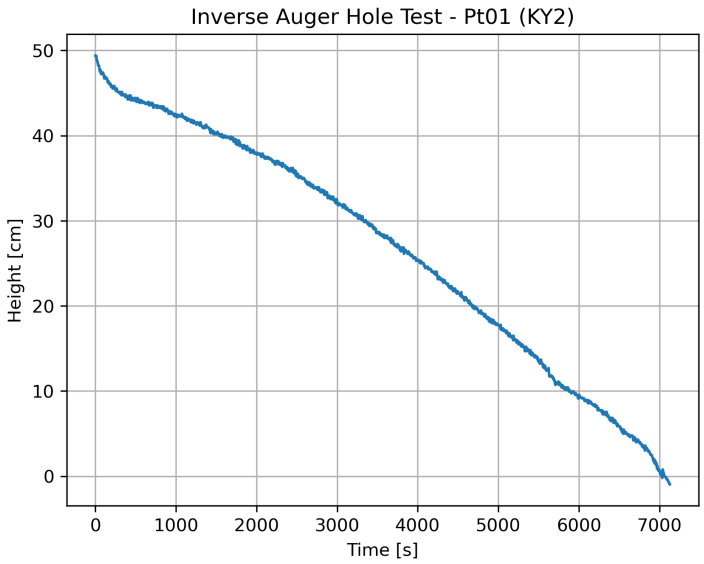

Figure D.7: Measured drawdown in auger hole at KY2. No repetition was performed due to the slow drawdown.

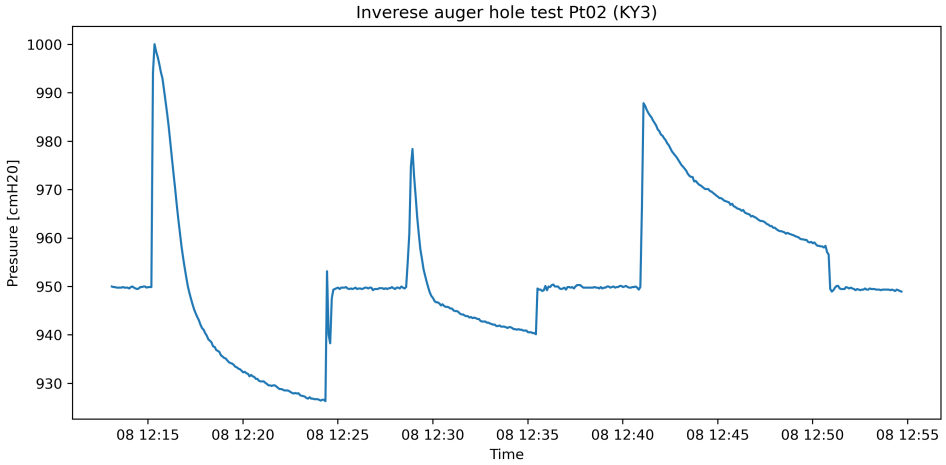

Figure D.8: Measured drawdown in auger hole at KY3. The test was repeated three times resulting in decreasing infiltration with each repetition.

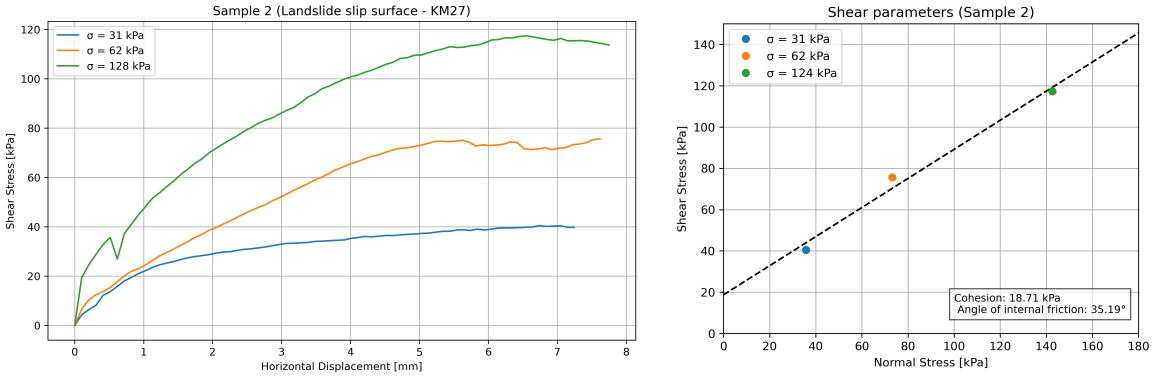

Figure D.9: Direct shear test: Sample set 2.

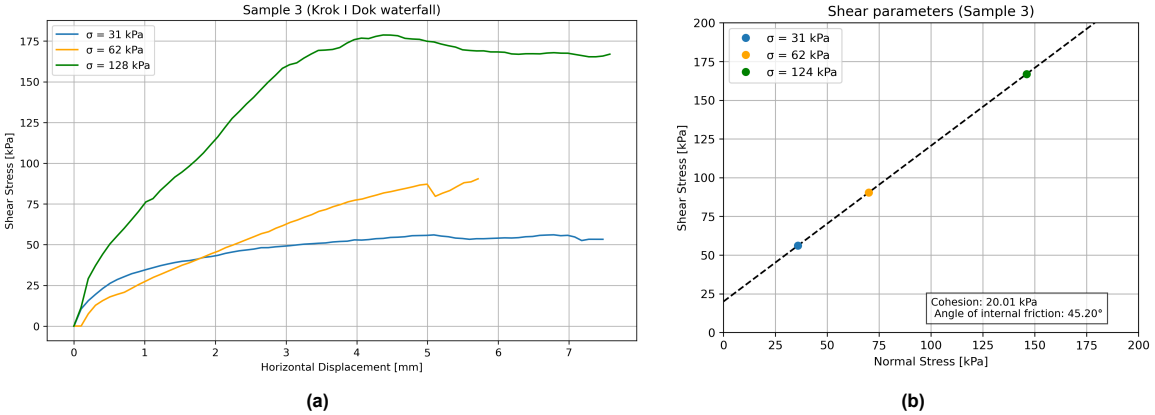

Figure D.10: Direct shear test: Sample set 3.

E

Hydrological observations

E.1. Precipitation

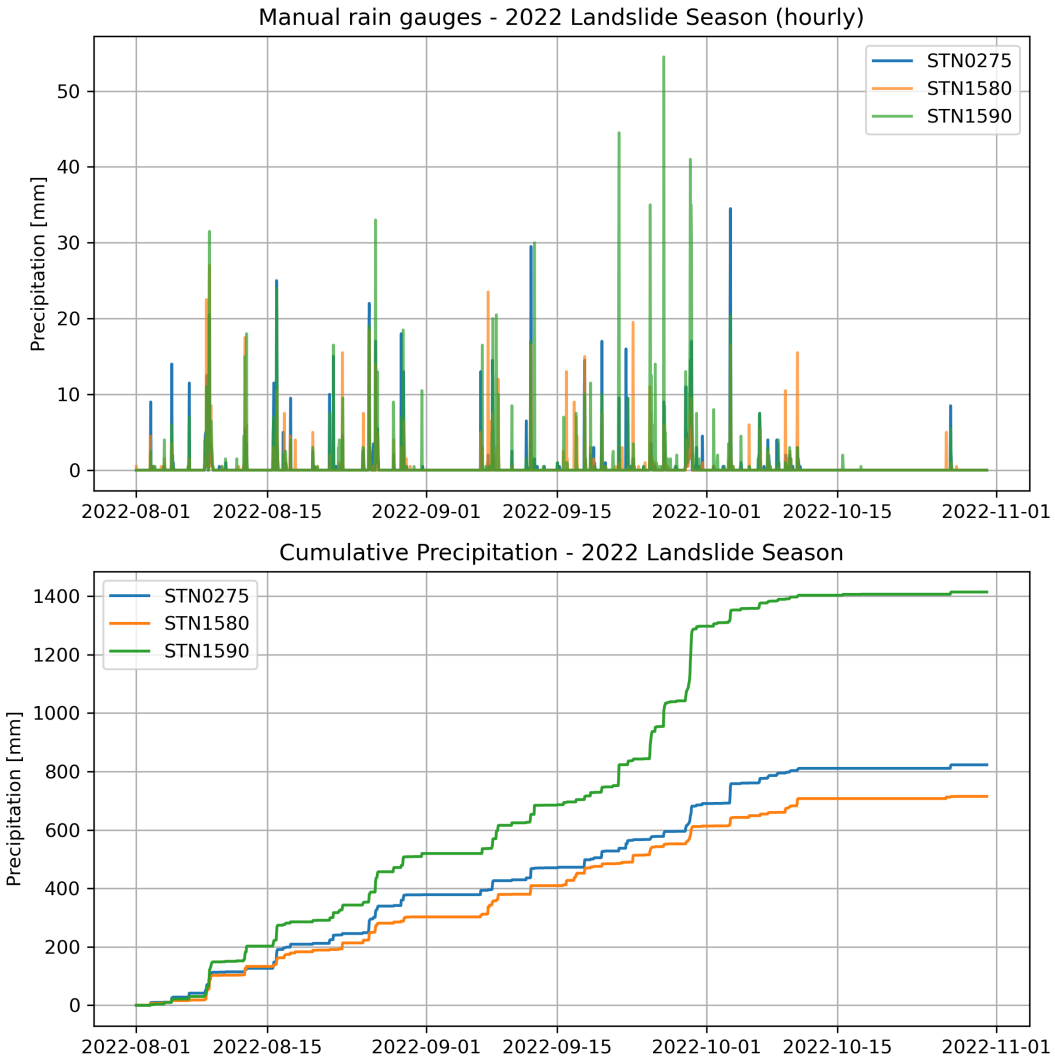

Figure E.1: Precipitation observed at manual rain gauges around catchment Ny6. During the landslide event in September 2022, a cumulative precipitation of up to 300 mm in one day could be observed.

E.2. Discharge

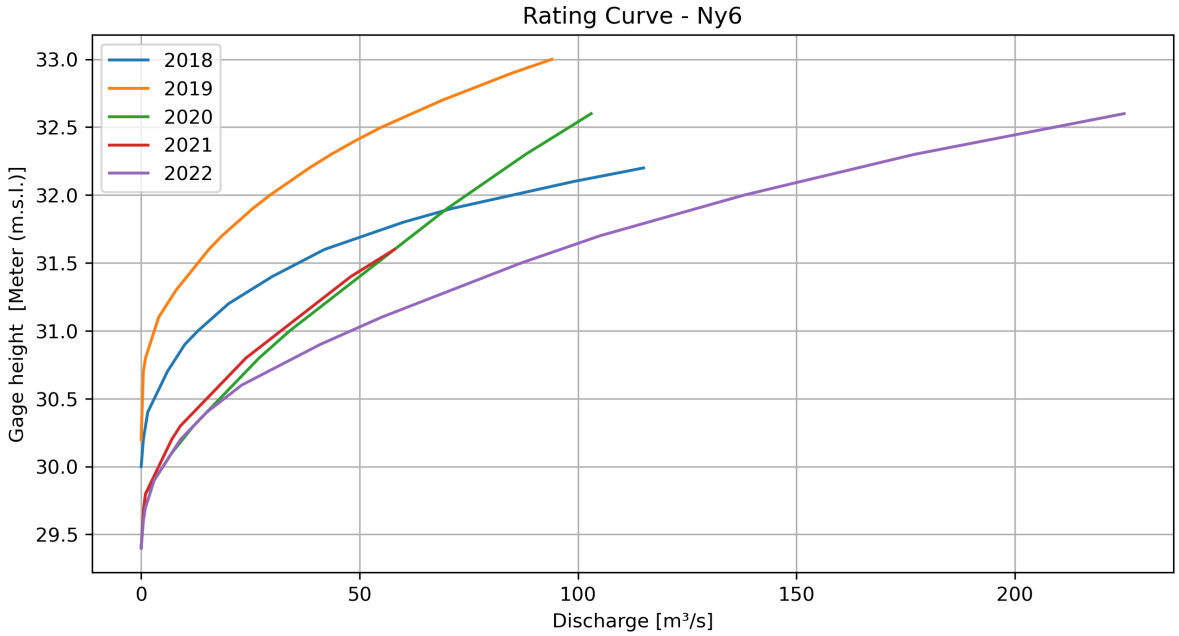

Figure E.2: Rating curves 2018 - 2022 at gauge Ny6 (Royal Irrigation Department, 2024).

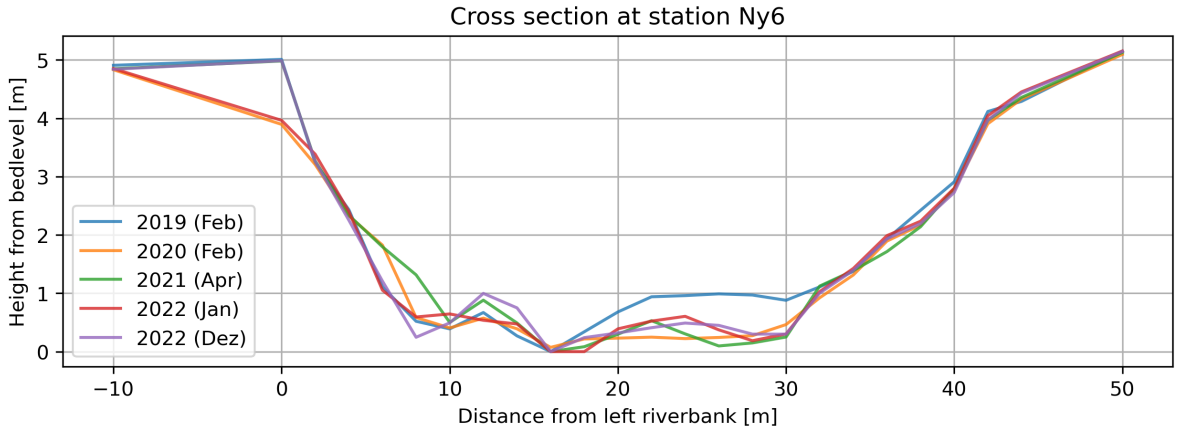

Figure E.3: Channel cross-section at station Ny6. Changes could only be observed at the bottom of the channel. The river banks remain stable (Royal Irrigation Department, 2024).

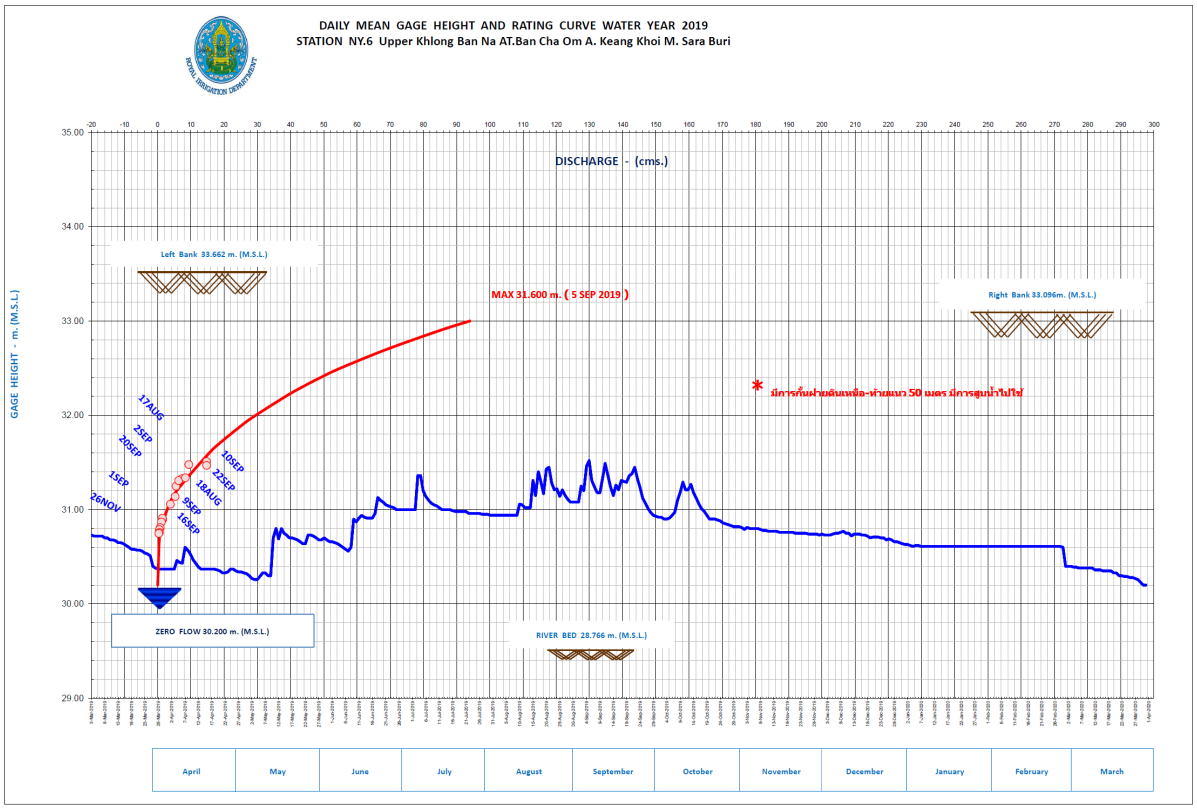

Figure E.4: Measured water level and rating curve 2019 at gauge Ny6 (Royal Irrigation Department, 2024).

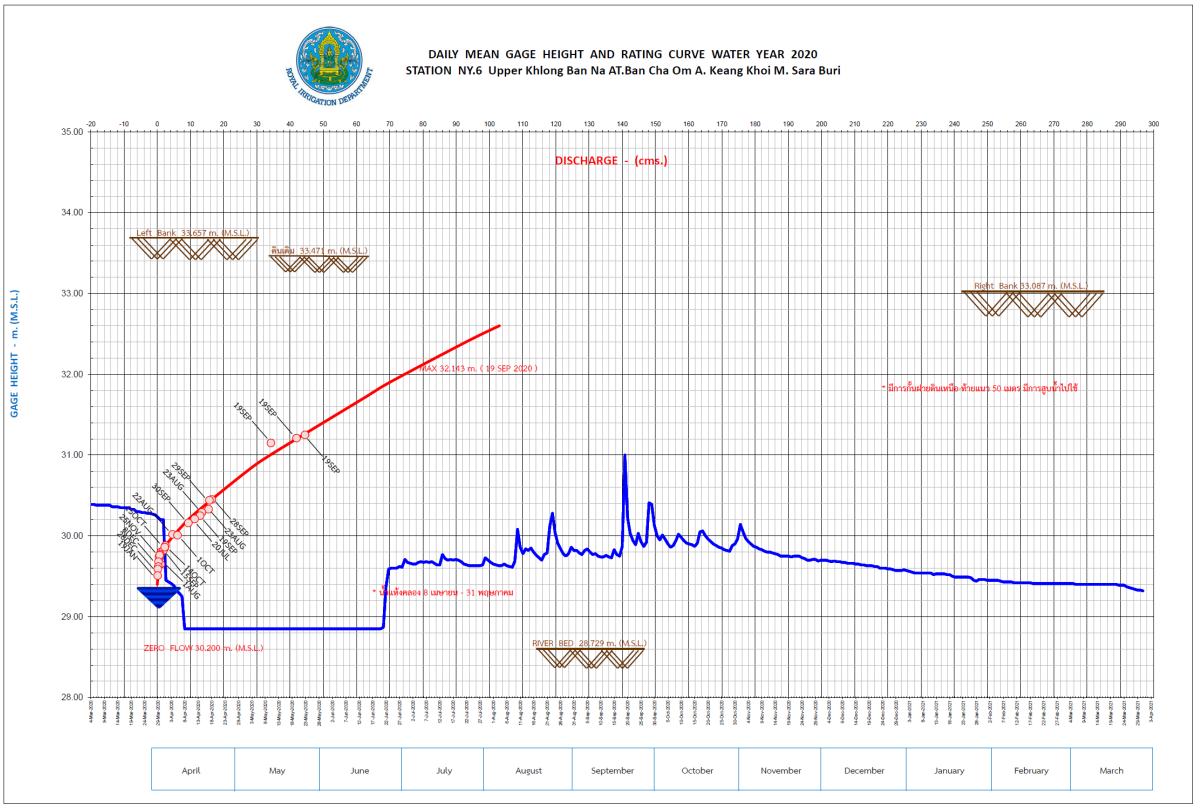

Figure E.5: Measured water level and rating curve 2020 at gauge Ny6 (Royal Irrigation Department, 2024).

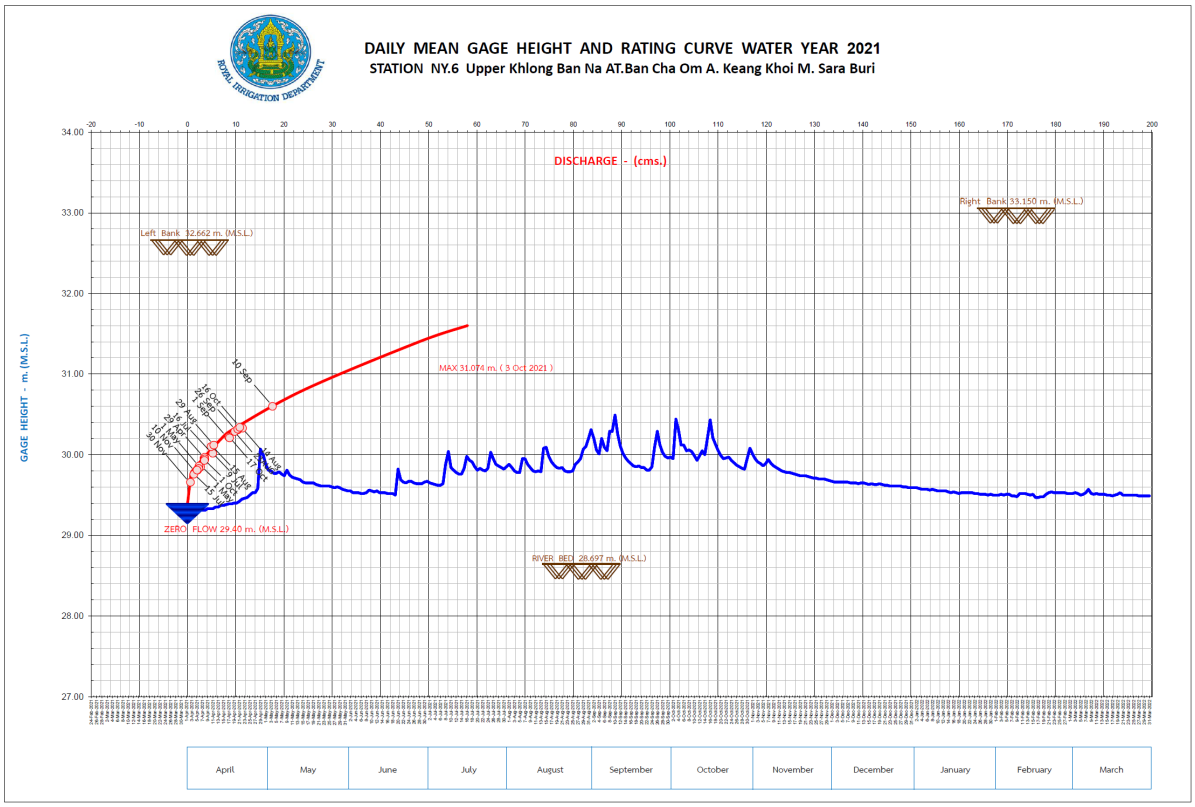

Figure E.6: Measured water level and rating curve 2021 at gauge Ny6 (Royal Irrigation Department, 2024).

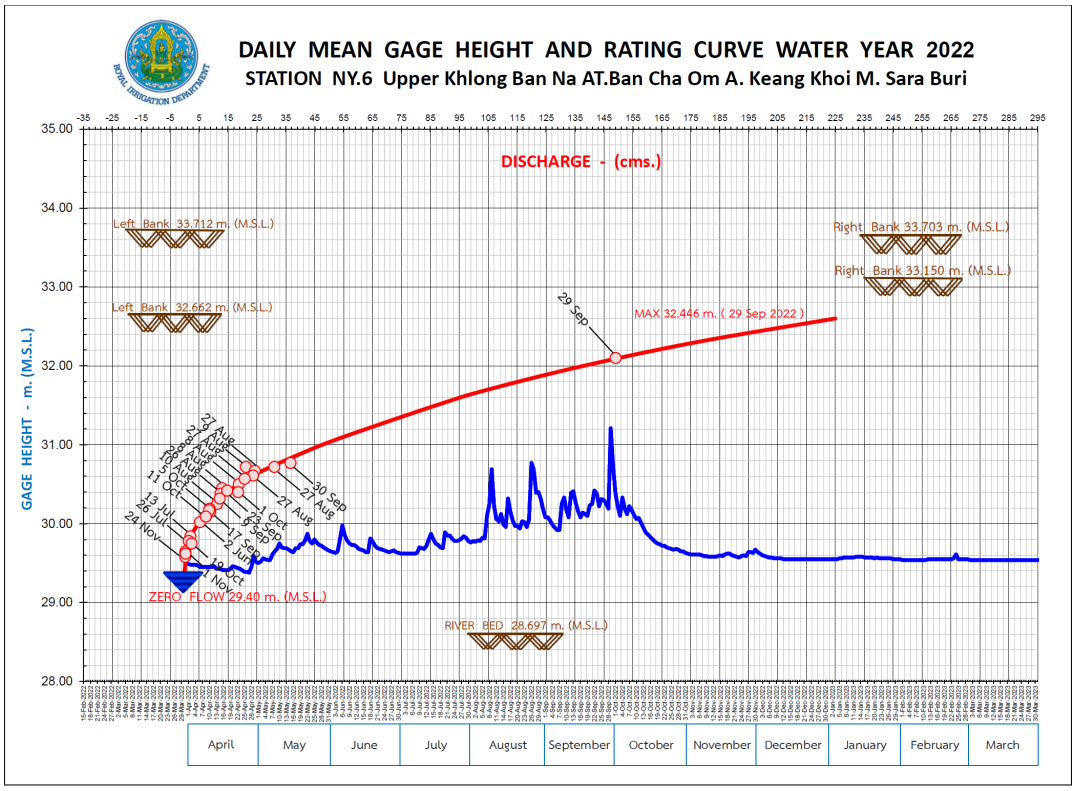

Figure E.7: Measured water level and rating curve 2022 at gauge Ny6 (Royal Irrigation Department, 2024).

F

LISEM debugging: Version 0.2.4

Within the LISEM model, there are two options to run the model. The first option is a user interface in which the model settings and required input maps can be selected via checkboxes. The other option is to build a custom model by using the functions of the LISEM model in a scripting environment. While the scripting environment allows for more flexibility in the model setup, the GUI version has the benefit that it is easier to use for inexperienced users once the *run*-file is prepared. Therefore, the first approach was to test the GUI version of the LISEM model to show that it can be used for the assessment of predisposing landslide conditions and modeling of landslide events. Unfortunately, however, multiple bugs could be found when testing the LISEM model version 0.2.4:

1. The water balance of the model has a large error of > 10 % and in some cases even up to 50 % of the rainfall forcing
2. The model is inconsistent with how water heights in the soil are handled. The Green and Ampt infiltration function handles water heights, namely the groundwater and wetting front height, as total water height while others handle them as piezometric heights (This explains part of the water balance error.)
3. The model has no clearly defined boundary conditions. Water is allowed to flow in and out at the boundary of the model. (This also explains part of the water balance error.)
4. The rainfall input file is interpreted as absolute rainfall input per time step and not as rainfall intensity. The rainfall input file therefore has to be adjusted to the chosen time step.
5. The generated output file contains errors. For example, when activating the channel option, every third column of the output file gets overwritten with a constant value.
6. The function for evapotranspiration does not work and causes the system to run out of storage.
7. The advanced Green and Ampt function does not work and causes the system to run out of storage. Furthermore, multiple bugs could be found in the function.
8. The transient flow function can not handle flat terrain and requires a minimum slope of 0.25° in each pixel.
9. The slope stability model has an error in the definition of the infinite slope function.

While most of these errors are easy to fix, it was decided to rewrite the functions in the scripting environment to bypass the time-consuming procedure of compiling the software after each edit. Furthermore, multiple model behaviors could be observed which made the standard model unsuitable for continuous modeling and required a custom model in the scripting environment. These behaviors based on design decisions in the model development are especially:

- The overland and groundwater flow models only allow D4 flow (No diagonal flow). This leads to large amounts of water getting trapped in sinks when working with a DEM with coarse resolution in catchments with steep and complex topography. This problem can not be solved by filling the sinks, as these algorithms allow D8 flow (also diagonal flow). This especially becomes a problem when modeling slope stability because fully saturated cells, due to the ponding effect, will always fail in steep terrain.

- The process of preferential shallow subsurface flow is not included in the model. Infiltrated water either stays in the cell or percolates into the groundwater in which transport in a neighboring cell is possible. While this might not be a problem during a multihazard event simulation it's a crucial process for continuous modeling. Without this process, the model can not be calibrated on an observed hydrograph.
- Percolation through the bedrock into deeper groundwater layers is not included in the model. With long simulation times of more than one month, this eventually leads to a fully saturated catchment.
- The soil moisture is not updated when water is moved out of a cell by groundwater flow and the groundwater zone is replaced with the soil moisture zone. Therefore, every time step a very small amount of water is created. This effect increases with increasing saturation of the soil. The created amounts of water are small and lead to a water balance error of about -0.002 mm/hr and can therefore be neglected in event-based modeling. However, when performing longer simulations of more than a week the effect is important on the scale of a single cell. By filling the emptied groundwater height with the soil moisture layer without updating the soil moisture the potential of moving water out of the soil column gets limited, especially with increasing saturation. Therefore, this effect long term leads to a fully saturated soil, even though the effect does not seem significant when only considering the water balance error.

F.1. Synthetic catchment

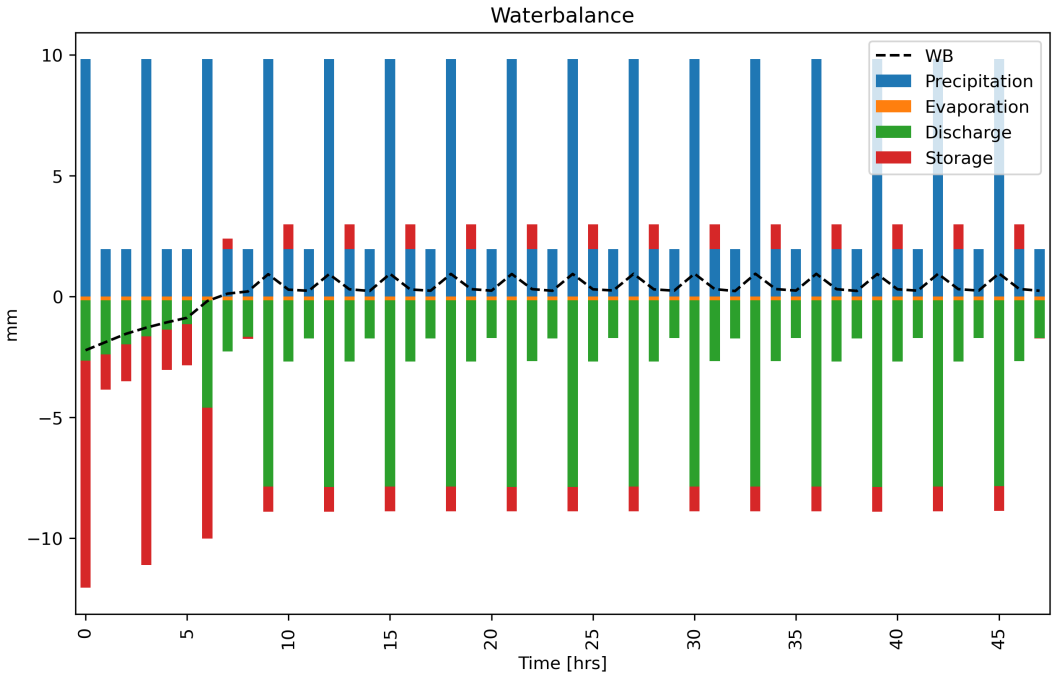

Figure F.1: Water balance with open boundary conditions. Maximum water balance error after spin-up phase: 0.01 mm.

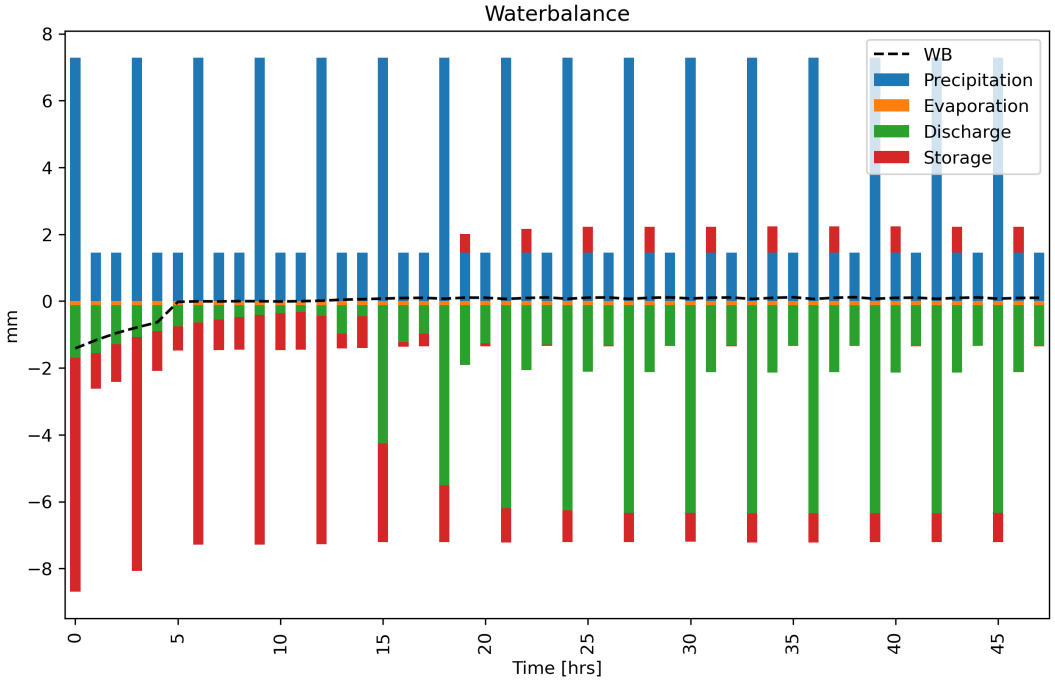

Figure F.2: Water balance with closed boundary conditions. Maximum water balance error after spin-up phase: 1.2 mm.

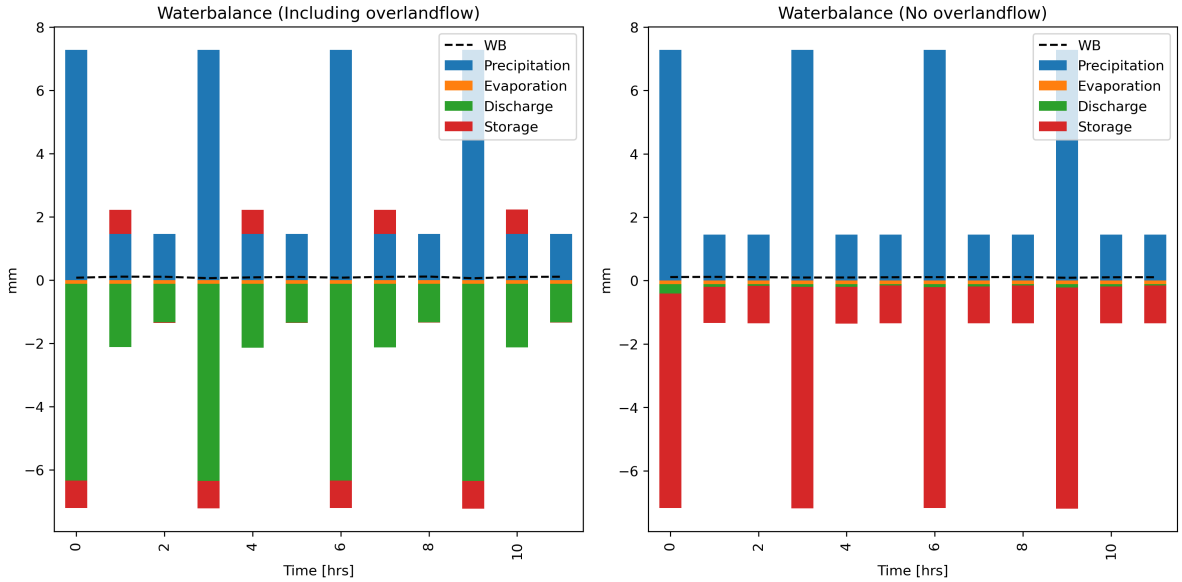

Figure F.3: Water balance with activated (left) and deactivated (right) overland flow.

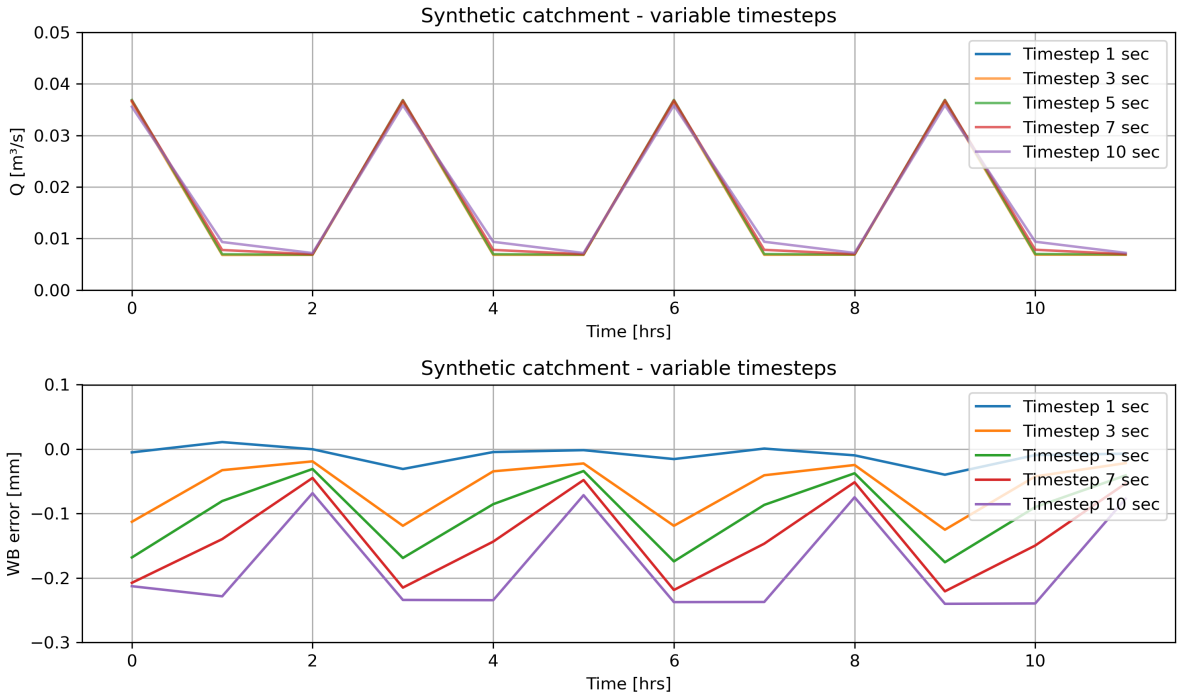

Figure F.4: Sensitivity analysis to determine minimum time step required for stable flow conditions with a cell size of 5 m.

F.2. Model calibration

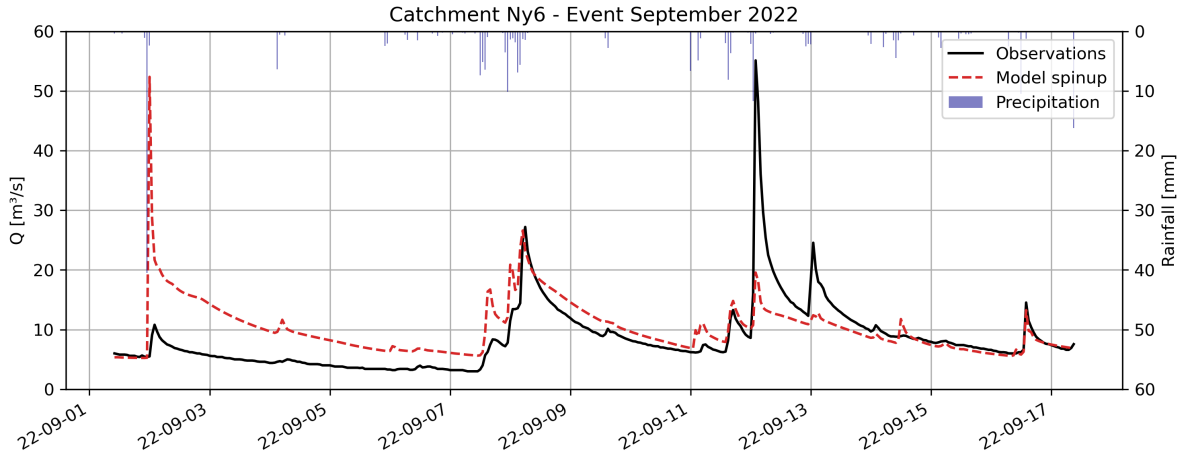

Figure F.5: Predicted streamflow during the spin-up phase of the calibrated model.

G

Missing event on radar observations

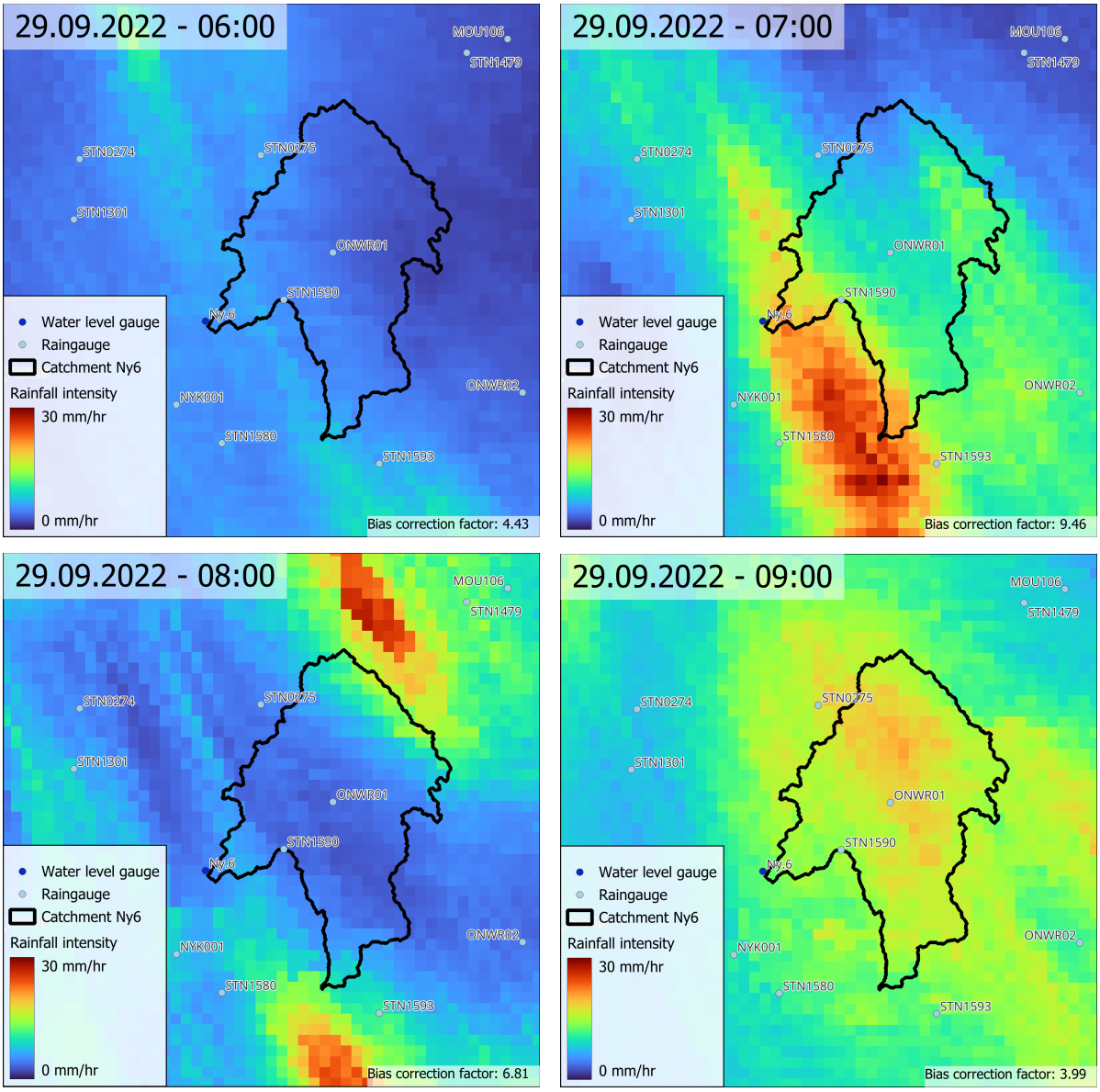

Figure G.1: Radar observations of spatial rainfall patterns during the storm event on September 29th

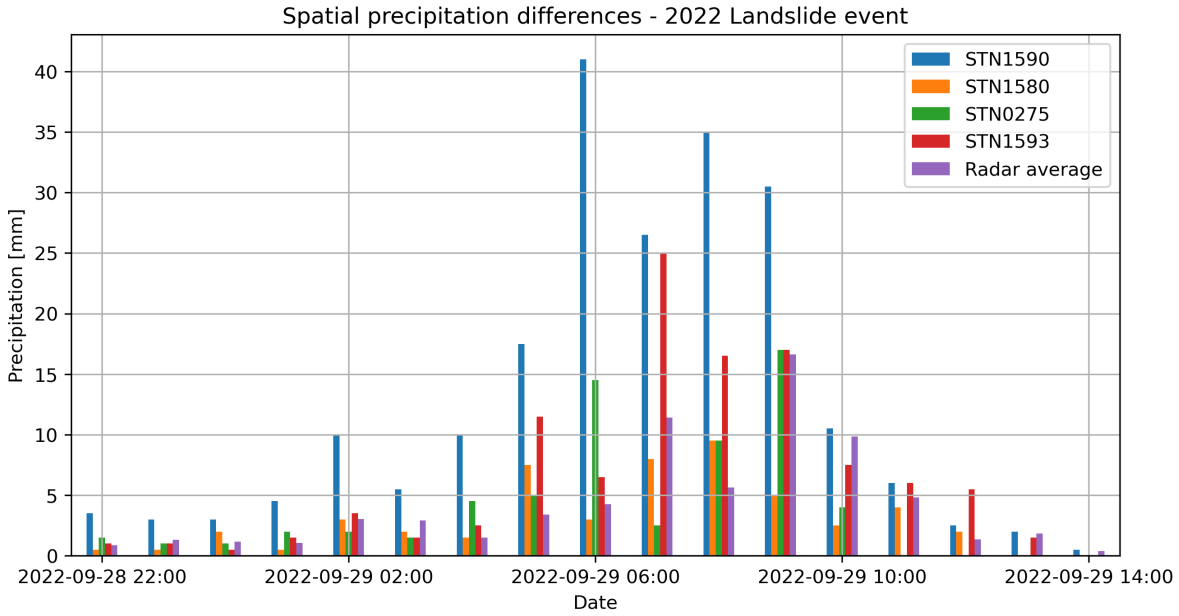

Figure G.2: Rain gauge observations of precipitation around catchment Ny6 during the storm event on September 29th

H

Sensitivity analysis: Infinite slope model

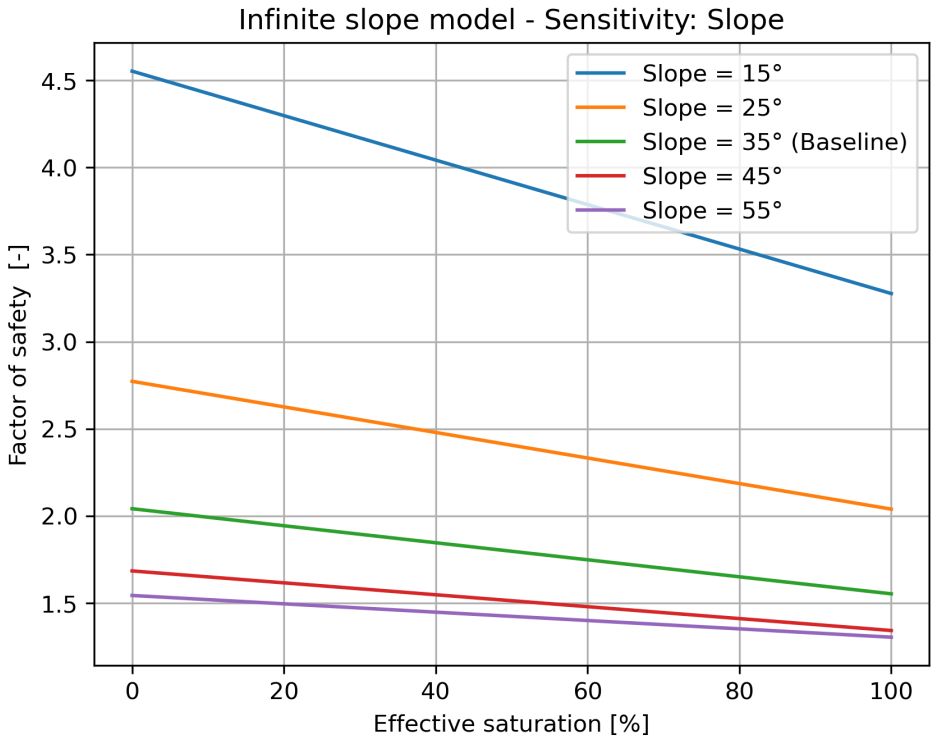

Figure H.1: Sensitivity Analysis: Slope. Increasing slope angle results in decreasing slope stability.

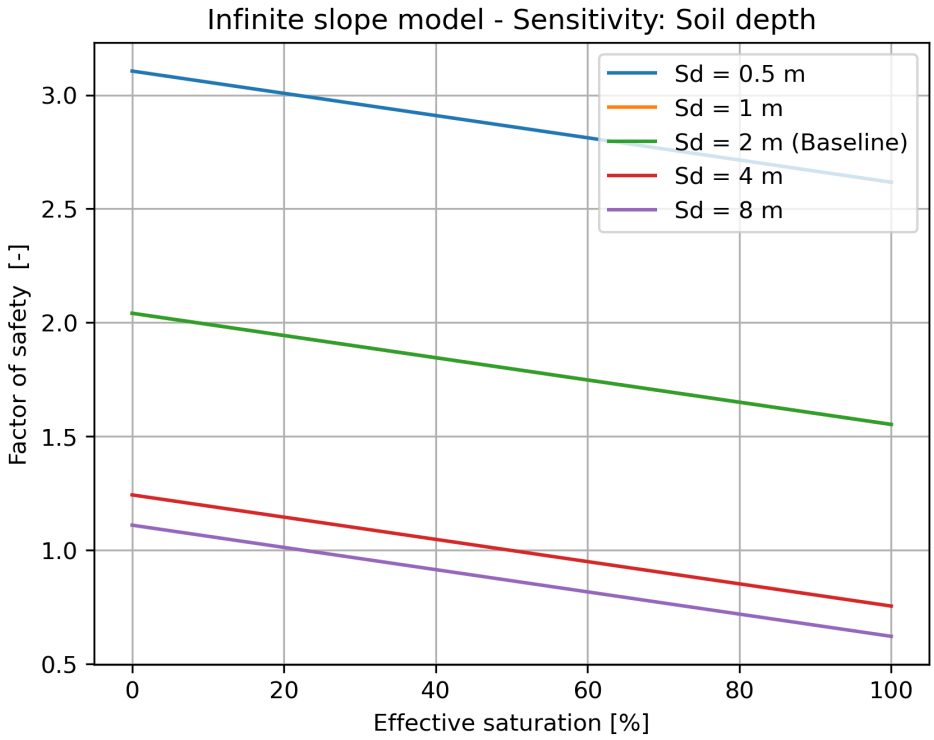

Figure H.2: Sensitivity Analysis: Soil Depth. Increasing soil depth results in decreasing slope stability.

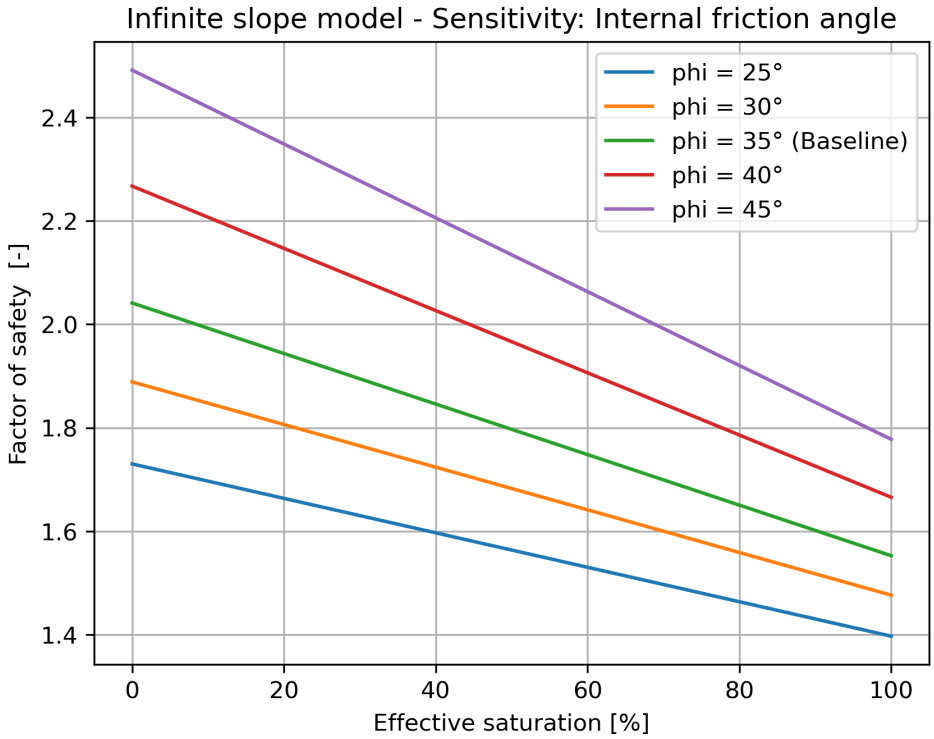

Figure H.3: Sensitivity Analysis: Internal friction angle. Increasing angle of internal friction results in increasing slope stability.

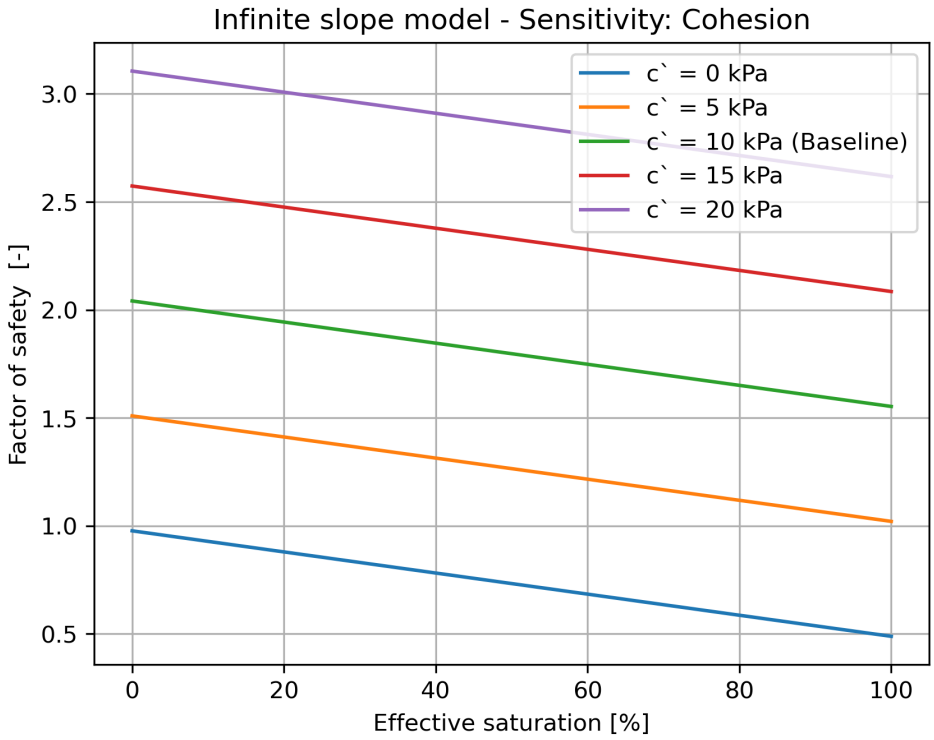

Figure H.4: Sensitivity Analysis: Cohesion. Increasing cohesion results in increasing slope stability.

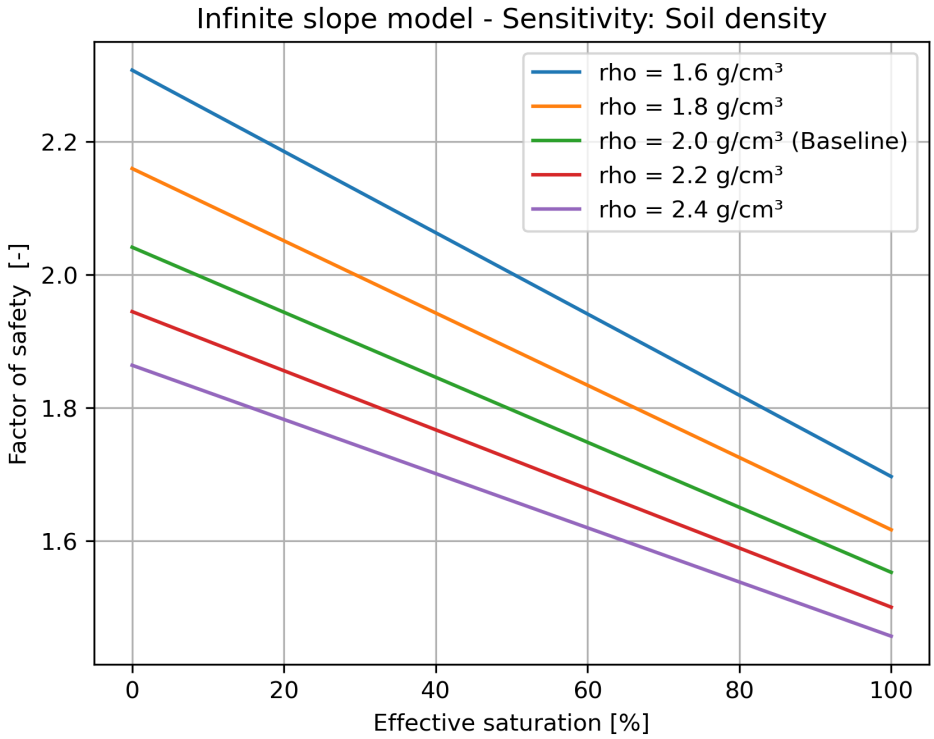

Figure H.5: Sensitivity Analysis: Soil Density. Increasing soil density results in decreasing slope stability.